

BORIS ZHIVKOV DESHEV

On the coevolution of galaxies and
their host clusters



BORIS ZHIVKOV DESHEV

On the coevolution of galaxies and
their host clusters



UNIVERSITY OF TARTU
Press

The study was carried out at Tartu Observatory, University of Tartu, Estonia.

The dissertation was admitted on April 2, 2019, in partial fulfillment of the requirements for the degree of Doctor of Philosophy in physics, and allowed for defense by the Council of the Institute of Physics, University of Tartu.

Supervisors: Prof. Dr. Alexis Finoguenov,
University of Helsinki, Finland

Prof. Dr. Peeter Tenjes,
University of Tartu, Estonia

Prof. Dr. Bodo Ziegler,
Vienna University, Austria

Opponents: Dr. Sean L. McGee,
School of Physics and Astronomy, University of Birmingham,
Birmingham, United Kingdom

Defense: May 23, 2019, University of Tartu, Estonia

ISSN 1406-0302

ISBN 978-9949-03-009-5 (print)

ISBN 978-9949-03-010-1 (pdf)

Copyright: Boris Zhivkov Deshev, 2019

University of Tartu Press

www.tyk.ee

Contents

List of original publications	6
1 Introduction	11
2 Data	21
2.1 Multi-fibre spectroscopy of galaxies in A520	21
2.2 21 cm imaging of galaxies in A963 and A2192	39
2.3 Wide field optical imaging of A963 and A2192	66
2.4 Additional data	77
3 Results and Discussion	79
3.1 Analysis of A520	79
3.2 Analysis of A963	97
4 Conclusions	109
References	111
Summary in Estonian	121
Acknowledgements	123
Attached original publications	125
Curriculum vitae	193
Elulookirjeldus	197

List of original publications

This thesis is based on the following publications:

- I **Deshev, Boris**; Finoguenov, Alexis; Verdugo, Miguel; Ziegler, Bodo; Park, Changbom; Hwang, Ho Seong; Haines, Christopher; Kamphuis, Peter; Tamm, Antti; Einasto, Maret; Hwang, Narae; Park, Byeong-Gon 2017, *Galaxy evolution in merging clusters: The passive core of the "Train Wreck" cluster of galaxies, A 520*, Astronomy & Astrophysics, 607, A131
- II Jaffé, Yara L.; Verheijen, Marc A. W.; Haines, Chris P.; Yoon, Hyein; Cybulski, Ryan; Montero-Castaño, María; Smith, Rory; Chung, Aeree; **Deshev, Boris**; Fernández, Ximena; van Gorkom, Jacqueline; Poggianti, Bianca M.; Yun, Min S.; Finoguenov, Alexis; Smith, Graham P.; Okabe, Nobuhiro 2016, *BUDHIES - III: the fate of H I and the quenching of galaxies in evolving environments*, MNRAS, 461, 1202J
- III Jaffé, Yara L.; Poggianti, Bianca M.; Verheijen, Marc A. W.; **Deshev, Boris**; van Gorkom, Jacqueline H. 2013, *BUDHIES I: characterizing the environments in and around two clusters at $z \simeq 0.2$* , MNRAS, 431, 2111J
- IV **Deshev, B.**; Park, C.; Hwang, H. S.; Ziegler, B.; Verdugo, M.; Kamphuis, P.; Finoguenov, A.; Tenjes, P.; Tamm, A. 2016 *Building Up a Cluster: The Case of A520*, ASP, 507, 237D

Other related publications of the dissertant:

- V Einasto, Maret; Gramann, Mirt; Park, Changbom; Kim, Juhan; **Deshev, Boris**; Tempel, Elmo; Heinämäki, Pekka; Lietzen, Heidi; Lähteenmäki, Anne; Einasto, Jaan; Saar, Enn 2018, *Supercluster A2142 and collapse in action: infalling and merging groups and galaxy transformations*, Astronomy & Astrophysics, 620A, 149E
- VI Einasto, Maret; **Deshev, Boris**; Lietzen, Heidi; Kipper, Rain; Tempel, Elmo; Park, Changbom; Gramann, Mirt; Heinämäki, Pekka; Saar, Enn; Einasto, Jaan 2018, *Infalling groups and galaxy transformations in the cluster A2142*, Astronomy & Astrophysics, 610A, 82E
- VII Cybulski, Ryan; Yun, Min S.; Erickson, Neal; De la Luz, Victor; Narayanan, Gopal; Montaña, Alfredo; Sánchez, David; Zavala, Jorge A.; Zeballos, Milagros; Chung, Aeree; Fernández, Ximena; van Gorkom, Jacqueline; Haines, Chris P.; Jaffé, Yara L.; Montero-Castaño, María; Poggianti, Bianca M.; Verheijen, Marc A. W.; Yoon, Hyein; **Deshev, Boris Z.**;

Harrington, Kevin; Hughes, David H.; Morrison, Glenn E.; Schloerb, F. Peter; Velazquez, Miguel 2016, *Early Science with the Large Millimeter Telescope: COOL BUDHIES I - a pilot study of molecular and atomic gas at $z \simeq 0.2$* , MNRAS, 459, 3287C

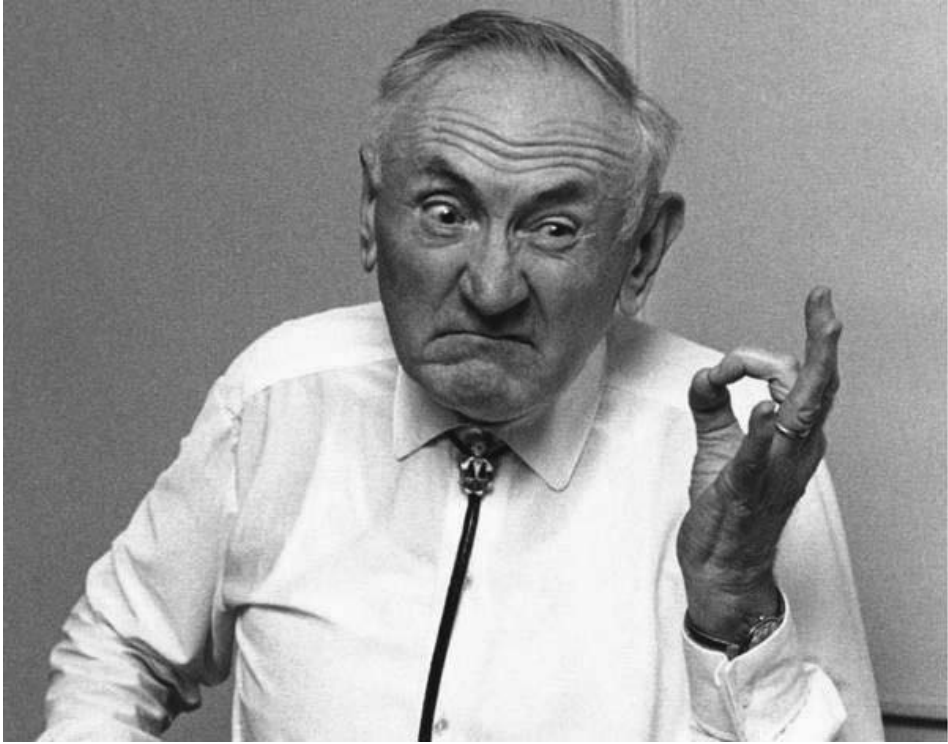
Author's contribution to the publications

Author has made considerable contributions to the following original publications. The following list gives details on the author's work in each of the papers. The Roman numerals correspond to those in the list of publications.

Publication I. The author designed the project, wrote the proposal to gather the main data set used in the publication, single-handedly processed the data and executed all of the analyses presented in the publication. The author wrote all the text in the publication.

Publication II and III. The author processed two of the main data sets used in the publications, namely the 21 cm spectroscopy and the optical imaging. He took part in the planning and writing of the proposal for the spectroscopic data set. He took part in the analysis and the discussions helping to improve the text during the publication process.

Publication IV. This publication is a proceeding from a conference. The data used is the same as in publication I which the author fully processed. The poster presentation at the conference and the text of the publication were done entirely by the author.



"... Zwicky was here first."

(Butcher & Oemler 1984)

1

Introduction¹

THERE are only a handful of non-stellar objects visible with unaided eye from our planet. Excluding planets, early observers referred to those as *nebulae* (Latin for "cloud" or "fog"). These include stellar clusters, planetary nebulae, regions of star formation and galaxies, among others. This book is about galaxies. Galaxies are the building blocks of the universe. There are only three galaxies visible without a telescope – M31 and the Large and Small Magellanic Clouds. Shortly after the invention of the telescope, observers started to catalogue the positions and appearances of the nebulae. Traced by the distribution of baryonic matter within them, and in particular by the stars which are readily observable at optical wavelengths, the non-uniform distribution of galaxies on the sky was noticed very early. In 1781 Charles Messier noticed that 13 of the 103 nebulae in his catalogue were in the constellation of Virgo, thus he was likely the first person to observe a cluster of galaxies. Shortly after that, the body of data, recording the positions of known nebulae, reached into the thousands of objects, thanks to the work of Sir William Herschel and his son John. By 1847, when John Herschel completed his survey of the southern sky, Herschel's catalogue contained around 4000 objects. In 1888 Drayer's New General Catalogue contained 7840 non-stellar objects. Shortly after that the numbers rose to hundreds of thousands (Campbell 1915).

In 1869, Proctor's chart was published showing the distribution of star clusters and nebulae (Fig. 1.1). Fig. 1.2 shows the distribution of faint nebulae observed at Mount Wilson observatory, published around the end of the 19th century. Note the enhancement associated with the Virgo and Coma clusters close to the position of the North galactic pole (marked as N on the Figure). The thick line shows the plane of the Galaxy.

As soon as the first observations were made, people started debating how far away the nebulae are and what their nature is. The word galaxy (from Greek $\gamma\alpha\lambda\alpha\xi\iota\alpha\zeta$ – milky) was probably first used around the middle of the 19th century to describe our Galaxy and some other nebulae, when an ever greater number of people were becoming convinced that not all nebulae share a common nature. At that time, Keeler started systematically photographing of nebulae and he was

¹The brief review of the historical facts surrounding the build-up of knowledge about the nature of galaxies and extragalactic structures, presented in this chapter, reflects only the modest knowledge of the author who makes no claims for completeness.

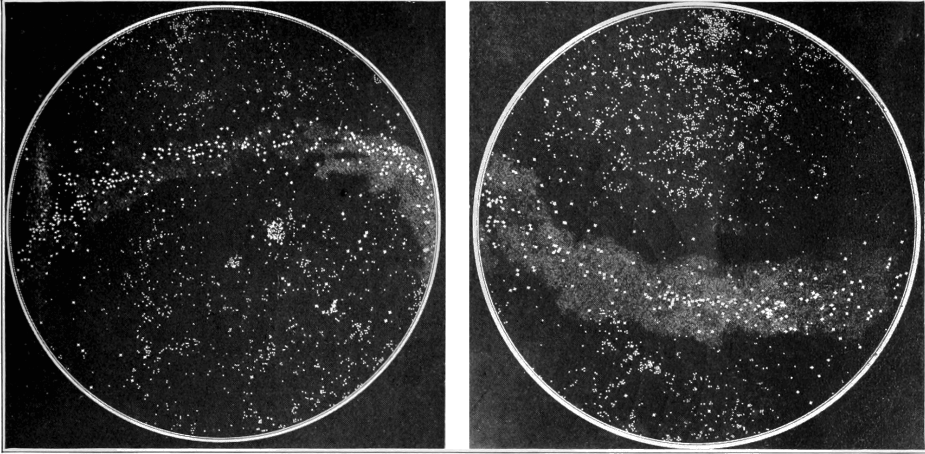


Figure 1.1: Distribution of nebulae (marked by dots) and star clusters (marked by crosses), published by Richard Anthony Proctor circa 1869.

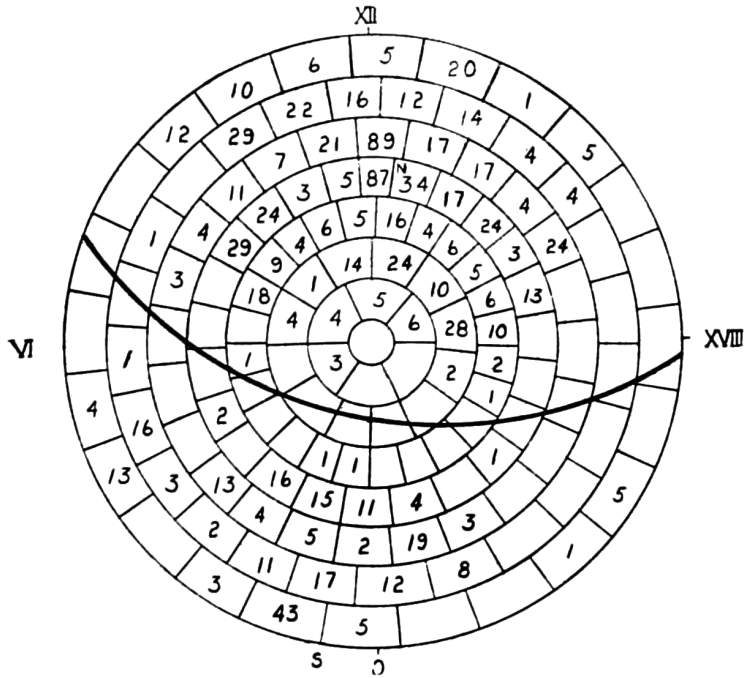


Figure 1.2: Distribution of faint nebulae observed at Mount Wilson. The thick line shows the galactic plane.

one of the first to observe that many of the nebulae show a spiral structure. Lord Rosse's observations also revealed this, which he interpreted as indication of rotation. The top panel of Fig. 1.3 shows an image of M51 (NGC 5194, a.k.a. Whirlpool galaxy) drawn by Lord Rosse following his observations of this galaxy, which were probably the first to reveal its spiral arms. For the pleasure of the reader we also print a modern false-colour image of M51 combining images taken with the Hubble Space Telescope's Advanced Camera for Surveys in four filters – B, V, I and H α .

Using the newly available measurements of spectra of nebulae (William Huggins, 1864), and by separating the nebulae into different types according to their appearance and distribution on the sky, Cleveland Abbe (1867) concluded that some are indeed located outside the Galaxy. The debate about the distance to the nebulae went back and forth for a considerable time, until eventually it was resolved by the precise measurements of distances to some nebulae by Hubble (1925a,b) based on Cepheid variable stars identified within them. Later on, the redshift-distance relation (Hubble & Humason 1931), now known as the Hubble-Lemaître law, revealed the expansion of the universe and is now widely used as the main distance indicator for galaxies beyond the local universe.

A debate followed, as to the distribution of galaxies in the universe and a search for a distance scale over which their distribution is uniform – which continued well into the late 20th century. The monopolistic nature of gravity, to a large extent, predetermines the cellular nature of the large scale distribution of matter in the universe (Joeveer & Einasto 1978), once the primordial density fluctuations were seeded (van Albada 1960, 1961; Peebles 1970; White 1976). There exist overdensities which can only grow at the expense of lower density regions. The expansion of space serves to slow down this process and arrest it at larger scales, but gravitationally bound systems remain that way even in the presence of inflation. The hierarchical scenario, where small structures form first and then grow by merging, means that mergers between galaxies, groups, and clusters of galaxies are relatively commonplace in the universe, with the halo mass function (Tinker et al. 2008) governing the relative frequency with which mergers of various mass ratios are occurring (McGee et al. 2009). This accretion of matter onto larger structures, and in particular the mergers of structures with approximately equal mass, represents the stage on which some aspects of the evolution of galaxies analysed in this book, unfolds.

Shortly after the abundance of galaxies in the universe was confirmed, the tendency of galaxies of elliptical types and higher masses to cluster more strongly than the spiral and lower mass ones was noticed and published by Zwicky (1938). Fritz Zwicky was also the first to notice the presence of large amounts of unseen matter that interacts gravitationally with visible matter (Zwicky 1937, see also Zwicky (1933) (in German)). This morphology-density relation was quantified for the first time by Dressler (1980) and later confirmed by numerous other studies and extended over a wide range of galaxy densities (Postman & Geller 1984; Fukugita et al. 2007; Bamford et al. 2009).

It is now established that the stellar mass of a galaxy plays an important role



Figure 1.3: *Top* Image of M51 drawn by Lord Rosse. Picture from the Birr Castle archives. Picture credit: John C McConnell. *Bottom* Image of M51 taken with HST. Image credit: NASA, ESA, S. Beckwith (STScI), and The Hubble Heritage Team (STScI/AURA)

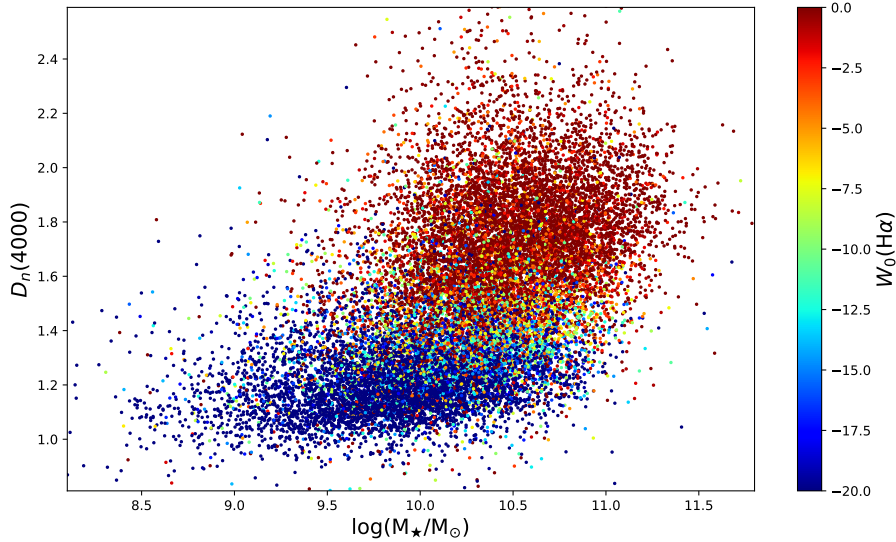


Figure 1.4: The distribution of ~ 18500 galaxies from the ACReS survey on the plane relating the age of their light-dominating stellar population ($D_n(4000)$ see Sect.3.1.1) with their total stellar mass. The equivalent width of the $H\alpha$ emission line which is a good indicator for ongoing star formation is colour coded.

in determining its morphology and star formation properties (see e.g. Kauffmann et al. 2003; Baldry et al. 2006; Peng et al. 2012). The term "mass quenching" is often used to describe this. As the term suggests galaxies with larger stellar masses tend to be older and, on average, more quiescent. Fig. 1.4 demonstrates this using part of the data and measurements used in this thesis and presented in Section 2.4. The figure shows ~ 18500 galaxies distributed on the plane relating the age of their light-dominant stellar population (expressed with the $D_n(4000)$ index, (Bruzual A. 1983; Poggianti & Barbaro 1997; Balogh et al. 1999)) and their total stellar mass. The colour of each point shows the strength of the $H\alpha$ emission line in their spectra (note that $W_0(H\alpha)$ index is negative when the line is in emission), which correlates well with the rate of ongoing or recent (age < 100 Myr) star formation (Kennicutt & Evans 2012). While completeness can play a role at low stellar masses, it is obvious that as we move up the mass range, a greater fraction of galaxies show increased stellar age and decreased ongoing star formation. At $M_* > 10^{10.5} M_\odot$ the majority of the galaxies have $D_n(4000) > 1.5$, while the opposite is true below that stellar mass. We choose to show a relatively narrow range of $H\alpha$ equivalent widths. Below $\sim 5\text{\AA}$ galaxies are considered non-star forming, since such low levels of emission can also come from evolved stellar populations (Cid Fernandes et al. 2011; Papaderos et al. 2013). We cut the upper end at -20\AA , which shows a certain presence of young stars (AGNs are not shown on the Figure), although $W_0 H\alpha$ reaches $\sim -2000\text{\AA}$ in this data set. Note that, although galaxies with intermediate $W_0 H\alpha$ values can be found over the entire plane of the figure, they tend to concentrate in the gap between the galaxies with high and low

$D_n(4000)$.

Alongside stellar mass, it has long been recognised that the environment of galaxies also plays a role in determining their properties (see e.g. Boselli & Gavazzi 2006, for an exhaustive review on environmental effects on late type galaxies), in addition to the expected from the mass segregation with environment noted by Zwicky (Dressler 1980; Bamford et al. 2009; Peng et al. 2010). A number of physical mechanisms have been proposed that can drive the environmental quenching of galaxies. The most commonly invoked ones are – ram-pressure stripping (Gunn & Gott 1972, RPS,) and starvation (a.k.a. strangulation) (Larson et al. 1980), both of which alter the gas content of the galaxies, and with that, their ability to form new stars. Dynamical processes that can alter inter-stellar matter (ISM) as well as stellar distribution are mergers and tidal interactions, both with other galaxies (Spitzer & Baade 1951; Richstone 1976) and with the cluster potential (Merritt 1983; Byrd & Valtonen 1990). Mergers are efficient only in low mass groups and pairs of galaxies but tidal interactions can have significant effects on morphology and star formation (Hwang et al. 2018). While RPS has actually been observed at work (Kenney et al. 2004; Poggianti et al. 2017), it is expected to only affect galaxies infalling into relatively large clusters. Starvation seems to be very dominant in a range of environments (Peng et al. 2015).

As part of a remarkable series of articles, Butcher & Oemler (1984) (BO84 hereafter) paper is important to us for many reasons. It introduces the effect – now known as, Butcher–Oemler effect, which represents the observational fact that the fraction of blue galaxies in distant clusters increases with a cluster’s redshift. BO84 split the clusters in their sample according to how centrally concentrated the distribution of galaxies is in them. With this they also connect the global distribution of cluster members on the sky with the fraction of star forming galaxies among them. This suggests that the redshift is not the only factor determining the fraction of star forming galaxies in a given cluster, and other, cluster specific, processes also play a role. These processes must be related to the formation/accretion history of the clusters (Poggianti et al. 2006). BO84 do indicate that the observed tendency of open (as opposed to concentrated) clusters to harbor more star forming galaxies was known already to F. Zwicky. The analysis presented in this book follows in the footsteps of the analysis presented by BO84. Among all other connections BO84 also introduce the two protagonists in this book. The clusters Abell 963 (A963) and Abell 520 (A520) are the main subjects of the research presented here and they are also part of BO84’s sample. They feature prominently on Fig. 1.5 as both clusters are almost exactly at $z = 0.2$ and the two straddle almost the entire scatter of the Butcher–Oemler effect at that redshift. Intriguingly, BO84 split their sample in three bins of concentration with A520 falling into the intermediate bin. Taken individually (dashed circles on Fig. 1.5), all the clusters in this bin show a decreased f_B when compared with the compact clusters. However, given the large contrast between the open and compact clusters the authors considered the intermediate bin to be part of that of compact clusters.

Systematic studies on the effects of cluster mergers on their constituent galaxies started relatively recently and while we are still missing a large cata-

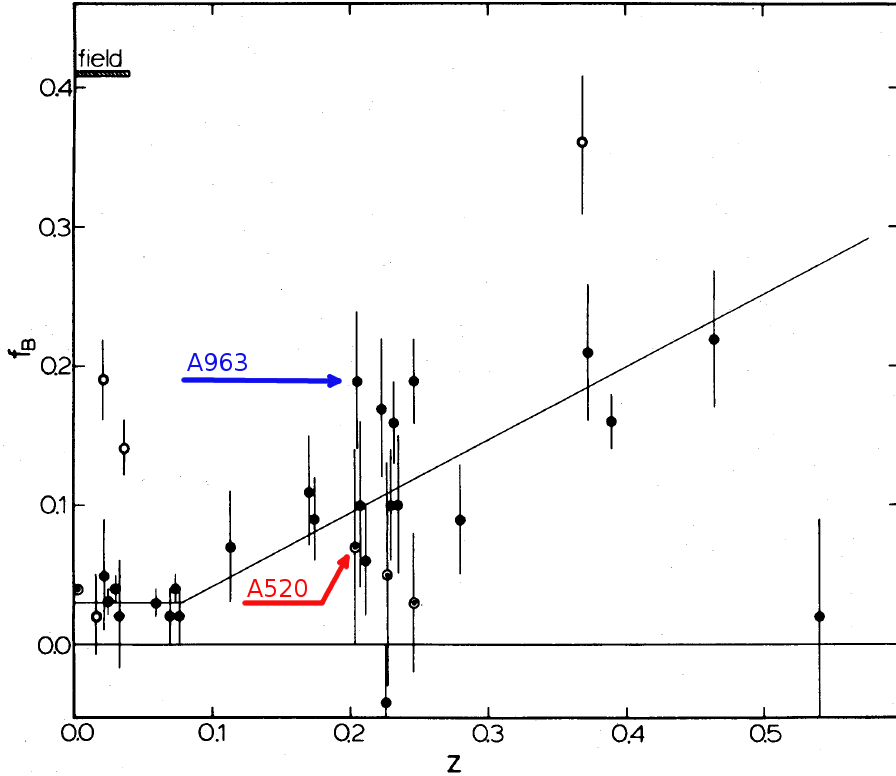


Figure 1.5: The Butcher–Oemler effect (Figure from Butcher & Oemler (1984) with added labels), showing the fraction of blue galaxies in clusters as a function of the redshift of the cluster. The points showing the positions of A963 and A520 are annotated.

logue of merging clusters of any completeness the number of recognised cluster mergers is growing rapidly ("MC² – The merging clusters collaboration" – <http://www.mergingclustercollaboration.org>). An effort is being made to catalogue all merging clusters in the SDSS area (Tempel et al. 2017), but with little success. Part of the difficulty in creating of such catalogues comes from the variety of observational evidence that would allow one to recognise an ongoing merger. There are many: an offset between the X-ray-emitting gas and the brightest cluster galaxy (BCG) (Coziol et al. 2009; Skibba et al. 2011; Martel et al. 2014), an offset between the X-ray emitting gas and the overall galaxy distribution (Markevitch et al. 2005), clustering of the galaxies projected on the sky or in phase space (Czoske et al. 2002; Girardi et al. 2008; Tempel et al. 2017), properties of the radio continuum and X-ray emission (Govoni et al. 2004; Feretti et al. 2012), to name and cite a few. All these are sensitive to different orientations between the line of sight and the merger axis, and/or different time before or after the core passage, as well as different mass ratios of the merging components. There is even a variety of definitions as to what constitutes a merging cluster. Sometimes the presence of substructure is taken as an indication of merging, while sometimes

Parameter	A963	A520
z	0.205 ^(a)	0.201 ^(a)
Richness class	3 ^(b)	3 ^(b)
R_{200}/Mpc	2.68 ^{+0.37} _{-0.14} (a)	2.32 ^{+0.23} _{-0.22} (a)
$M_{200}/10^{14}M_{\odot}$	17.9 ^{+7.5} _{-2.4} (a)	11.6 ^{+3.7} _{-3.0} (a)
$\sigma_v/\text{km s}^{-1}$	1199 ⁺¹¹² ₋₁₁₂ (a)	1036 ⁺¹⁰¹ ₋₉₇ (a)
R_{500}^{WL}/Mpc	1.185 ^(c)	1.208 ^(c)
$M_{vir}^{WL}/10^{14}M_{\odot}$	12.3 ^{+3.0} _{-3.0} (c)	15.3 ^{+3.0} _{-3.0} (c)
$L_{X,bol,500}/10^{45}\text{erg s}^{-1}$	1.96±0.04 ^(d)	1.75±0.04 ^(d)
$T_{X,500}/\text{keV}$	6.2±0.2 ^(d)	7.8±0.4 ^(d)
Concentration	0.60 ^(e)	0.38 ^(e)
f_B	0.19±0.05 ^(e)	0.07±0.07 ^(e)
f_{SF}	0.27(0.41)±0.04 ^(f)	0.09(0.28)±0.04 ^(f)

Table 1.1: Main properties of A963 and A520

Notes:(a) - Paper I; (b) - Abell (1958); (c) - Hoekstra et al. (2015); (d) - Mahdavi et al. (2013); (e) - Butcher & Oemler (1984); (f) - this work. The numbers in brackets are calculated over the whole cluster.

a merger of semi-equal mass components is required. Similarly, studies on the effects of cluster mergers on their constituent galaxies are also based on a variety of methods, which can explain the variety of results obtained. The majority of the studies agree that cluster mergers do inspire star formation (Bekki 1999; Miller & Owen 2003; Ferrari et al. 2005; Owen et al. 2005; Hwang & Lee 2009; Cohen et al. 2014; Stroe et al. 2015). There are also studies showing that mergers make little difference (Chung et al. 2009), and some that show a decrease in star formation activity – Poggianti et al. (2004), and Paper I.

There are many studies dedicated to the Butcher–Oemler effect, mostly confirming its presence (Margoniner & de Carvalho 2000; Margoniner et al. 2001; Haines et al. 2009) although different results are also present (Andreon & Etori 1999; Andreon 2006; Andreon et al. 2006). While most analyses agree that the usage of optical imaging to measure blue fractions in clusters (as in BO84) leads to a bias (Smail et al. 1998; De Propriis et al. 2003; Haines et al. 2009), they also agree that the Butcher–Oemler effect is real, although the evolution with redshift is not as strong as suggested in the BO84 paper. The dynamical status of clusters has often been invoked to explain the large scatter of the Butcher–Oemler effect, with the younger, unsettled clusters showing a larger blue fraction (Dwarakanath & Owen 1999; Miller & Owen 2003; Miller et al. 2006, BO84).

Table 1.1 lists some of the main parameters of the clusters A520 and A963. At first glance, A963 and A520 appear to be very similar. Their redshift, richness class, velocity dispersion, total mass and X-ray luminosity are very similar. Even the difference between the masses estimated by different methods for the two clusters are similar. The only really stark difference between the two clusters is their concentration, measured by BO84 and indicated on Fig. 1.5 with the

different symbols used for the two clusters. The different distributions of their member galaxies on the sky are now confirmed by the fact that A963 is considered a relatively relaxed cluster (Allen 1998; Smith et al. 2005) while A520 is known to be a major merger of at least two sub-clusters of approximately equal mass. This merger is accompanied by a number of other, smaller infalling structures (Markevitch et al. (2005); Mahdavi et al. (2007); Girardi et al. (2008); Jee et al. (2012, 2014); Wang et al. (2016), Paper I). Of course, the other stark difference between the two clusters is the fraction of blue galaxies among their members, which is the very reason why we choose to analyse them. Below the f_B from BO84 in Table 1.1 we print our estimate of the fraction of star forming galaxies f_{SF} (with emission lines). The numbers are calculated inside R_{500} , which is a close match to the area observed by BO84. The numbers in brackets include all the cluster members out to $3 \times R_{200}$. Note that A520 demonstrates a much larger drop in f_{SF} than A963 when comparing the cluster as a whole and its core. A more detailed comparison between the two clusters is presented in Chapter 3.

We undertook the research presented in this thesis with the following main goals in mind:

- Analyse the effects that cluster mergers have on member galaxies
- Estimate the gas content of the galaxies responsible for the elevated blue fraction in A963, and use that to shed some light on the reasons behind the Butcher–Oemler effect.
- Analyse the scatter in the Butcher–Oemler effect by comparing A963 and A520

To achieve our goals we employ a large set of multi-wavelength data, including optical imaging and spectroscopy of tens of thousands of galaxies at intermediate redshifts. We make use of a unique data set, comprising the deepest H I data cubes ever created, in terms of the noise level reached. To this we add the use of all-sky survey like SDSS. These data are presented in details in Chapter 2. In Chapter 3 we present the results of our analysis which have been published in Papers I, II, and III, as well as some new, unpublished, results. We summarise our conclusions in Chapter 4. The three articles on which this thesis is based are printed in their published form at the end of the thesis. Throughout this thesis we use standard Λ CDM cosmology with $\Omega_M = 0.3$, $\Omega_\Lambda = 0.7$, and $H_0 = 70 \text{ km s}^{-1} \text{ Mpc}^{-1}$.

With utmost modesty we conclude this Chapter with a direct quote from BO84: "We cannot end this discussion without noting that, as usual, Zwicky was here first."

2

Data

THE work presented in this thesis is based mainly, but not only, on the three observational data sets presented in this chapter.

2.1 Multi-fibre spectroscopy of galaxies in A520

2.1.1 Target selection

THE target selection is done in several steps, based on archival CFHT, Megacam images in g' and r' filters. Prior to the target selection the two images were astrometrically calibrated using the positions of point sources from the 2MASS (Skrutskie et al. 2006) survey. Guide stars were also selected from the same survey.

We performed photometry on those images with SExtractor using MAG_AUTO magnitudes. All the targets for which high quality photometry could not be made due to presence of bright neighbors (extraction flag 1) were removed. Although this does remove some of the already confirmed cluster members (Girardi et al. 2008) it does not introduce bias in our target selection. The point sources were selected from a total magnitude - half light radius plot and removed from the target list. The next step was based on the color - magnitude diagram shown in Fig. 2.1. The gray points show all the sources extracted from the CFHT images. The \bullet and \times symbols are the members and non-members (respectively) with spectroscopy available from the literature. The black polygon shows the region from which we draw our sources. The faint magnitude limit is set equal to the completeness limit of the currently available spectra. This is also the magnitude limit of the Rines et al. (2013) survey performed with the same telescope + instrument, which we use as a guidance for the instrument performance. For spectroscopic studies, one hour integration time should provide sufficient signal to noise ratio in absorption for redshift estimation of targets with $r' < 21$. The selection is $16.5 < r' < 21$ and $0.3 < g' - r' < 1.3$, which encompasses the entire red sequence and the blue cloud of the confirmed cluster members. In order to remove any foreground contamination we limit the selected sources by their angular size on the sky, selecting sources with 50% flux radius (R_{50}) smaller than $1.25 R_{50}$ of the largest confirmed cluster member. Note that all the targets have sizes on the sky significantly exceeding the fibre diameter of $1.5''$. After that we remove all

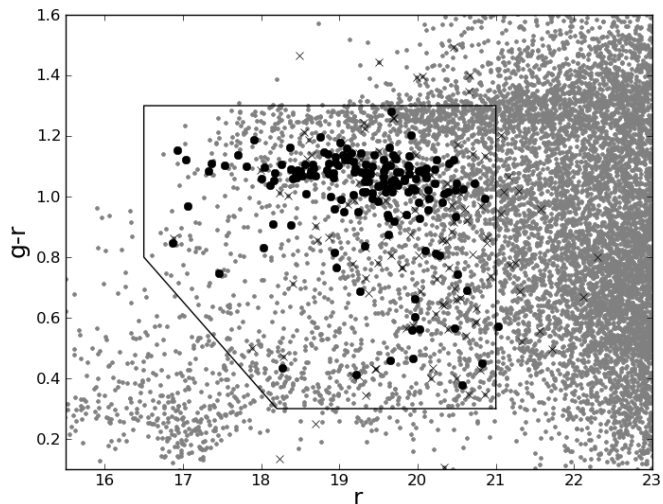


Figure 2.1: Selection of targets by optical colour and magnitude. The gray points are all the sources extracted from the CFHT images. The \bullet and \times symbols are the spectroscopically confirmed members and non-members, respectively. The black polygon shows the region from which we are selecting targets.

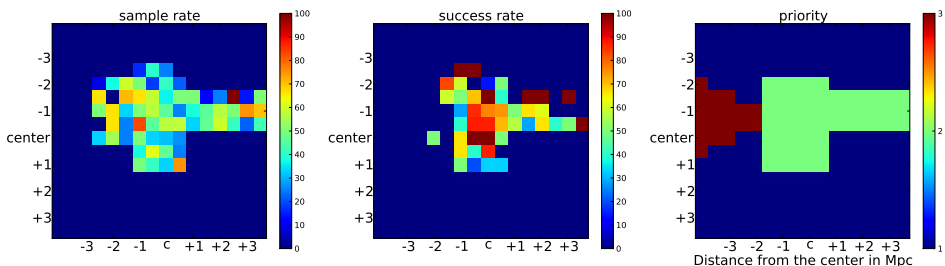


Figure 2.2: *{Left}* The rate at which the potential targets are sampled by the existing spectroscopy data. *{Middle}* The fraction of cluster members among the objects with available data. The increase of the success rate toward the edges of the sampled region is a result of the binning. *{Right}* Distribution of the priorities on the sky, with 1 being the highest. These are regions with high success rate and low sampling rate. The tail toward the left, even though well sampled, contains no cluster members, hence it has the lowest priority.

the confirmed non-members from the target list.

After applying these criteria we have 2523 potential targets, to which we assign priorities aimed at maximising the fraction of cluster members from the observed galaxies. The priorities are set taking into account the available spectroscopic data as shown in Fig. 2.2, for the targets with cluster-centric distance $R_{clust} < 3$ Mpc. First the fraction of the potential targets with available data is calculated for different parts on the system, to estimate the sampling rate of the current data.

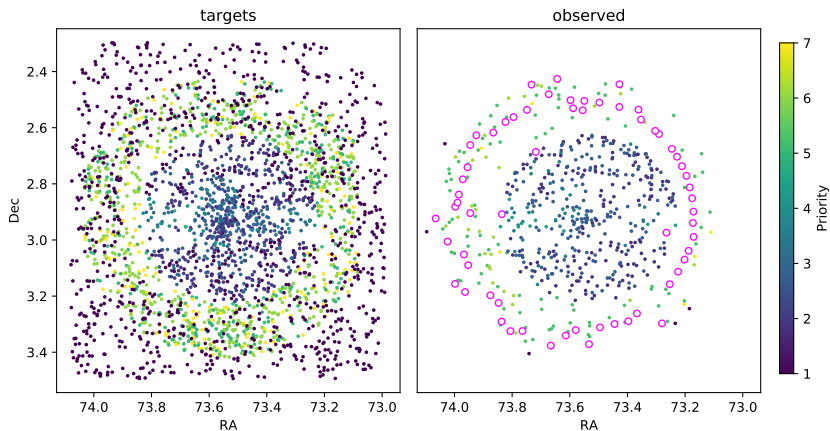


Figure 2.3: The distribution on the sky of all the targets (left) and the 523 fibres assigned to targets (right) with their priorities. The magenta circles on the right hand side plot show the positions of the 62 sky fibres.

This is shown on the left hand side of Fig. 2.2. Then the success rate (fraction of cluster members among the current data) is calculated, and plotted in the middle panel. The right hand side of the figure shows the assigned priorities in different parts of the cluster. The highest priorities (1) are given to the regions not sampled by the available data. Lower priorities (2 and 3) are given to the sampled regions and the regions with the very low success rate, respectively. Note the region to the east of the cluster center (left on the plot) that have the lowest success rate (0 members out of > 10 available redshifts), even though the sampling rate is similar to the rest of the cluster.

Additionally the priority of a given target is decreased by 1 if its magnitude within an aperture of $1.5''$, equal to the diameter of the fibres, $r'_{1.5}$ is below 20% of the dark sky brightness, and by 2 if it is below 20% of the gray sky brightness (see Fabricant et al. 2005, for description of the instrument capabilities). The priority is also decreased by 1 if the object has been observed already by Girardi et al. (2008), as these data are publicly available. Additional targets with cluster-centric distances $3 < R_{clust} < 5$ Mpc were added in order to make a full use of the 300 available fibres while satisfying positioning limitations of Hectospec (minimum fibre separation of $20''$). Those satisfy the same magnitude and size criteria and were entered with priorities lower than the targets with $R_{clust} < 3$ Mpc. The so produced catalogue contains 129 of the 167 cluster members confirmed by Girardi et al. (2008), with the majority of the remaining 38 being excluded by the requirement for a high quality photometry. Eventually we observed 52 of those for calibration purposes.

After that, the list of targets is fed into the fibre assignment program *xfit-fibs*. The distribution of the targets with their priorities and the assigned fibres are shown on Fig. 2.3. The right hand side of the figure includes the 62 fibres dedicated to sky measurements, shown with a large magenta circles.

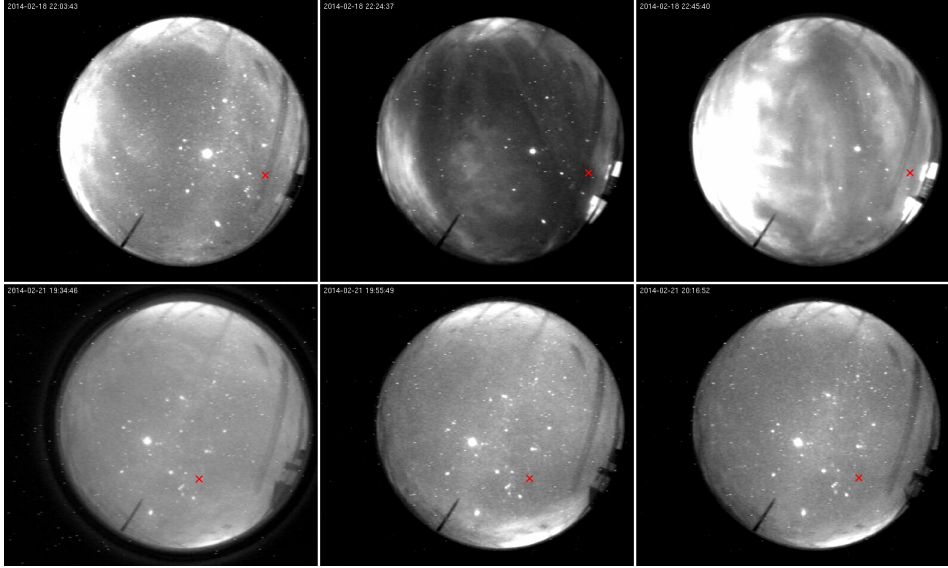


Figure 2.4: All-sky images, taken at the end of each science exposure, showing the sky conditions. The date and local time are indicated in the top left corner of each image. The images are with matched intensities and all the differences are due to varying sky conditions. The approximate position of A520 is indicated with the red \times on each frame. The bright object near the center of each frame is Jupiter. Note the high airmass and cloud cover during the first night (top row).

2.1.2 Data acquisition and processing

The two fibre configurations were observed with the MMT¹ in service mode on 19-th and 22-nd of February 2014. Three consecutive 1200 sec exposures were acquired in each configuration for a total integration time of 1h per galaxy. The site conditions were less than perfect, particularly during the first observing night. The target was at airmass between 1.4 and 1.6 and with seeing $\sim 1.2''$, some clouds were present during all three exposures (see Fig. 2.4). The second fibre configuration was observed at airmass ~ 1.15 with thin high clouds and a seeing $\sim 1''$. The observations were done with grism 270 with a resolutions of 6 \AA (1.2 \AA pix^{-1}). The spectral coverage is from 3650 to 9200 \AA centered on 5770 \AA . No filters were used. From the 300 fibres available, 32 and 30 were used for sky emission in the first and second observing night, respectively. There were 15 unused fibres in total between the two configurations. The data processing was done in IRAF with the occasional use of our own python tasks. We did not use the Hectospec pipeline SPECROAD (Mink et al. 2007), although we did closely follow its ideology.

¹Observations reported here were obtained at the MMT Observatory, a joint facility of the University of Arizona and the Smithsonian Institution.

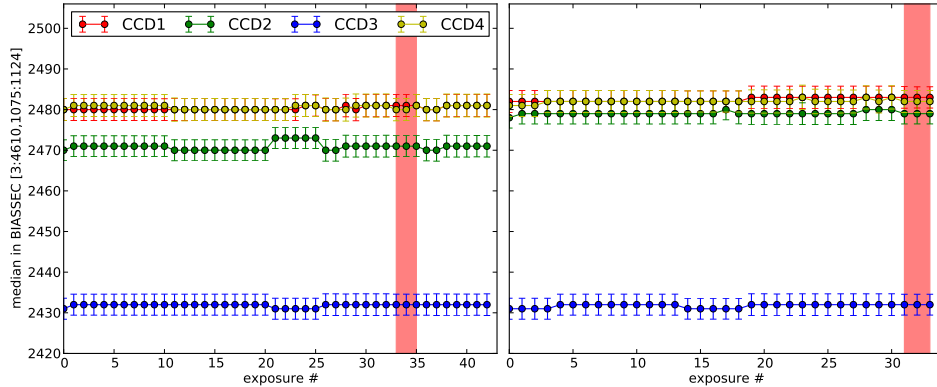


Figure 2.5: The median of the overscan region for all the frames used from the two nights and the corresponding rms noise after the *preampfix* correction. The frames from 19-th of February are on the left hand side and those from 22.Feb on the right hand side of the figure. The red shaded region indicates the science exposures. The exposures following the science ones on the left hand side are sky flat fields.

Overscan and bias subtraction

Prior to any processing of the Hectospec data, a correction have to be made for the time-constant problem of the amplifiers (<http://www.cfa.harvard.edu/mmti/hectospec/hecto-reductions.htm>). This was done in python in the fashion of the *preampfix* task from the Hectospec pipeline. A visual inspection confirmed that the overscan regions of all the files are free of any signal. Before this correction an additional signal and a visible structure along the readout direction was apparent in the overscan of the dome and sky flat fields. The median values in the overscan of all the exposures after this correction is shown in Fig. 2.5. After that a constant value overscan was subtracted, the bad pixels were fixed by linear interpolation from the neighboring pixels and the images were trimmed.

The so processed bias frames showed a very constant pattern allowing us to make one master bias from 21 of the 22 available bias frames from both nights (one image was discarded for showing pattern different from all the rest). The large number of combined bias read-outs minimizes the bias subtraction contribution to the error budget of the recovered scientific parameters from the data. The master bias frame was done within *zerocombine*, IRAF with median combination with sigclip type of rejection, set at 4σ . This master bias was visually inspected and subtracted from all the remaining frames.

Dark current

A series of 5 dark current measurements were acquired by the observing team after completing each night's program. Two different exposure times were used - 900sec during the first night and 1200sec during the second one. Figure 2.6 shows the mean dark current in 1200sec (the length of our scientific exposures),

and rms (read-out noise) in bins spanning 200 pixels along the dispersion axis (Y) and the full width of the CCD (1024 pixels) along the X axis. Those are calculated with 3 iterations of 3σ clipping. The dark frames from the first night show dark current higher than the one measured during the second observing night. The difference is $\sim 2 \times$. All 10 dark current frames however, show a dark current of $< 1e^{-h^{-1}}$ except in the first bin of 200 pixels in the red end of the dispersion axis. During the acquisition of all the dark current frames the CCD temperature was stable within 0.05K. Hectospec is known for a negligibly low dark current rate, as well as a light leakage from its shutter (Hectospec Observers Reference Manual). We assume that this is probably the cause for the elevated dark current from the first night. We could not determine the source of the increased dark current and read-out noise over the first 200 pixels, but it could also be caused by a light leakage. The web documentation of the instrument (<http://www.cfa.harvard.edu/mmti/hectospec/hecto-reductions.htm>) points out a light leak in the red end for some of the fibres, which renders the data redward of 8500 Å unusable. This is exactly the region where we find the elevated dark current. Given the overall very low level of dark current in the usable region of all four CCDs we decided not to subtract a noisy dark current image.

Pixel-to-pixel variations and fringing

All the images were corrected for gain variations between the separate amplifiers and all four read-outs were joined into a single image. We produced and visually inspected a set of ratio images for all the available dome flat field images. All but four of those were medianly combined into a master dome flat, excluding the few files with illumination deviating from the rest by more than 10%. The IRAF task *apflatten* was used to fit and subtract the light from the dome flood lamps, and create a normalized pixel-to-pixel sensitivity variation map, which also includes the fringing pattern noticeable redward of 6500 Å (see Fig. 2.7). We did produce two separate maps, one for each observing night, and after confirming their similarity decided to produce one such map for the entire observing run. The task *apflatten* calls on *apall* to find and trace the 300 apertures containing the spectra from all the fibres in the master dome flat field image. The width of the apertures was set equal to the FWHM, which should minimize the contamination from the adjacent apertures to $< 1\%$. After that it extracts the spectra and fits it with a spline3 function of order 70. This is then subtracted to leave only the pixel sensitivity variations and the fringe pattern. Producing an entire image, rather than extracting the flatfield spectra, appears to work better because of the wanderings of the images on the CCDs. According to the SPECROAD pipeline manual this method of removing the fringe pattern is good to within 1-2%. The so produced map is shown on Fig. 2.7 and is divided into all of the remaining frames.

Cosmic ray removal

Before combining the individual exposures, the cosmic ray events had to be cleaned. The events were detected on a image of the variance between a median image and every 20min. exposure. The cut-off level in the variance was manually

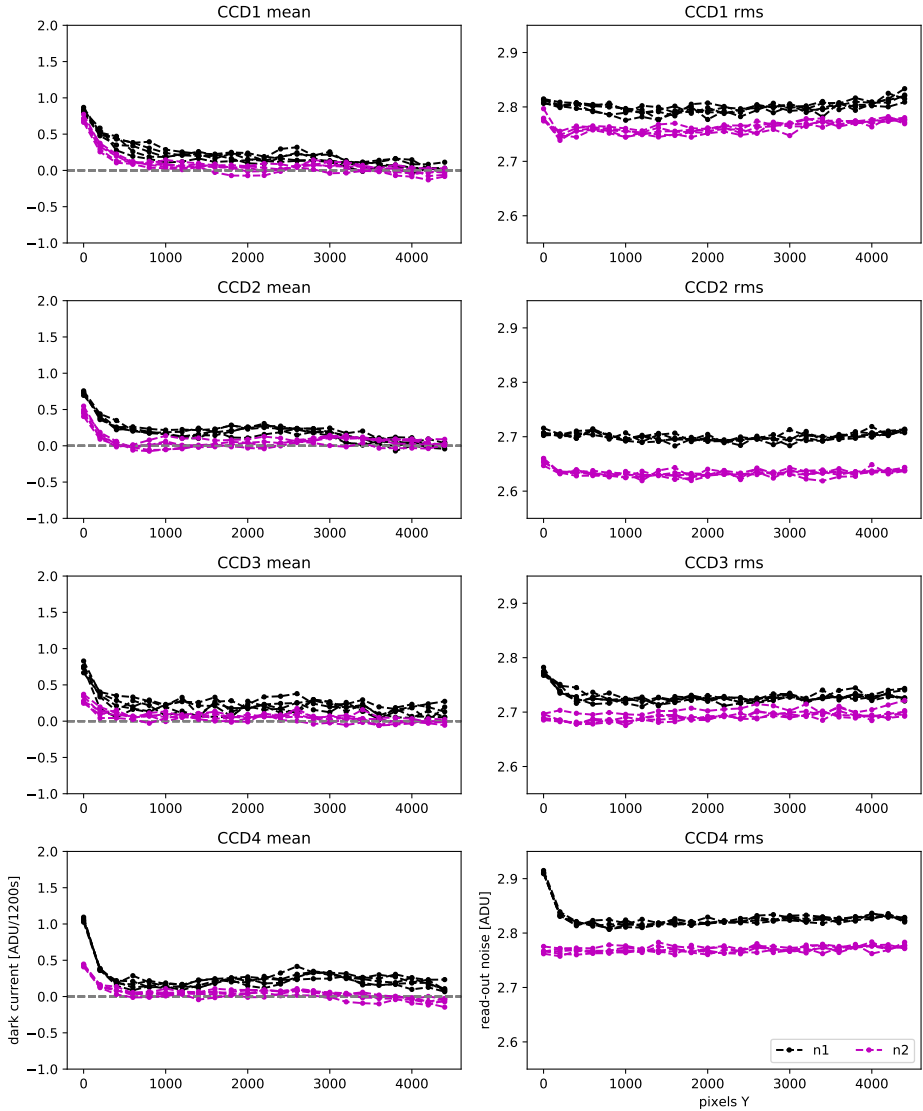


Figure 2.6: The mean (left) and the rms along the Y direction of all the dark frames acquired during both observing nights. The values are calculated in bins spanning the full 1024 pixels in X direction and 200 pixels in Y, with 3 iterations of 3σ clipping. The values from the first night are converted to 1200 seconds exposure (see text for details).

established for every individual image to make sure the data is not affected while still picking most of the cosmic ray events. As expected this procedure proved more effective with the observations done in clouds free conditions. Nevertheless we successfully applied it also to the observations from the first observing night with varying cloud coverage (see Fig. 2.4) The so produced map of cosmic ray events was grown by 1.5 pixels and fed into the IRAF task *fixpix* to substitute the masked pixels with interpolation across the smallest dimension. To fully remove

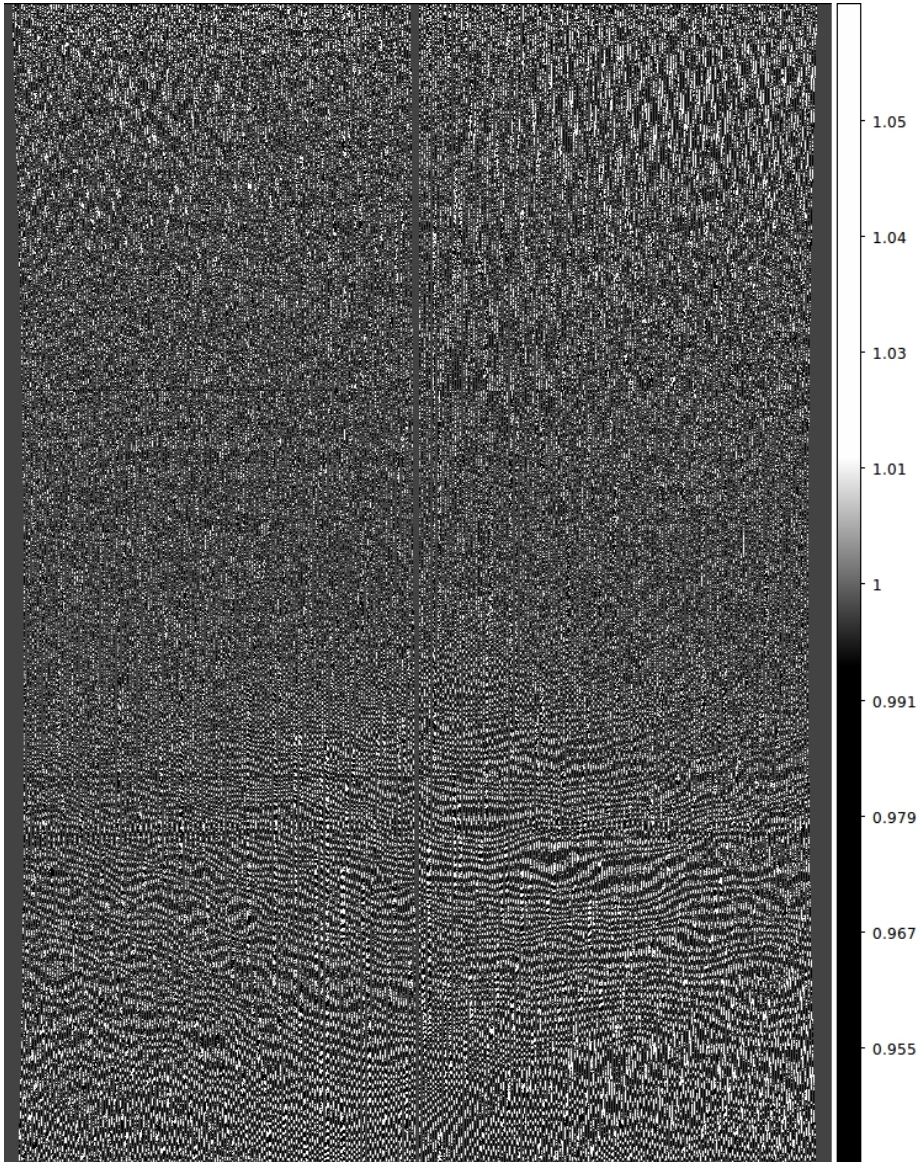


Figure 2.7: A map of the relative pixel-to-pixel sensitivity variations and the fringe pattern. The red end is at the bottom.

the effects from the cosmic rays and the artifacts introduced by our cleaning algorithm we used a median combination with median scaling to produce the final images.

Fibre throughput and geometrical correction

Prior to the throughput correction a 2-D model of the scattered light was made and fitted to the master twilight flat field image with the IRAF task *apscatter*. The scattered light model was fitted to the first and last ~ 400 unexposed pixels, and to the central gap of ~ 10 pixels. This step was also done with the target data, where a peak level of ~ 3 ADU was found.

The correction for the different throughput of the individual fibres is achieved in two steps. First wavelength dependent throughput correction is calculated from the sky flat field images. The 1-D twilight sky spectra extracted with *apall* were wavelength calibrated using observations of a comparison HeNeAr lamp. Following the Hectospec pipeline approach, the spectra from apertures between 141 and 146 was averaged and then divided into all 300 twilight spectra. The so produced ratio was fitted with a low order function to produce a map of the wavelength dependent part of the relative fibre throughput shown on Fig. 2.8a. The second step of the relative throughput correction was based on the flux measured in a number of sky emission lines. We used 7 of the strongest lines which can reliably be measured. A relative scales were calculated for each fibre, based on the median of the line flux ratios excluding the two extreme ones. Unlike the first part of the throughput correction this one does not have colour dependence. The image with the relative scales can be seen in Fig. 2.8b.

The area on the sky accepted by the individual fibres changes with the distance of the fibre from the center of the focal plane. The variation is between $1.76''^2$ in the center and $1.62''^2$ at the edge of the usable focal plane. All the fibres were brought to the same sky coverage of $1.62''^2$ with the correction calculated as:

$$I(\lambda)_{corr} = \frac{I(\lambda)_0}{(1.11748 + (0.0001866 \times rad) - (0.00000188622 \times rad^2))} \quad (2.1)$$

where *rad* is the distance from the fibre to the center of the focal plane.

This correction was only applied to the target data as all the calibration frames were taken with the fibres parked at constant field angle.

Wavelength calibration

A comparison HeNeAr lamp spectra was observed in the beginning of each night. An atlas of the HeNeAr spectral lines was taken from Megan Kiminki's webpage (<http://spockprime.as.arizona.edu/~megan/hectospec/>). The accuracy of our wavelength calibration in terms of RMS scatter around the fit of the wavelength solution are $\sim 0.06 \text{ \AA}$ and never higher than 0.09 \AA which is very similar to the typical scatter for the instrument 0.06 \AA and consistent with the error in determining individual lines centres (Fabricant et al. 2005, 2008) (Fig. 2.9). The final spectra extends from 3699.5 \AA to 8905.5 \AA with a pixel scale of 1.212 \AA . In addition the wavelength zero point was adjusted for each individual target exposure,

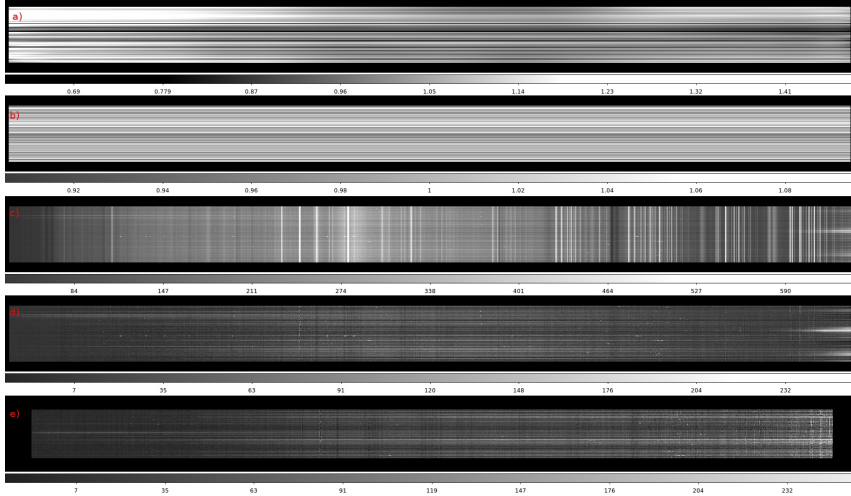


Figure 2.8: The extracted spectra from the first observing night. From top to bottom- a) A wavelength dependent throughput correction derived from twilight sky exposure; b) Throughput correction based on sky emission flux; c) Target plus sky spectra; d) Target spectra after sky subtraction, and e) The final spectra of the 262 targets after red leak and system throughput corrections, and trimmed to the final wavelength coverage. Each horizontal line represents one fibre. The red is to the right.

based on the position of 3 sky emission lines measured with *emsao*. Those offsets were rarely exceeding 0.1 pixels and with a median offset of 0.05 pixels at most, which is $< 5 \text{ km s}^{-1}$ at the wavelength of the redshifted $H\alpha$ line. The offsets were very similar among the observations from the second night but somewhat more variable during the first night. All were very similar among the different apertures.

An additional check on the wavelength calibration is presented on the first column of Fig. 2.10, where the central wavelengths of five bright unblended sky lines measured from our spectra are compared with the expected λ_0 for all the apertures from both nights.

Sky subtraction

Prior to the sky subtraction an additional flux scaling between the fibres was applied. This was based on the flux measured in seven of the brightest non blended sky emission lines. This is the final scaling applied to the individual fibres. The sky spectrum subtracted from each fibre was not additionally scaled as this scaling would be biased because of the presence of a signal from the targeted galaxies.

To select sky spectra not affected by other sources we made one average sky spectra from all the sky fibres and then examined the difference between every sky fibre and that average. Those with large deviations were rejected, leaving 24 and 20 *clean* sky fibres for the two observing nights, respectively.

Because the sky subtraction is considered problematic when dealing with data

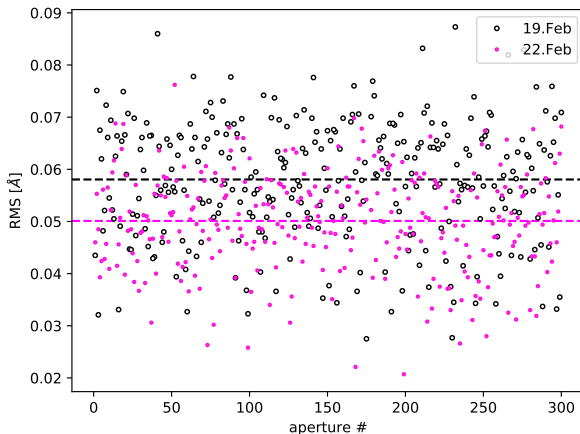


Figure 2.9: The RMS of the wavelength solution fit for every individual fibre from the two observing nights. The dashed lines show the median.

from multi-fibre spectrographs, particularly at low resolution, a number of different ways of subtracting the sky have been suggested in the literature alongside the straightforward averaging of all the clean sky spectra: making one sky spectra per CCD (Mink et al. 2007), making one sky per fibre averaging the nearest 6 sky fibres (Fabricant et al. 2005), eigenvector sky subtraction (Kurtz & Mink 2000), to name the few proposed for MMT data. We tested three different ways of subtracting the sky from our data, the ones adopted by (Fabricant et al. 2005) and (Mink et al. 2007), as well as *all fibres* method where all the clean sky fibres are used to make one average sky spectra and this is then subtracted from all the data fibres.

Fig. 2.10 shows the measurements of the FWHM of five bright sky lines (the first line at 4358.50 \AA is due to mercury discharge and comes from street lamps. This does not affect our conclusions (Omer & Lawson 1936).). The Figure does show a variation of the psf across all the fibres at the red end of the spectra. Those variations were smooth with an amplitude of $\sim 10\%$ and only affect the wavelengths redward of 8000 \AA . Because of the smooth variations of the psf making two separate sky spectra, one for each CCD (like in Mink et al. 2007), did not improve the sky subtraction. One can see on Fig. 2.10 that the variation of the line’s FWHM has the same amplitude over the first 150 fibres (imaged on CCD 1) and over the set of fibres imaged on CCD 2 (151–300). Because of that we rejected the use of this method.

We performed the sky subtraction with a sky made by averaging all the clean sky fibres and by averaging the six nearest clean sky fibres. A comparison between the noise patterns in the final spectra revealed an improvement in the sky emission dominated red end of the spectra when averaging the nearest six sky fibres. Even though throughout the rest of the spectra the noise was slightly elevated as a result of averaging fewer spectra we decided to stick to the second approach following the recipe of (Fabricant et al. 2005).

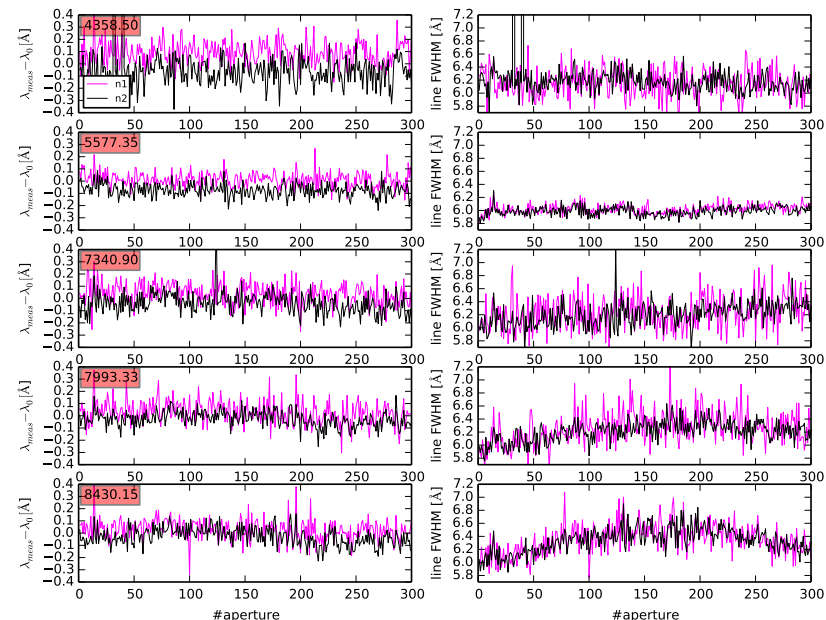


Figure 2.10: The first two moments of five bright, unblended sky lines with the central wavelengths printed in the upper left corner. Every row shows one line. The first column shows the variations of the central wavelength of the line around its laboratory wavelength across all the fibres. The second column shows the full width at half of the maximum for the given line. The observations of the first (second) night are shown in magenta (black). The line at 5577.35 Å has the highest signal to noise hence the small scatter. The aperture numbers from 1 to 150 are imaged onto CCD 1 and the rest onto CCD 2.

The Hectospec pipeline provides a model of the sky absorption features around 6870 Å and 7600 Å, this was divided into all the sky subtracted spectra, after which they were split into separate 1-D spectra.

Many of the Hectospec fibres are affected by a light leakage from a fibre positioning LED. This is spread redward of 8500 Å, affecting some ~ 500 pixels. In the fashion of the Hectospec pipeline, the continuum redward of 8500 Å was fitted with the IRAF task *fit1d*. This fit was subtracted only from the spectra that shows a rising continuum in that region.

The final step in the data processing was to correct all the data for a wavelength dependent system throughput. This correction was based on the measurements published by Fabricant et al. (2005) (their Fig. 16). This curve is based on the regular observations of standard stars which have demonstrated the remarkable stability of the Hectospec instrument (Fabricant et al. 2005). The extent of this curve gives the final wavelength extend of our spectra.

Spectrophometric calibration

This step was performed with further analysis in sight and did not play a role in the analysis presented in the following chapters.

We adopt the procedure for flux calibration from Fabricant et al. (2008). This method compares the R-band aperture magnitude from imaging with the integrated spectral flux through the filter transmission curve. Because Hectospec is very stable over long period of times and because it has an atmospheric dispersion compensation (ADC) prisms this method works remarkably well (Fabricant et al. 2008). We used the total magnitudes as extracted from the CFHT g' and r' images for the calibration, and calculated individual zero point for each individual galaxy. This way we also apply aperture correction.

In order to extract magnitudes from the spectra, we multiply each spectra with the transmission curves of the two filters and sum the result. We then convert that to AB magnitudes indicated on Fig. 2.11 as r_{spec} and g_{spec} , respectively. Fig. 2.11 shows the zero point for each galaxy together with a fit demonstrating the variation between the two filters and nights. The fit was performed with iterative rejection of the outliers. The points used for the final fit are indicated with black circles. The intercept and the slope of each fit are indicated in each panel. The fits to the red filter are repeated with dashed line in the g' plots. Those fits are plotted just for indication of the stability of this calibration. We calculated individual zero points for each galaxy. We did a visual inspection of each individual (spectra \times filter transmission) for the outliers without finding any obvious reason for their deviation. We conclude that it must be due to the different surface brightness distribution of each galaxy. The g' band shows larger scatter than the r' due to its lower signal to noise ratio. This calibration was only done to the 353 galaxies which have enough signal in the g' band for it to be reliably measured. The final uncertainties of this calibration are ~ 0.25 mag, indicated by the rms of the fit to the r' band magnitudes shown on Fig. 2.11. This is broadly consistent with the findings of Fabricant et al. (2008).

2.1.3 Redshift determination

As a first and most robust estimation of the redshift of the target galaxies a manual fitting of a Gaussian to emission or absorption lines was done in IRAF. Those were usually [O II] 3727 Å, H α 6563 Å, H β 4861.33 Å, [O III] 5006.84 Å and [O III] 4958.91 Å in emission and the calcium K and H lines in absorption at 3934 Å and 3968 Å together with Na 5892.50 Å. This yielded 170 redshifts, based on at least two lines. A manual quality flag was assigned to each redshift depending on the number, nature and strength of the lines used. Those redshifts are designated z_e from now on.

A second estimation of the redshift was done with cross-correlation of the observed spectra with spectral templates from SDSS DR7. Those redshifts are designated z_{cc} from now on. IRAF provides at least two routines that can perform this task as prescribed by Tonry & Davis (1979) - *noao.rv.fxcor* and *rvsao.xcsao*, we used both of them since they did not return identical results. Both tasks apply

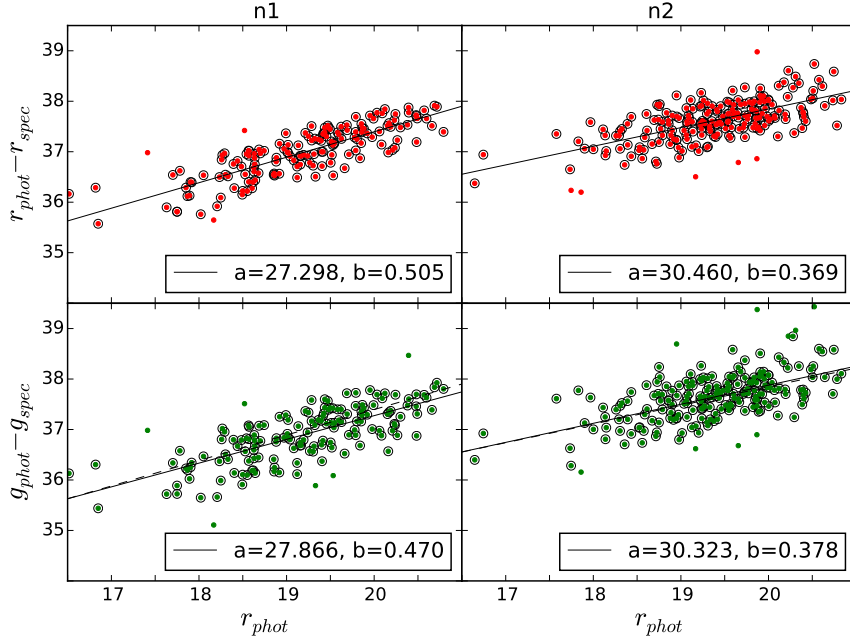


Figure 2.11: The photometric zero point for the two nights and two filters. The colour symbols show all the galaxies, while the black circles show the galaxies used for the fit. The fits to the red filter is repeated with dashed line in the g' plots. The intercept and the slope of the fits are indicated in each panel.

a Fourier filter to the continuum subtracted spectra prior to the correlation in order to remove the low frequency residuals from the continuum subtraction. Setting it up we followed a prescriptions from Alpaslan (2009) and Tonry & Davis (1979), and run a series of tests to select the filter setup that gives the highest Tonry and Davis r value and a stable redshift estimate while reducing the effects of Gibbs ringing. Only the region between 3800 and 8000 Å was correlated, thus avoiding the wavelengths most affected by the bright sky emission lines, at the expense of missing the $H\alpha$ line from galaxies at the high redshift extreme of the cluster ($v_{cut-off} > v_{cluster} + 5000 \text{ km s}^{-1}$) and the background sources.

Six different galaxy spectra were used as templates varying from early to late type, including a luminous red galaxy. From the twelve cross-correlation iterations (six with *fxcor* and six with *xcsao*) the one with the highest Tonry and Davis r value was selected. Few additional tweaks to the final cross-correlation redshifts were done. The SDSS template spDR2-026 of a late type galaxy was found to systematically return erroneous redshifts at $z \geq 0.2468$, when applied with *xcsao*. In those cases the *fxcor* redshift was taken irrespective of the r value. A small number of galaxies return a velocity of 0 km s^{-1} , those were discarded.

In order to estimate the quality of our cross-correlation redshifts, and determine a cut-off value in r , we applied a test similar to the one used by Kurtz & Mink (1998) and shown on Fig. 2.12. We plot the absolute difference between the velocities ($c \times z$) estimated by fitting of emission/absorption lines (z_e) and the

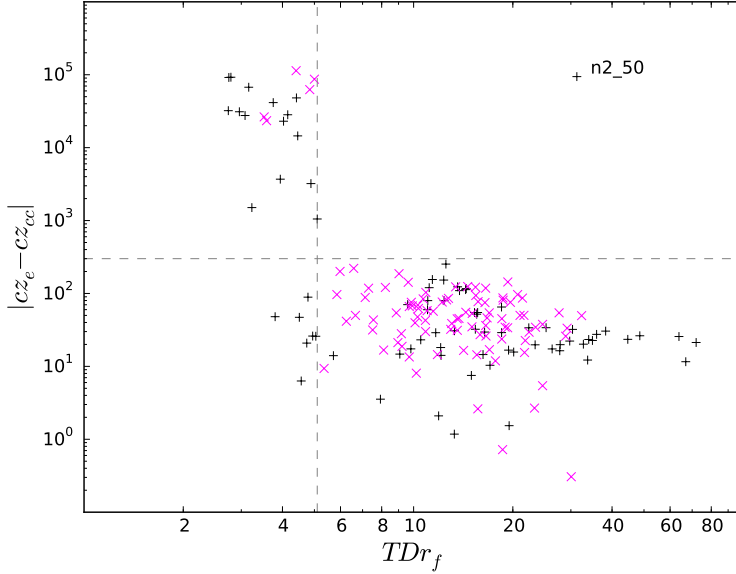


Figure 2.12: Modulus of the velocity difference between the line (cz_e) and the cross-correlation (cz_{cc}) redshifts against the highest r value. The horizontal dashed line is at velocity difference of 300 km s^{-1} , the vertical dashed line is at the cut-off value of $r = 5.1$. The + symbols show z_{cc} estimated with the IRAF task *FXCOR*, the \times ones with *xcsao*. *n2_50* is discussed in the text.

velocities from the cross-correlation method (z_{cc}) against the r value of the best z_{cc} measurement. The horizontal dashed line on Fig. 2.12 is at 300 km s^{-1} - the expected combined uncertainties of the two redshift estimates. The vertical dashed line is at the cut-off value in r . The top right part of the plot should contain no sources. The one source at high r and large difference between the two z estimates - *n2_50*, is a galaxy with strong emission lines. Since we manually checked all the available spectra, and a z_e redshift measurements of all the sources with strong emission lines would be available, this type of sources pose no confusion in our final redshift estimates (z_f). Based on this plot we set a cut-off level of $r > 5.1$ for reliable z estimates from cross-correlation (z_{cc}). This conservative choice should guarantee the disposal of all the dubious z_{cc} estimations and is indicated by the vertical dashed line in Fig. 2.12. From Fig. 2.12 we estimate that lowering the cut-off r value to 4 will add approximately two blunders for every three accurate z estimations.

Following this step we went once again manually through every single spectra to check the compliance between z_e and z_{cc} , and to search for faint emission/absorption lines confirming the z_{cc} . We found visual confirmation for 190 of the z_{cc} estimations to add to the 170 galaxies for which we manually measured z and then confirmed it with z_{cc} (those are the points residing in the bottom right part of Fig. 2.12).

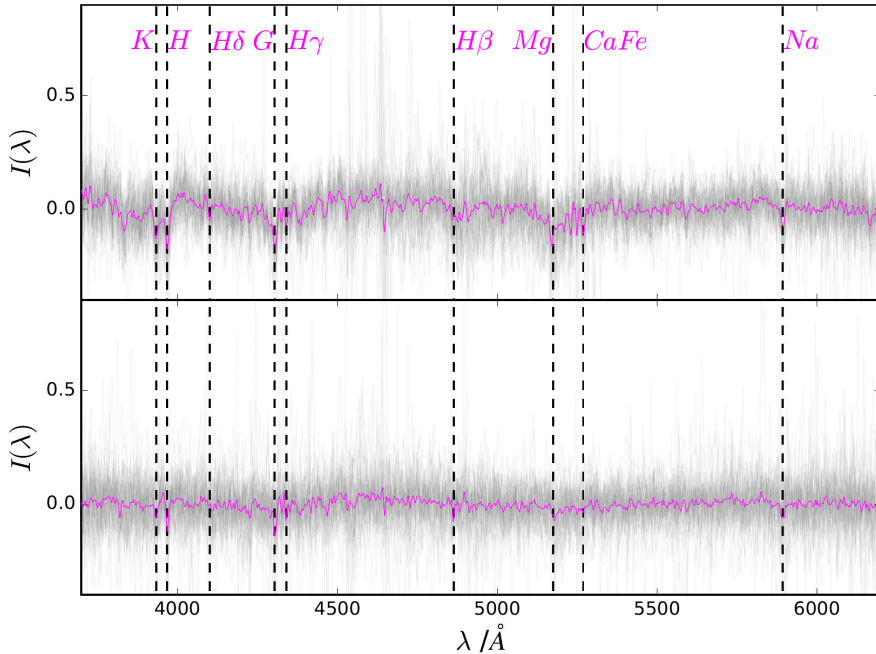


Figure 2.13: (*Top*) All the spectra with z_r measurements (49 in total, gray lines) and their average (magenta line). The positions of the strongest absorption lines are marked. (*Bottom*) The same number of spectra, randomly drawn and averaged from the spectra with uncertain z estimate.

We add to the final catalogue also all the targets for which at least one cross-correlation task returned a z estimation with $r > 5.1$ even if we couldn't visually find any spectral features to confirm it. There are 49 such targets and their redshift estimation is designated z_r from now on. For 32 of those both z_{cc} estimations agree.

Although both *fxcor* and *xcsao* stick to the robust Tonry & Davis (1979) recipe they are designed with different goals in mind, and probably that's why their results differ. What Fig. 2.12 shows is that *fxcor* usually gives a higher r value than *xcsao* although the bulk of the erroneous estimations, residing in the top left corner of the figure, also come from *fxcor*. The visual inspection of all the spectra confirmed that *fxcor* is more often wrong, particularly with the low signal to noise spectra.

To further test the accuracy of the z_r measurements we stack all those spectra. The results are shown on Fig. 2.13. The individual spectra of all the 49 galaxies are plotted with thin gray lines. The stacked spectra is overplotted with red line. The positions of the, usually, most prominent absorption lines are annotated with arrows. A number of absorption lines are visible in the stacked spectra with greatly increased signal to noise ratio, like the H and K lines. From the hydrogen lines only the $H\delta$ is prominent.

Even though some of the measurements which we consider unreliable are actually accurate (\times on Fig. 2.14, and the lower left part on Fig. 2.12) we exclude those from the following analysis.

With this approach we are confident in the correct estimation of the redshifts for 409 (78%) of our target galaxies. Those are distributed as follows: 170 (42%) z_e , 190 (46%) z_{cc} and 49 (12%) z_r . 17 of the 114 targets which failed to give reliable z estimate (referred to as "uncertain z " from here on), had their spectra spoiled by the presence of a nearby bright star. While selecting the targets we did not anticipate that a scattered light from a very bright star can affect a spectral measurement more than 7' away. In hindsight, starting directly with z_{cc} would be more efficient way of building the final redshift catalogue.

The so measured redshifts were corrected for the orbital motion of Earth by -27.94 km s^{-1} for the first night, and -28.00 km s^{-1} for the second.

2.1.4 Uncertainties

The final catalogue contains the z_{cc} estimation of the redshift and its associated uncertainties for the 190 / 49 galaxies with / without visually confirmed cross-correlation z . Both cross-correlation tasks provide estimation of the uncertainties. In the case of *fxcor* it is based on the strength of the correlation peak and the goodness of the fit to it. The *xcsao* task follows the Tonry & Davis (1979) approach and calculates the errors with:

$$error = \frac{3}{8} \frac{w}{(1+r)} \quad (2.2)$$

where w is the width of the correlation peak and r is as defined by Tonry & Davis (1979). The interested reader can find an exhaustive discussion on the errors estimated by *xcsao* in Kurtz & Mink (1998).

The final estimation z_f for the 170 galaxies for which we also have z_e is based on a weighted mean of the z_e and z_{cc} , with the weights on z_e based on the discrepancy between the z shown by the different lines. We will continue to refer to those redshifts with z_e .

The median error of all the sources with secure z_f is 78 km s^{-1} . Fig. 2.14 shows a comparison between our measured redshifts and the ones published by Girardi et al. (2008). The median error on cz in their combined catalogue is 112 km s^{-1} . The standard deviation from the line of equality on Fig. 2.14 - 195 km s^{-1} shows that we are underestimating the uncertainties of our measurements by $\sim 30\%$. This is broadly consistent with the findings of Kurtz & Mink (1998) for the error estimations made with *xcsao*. We multiply our errors in the final catalogue to compensate for that.

Few things are apparent on Fig. 2.14. Both the cross-correlation method and the line fitting method have comparable spread around the zero difference line (green and black \bullet , respectively). Also, as apparent from Fig. 2.12, some of the "unreliable" redshift estimates (\times) are actually accurate to within the errors of the measurement.

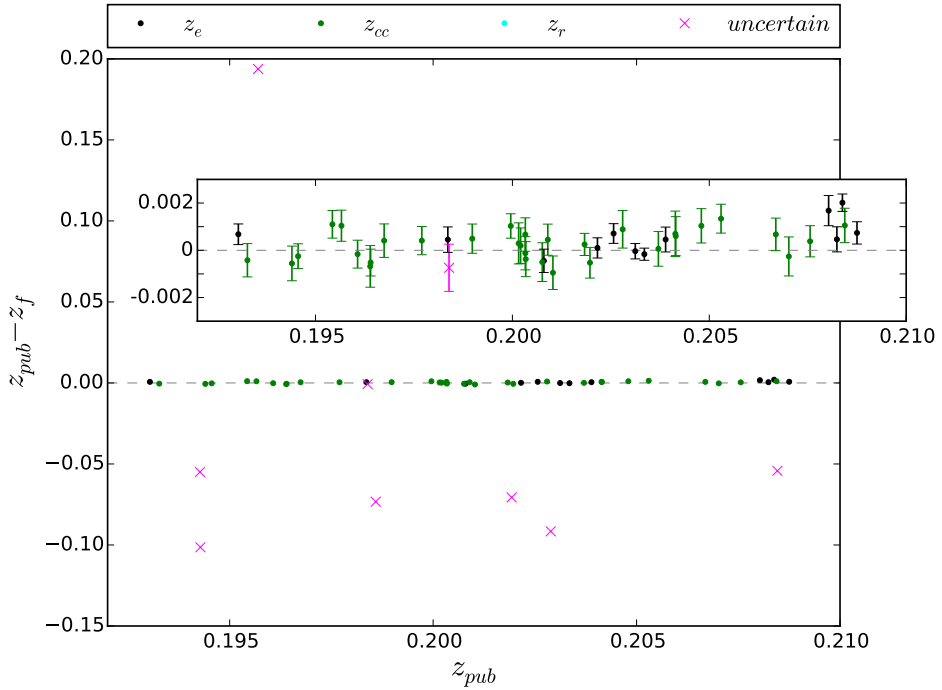


Figure 2.14: Comparison of our redshift estimations (z_f) with the published ones from Girardi et al. (2008) (z_{pub}) for the 52 common targets. The \bullet of different colours represent our secure estimations, the \times are the uncertain ones. The inset is a zoom around the line of equality. All the points on the big plot are visible. See the text for explanation of the separate z_f estimations. The figure is a re-print from Paper I.

From the 52 targets in common with G08 we have enough signal in our MMT data to confirm their z estimation with high certainty for 44 of them. For three of the other 8 targets we have a z_{cc} estimation in agreement with the G08's value but with r value below our cut-off limit. We could not estimate the redshift for the remaining 5 targets.

2.2 21 cm imaging of galaxies in A963 and A2192

2.2.1 Observing strategy

THE 21 cm data presented in this thesis were collected with the Westerbork Synthesis Radio Telescope (WSRT)¹. In total 190 12 hour measurements were performed, out of those 118 in the field of A963 and 72 in the field of A2192 (tbl.2.1). The coordinates of the two telescope pointings are RA 10h17m14.22s, Dec +39d01m22.1s (A963) and RA 16h33m22.98s, Dec +42d40m11.1s (A2192). Note that the measurements of A963 are actually centered on “4C +39.29“, a ~ 1.4 Jy at 1.4 GHz source situated 9.2' east from the cluster center, marked by the position of the cD galaxy. This pointing was selected in order to optimize the calibration process in the presence of such a strong continuum emitter in the field. For external phase and amplitude calibration two standard sources were observed, one in the beginning and one at the end of each measurement, with an integration time of 30 minutes. In the field of A963 the primary calibrator was 3C147 and the secondary CTD93. For A2192 the primary calibrator was 3C286 and the secondary 3C48. Due to the overwhelmingly large amount of data, and to avoid time loss the data were collected without change in the present antennae configuration.

Table 2.1: The distribution of the 12h measurements executed at WSRT over the years.

object	year	number of measurements
A963	2005	23
	2006	34
	2007	31
	2008	30
A2192	2005	15
	2006	20
	2007	14
	2008	23

The correlator, being easier to tune up, had the same setup for all the observations. Integration time of 60sec, eight partially overlapping IF bands, each 10MHz wide, with 256 channels and two polarizations per channel. The total bandwidth of 60MHz covers the range between 1220 and 1160 MHz, split in 1600 unique channels, 0.039 MHz each. This bandwidth corresponds to redshift range of $0.164 < z < 0.224$. The channel width gives us a velocity resolution of ~ 10 km s⁻¹. No on-line hanning smoothing was applied. At the central frequency of 1190MHz the full width at quarter of the maximum (FWQM) of the

¹The WSRT is operated by the Netherlands Foundation for Research in Astronomy(NFRA/ASTRON), with financial support by the Netherlands Organisation of Scientific research (NWO)

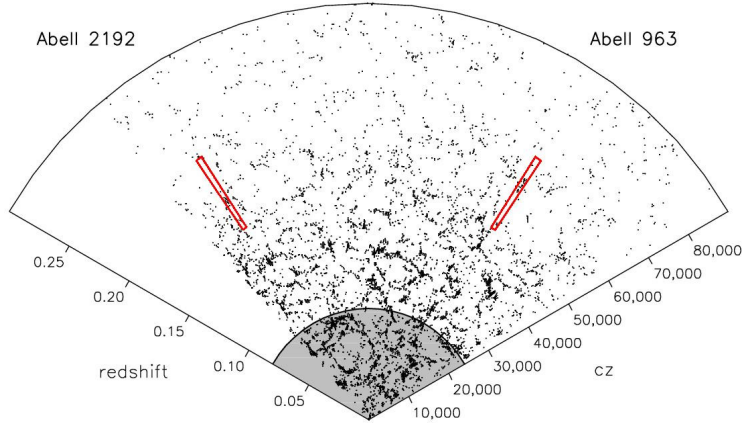


Figure 2.15: A pie diagram, showing all SDSS galaxies, along a great circle connecting the two clusters. The red rectangles show the volumes surveyed with WSRT. The figure is a reprint from Paper III.

primary beam of WSRT becomes $\sim 1^\circ$. The synthesized beam of WSRT at the same frequency and for the average declination of our targets ($+40^\circ$) has a size of $23'' \times 39''$ when imaged with robust parameter of 1 (Briggs 1995)(see section 2.1.2). The physical dimensions of the surveyed volumes, out to FWQM of the WSRT's primary beam, are two truncated cones, with diameter of the bases 10.04 and 12.86 Mpc, and a height of 326 Mpc positioned between 780 and 1106 Mpc (Fig. 2.15). The total surveyed volume with the two pointings, with identical setup is $67,130 \text{ Mpc}^3$. And the spatial resolution, defined by the size of the synthesized beam is $75 \times 127 \text{ kpc}$.

Fig. 2.15 shows a pie diagram containing all the galaxies with spectroscopy from SDSS (York et al. 2000) and the relative volumes probed by the here described WSRT survey. The gray region at the bottom of the plot shows the completeness limit of the ALFALFA survey (Giovanelli et al. 2005).

2.2.2 Data processing

The data processing was done in NRAO's² Astronomical Image Processing System (AIPS) and Groningen Image Processing SYstem (GIPSY, van der Hulst et al. 1992)).

After reading all the measurements into AIPS and concatenating them into multi-source files, the first part of the flagging of bad data was done based on manual inspection of system temperature plots. The data for the calibrators was clipped (AIPS task *CLIP*) to remove parts affected by the strongest radio frequency interference (RFI) peaks. After that a preliminary bandpass correction (BP) was determined, that could still be affected by RFI. The clipping then was

²The National Radio Astronomy Observatory is a facility of the National Science Foundation operated under cooperative agreement by Associated Universities, Inc.

repeated, applying the preliminary BP correction, and additional flagging was done (*FLGIT*) by fitting a baseline of order one to the channels between 26 and 217, and flagging everything above 8σ . The final bandpass correction was determined after applying those flags. This calibration table was then copied to the full data set.

RFI flagging

The central 75% of the band were then averaged (*AVSPC*) for every calibrator source, and the flux density was set with the task *SETJY*. The flux density of CDT93 was calculated with *GETJY* from the data of 3C147. The flux for 3C286 was set by taking into account the $\sim 10\%$ linear polarisation of the source, following the WSRT data analysis cookbook on www.astron.nl. The phase and gain solutions based on the calibrators were then interpolated into a CL table, which was then copied to the full data set. The bandpass and external calibration were then applied while splitting the data set into individual bands for further precessing. An iterative procedure for RFI flagging was developed, using velocity smoothing and clipping. First a first order baseline was fitted to the channels from 26 to 217 and subtracted (*UVLIN*). Then a series of iterations, with a boxcar smoothing and clipping were applied. The boxcar was with 4, 8, 16, 32, and 64 channels width, and the clip level was adjusted to 4.5σ of the smoothed data cube. The flags after every iteration were collected in a flag table and then applied to the original data set. Example of the work of the RFI flagging procedure is shown on Fig. 2.16.

Self-calibration

Once the data was assumed to be clean of RFI and system introduced noises a sky model was made, to be used for self-calibration of the line data cubes. This was done by averaging the central channels, from 26 to 217, for ~ 40 measurements per IF and per object and adding them together (*DBCON*). After that those continuum images were self-calibrated, iteratively shortening the solution intervals and going from phase only to both amplitude and phase solutions. The iterations involved the tasks *IMAGR*, *CALIB* and *CLCAL*. After running a number of tests, the solution intervals that gave the best results were - for the phase only self-calibration - 10, 5, 5, 2, 2, 1 minutes, and for amplitude and phase calibration - 15, 10, 5 minutes. Performing amplitude calibration was found necessary only in the field of A963, which was more complicated due to the fact that the two strongest continuum sources in the field were lying on each other's side lobes. For the field of A2192 phase only self-calibrations was found sufficient, after visual inspection of the results from the self-calibration (see Fig. 2.17 and 2.18). 16 sky models were produced that way, one for each band and for each object. The self-calibration solutions for every individual measurement were based on the clean components of those sky models. Two of those sky models are shown in figures 2.19 and 2.20.

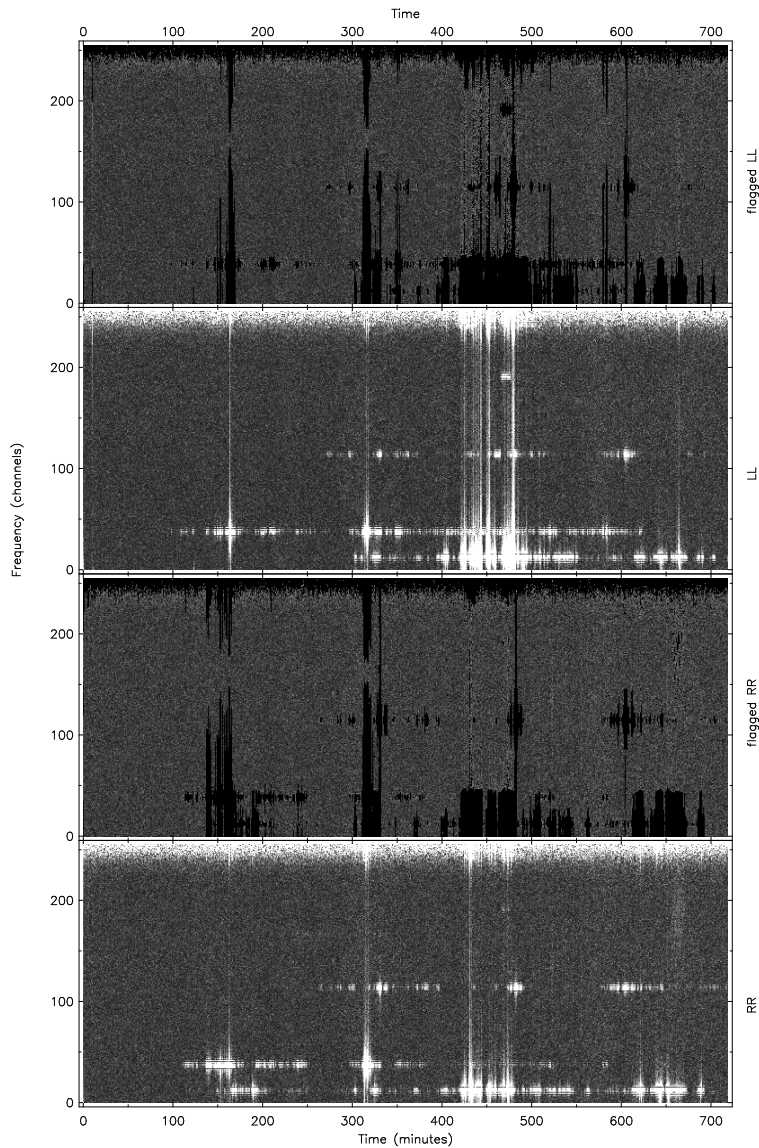


Figure 2.16: Example of the work of our RFI removal algorithm. On the picture, the two polarisations of a baseline, taken from a random measurement is shown before and after the RFI flagging has been applied, as described in the text. The frequency range shown here span the full 256 channels. Only the central $\sim 75\%$ of that are actually used in the imaging. The full measurement time range of 12 hours is shown.

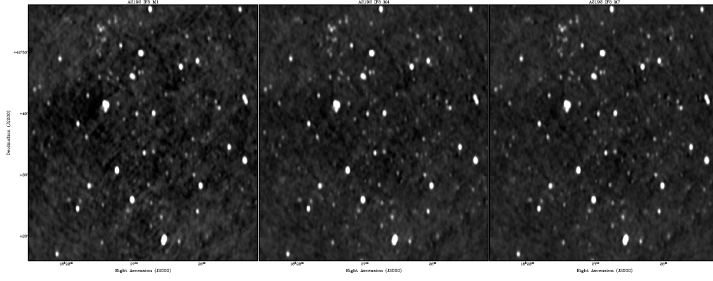


Figure 2.17: Example of the results of the self-calibration process. A zoom in on the central parts of the continuum image of A2192 in IF5 is shown. On the left before self-calibration, in the middle is an intermediate step during the process, and on the right the final image.

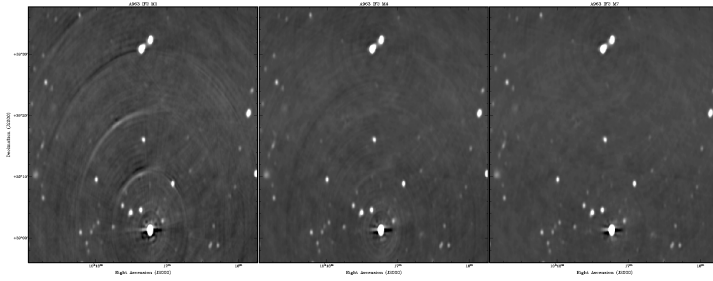


Figure 2.18: Same as Fig. 2.17 but for IF2 of A963.

Continuum subtraction

In order to remove the continuum emission, which is at a much higher level than the expected H I signal, after applying the selfcal solutions, the clean components of the sky models were subtracted from the line cubes (*UVSUB*). Followed by a subtraction of a first order baseline fitted to the real and imaginary components in frequency direction for each visibility (*UVLIN*). The fit was done over all of the middle 75% of the channels, since the expected level of the H I line emission is too low on a single spatial baseline, to have any significant influence on the spectral fit. As explained later additional step was necessary in order to remove the effects of the presence of the weak H I emission during the *UVLIN* run.

The central 202 channels from every band for every measurement were then Fourier transformed (*IMAGR*) with $8''$ per pixel, and 512×512 pixels. Hence the final images have a side of $\sim 68'$. A robust parameter of 1 was used in the imaging, as a good compromise between resolution and sensitivity (Fig. 2.21). This gave us a synthesised beam with FWHM of $23'' \times 39''$, which corresponds to 75×127 kpc of spatial resolution at the distance of our targets. A weighted average of those data cubes was then made in the image domain, in *GIPSY*, with the weights based on the rms noise of every cube, channel by channel.

One of the obstacles encountered in the process of data reduction was the so

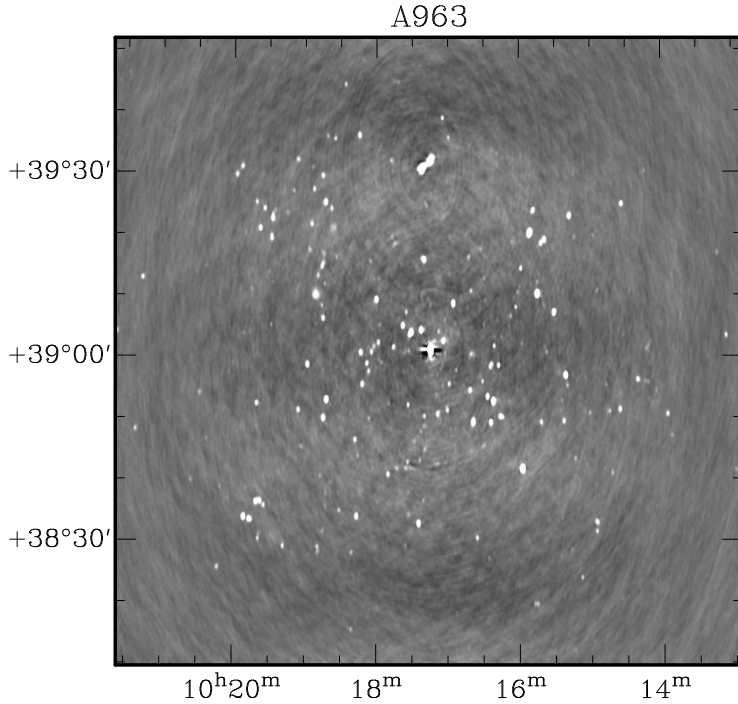


Figure 2.19: A radio continuum image of A963 used as one of the sky models for self-calibration of IF1. The model is made by averaging the central channels of ~ 40 individual measurements. Amplitude and phase self calibration has been done, as explained in the text.

called ghost, shown in Fig. 2.22. This artifact is possibly caused by a cross-talk between the feeds of some antennae prior to the cross correlation. This image appeared on all the measurements from 2008, at all baselines with 8×144 m length, drifting in declination with frequency. The strongest one was from baselines RT1 – RTA and was noticeable in a single measurement, while the contribution from the other baselines was visible only in the combined cube. Those baselines were flagged in all the measurements from 2008, and the FFT repeated. One additional step was found necessary for the A2192 data. A quasar at $z = 0.6$ with a very strong continuum emission cataloged as "3C345" and situated a little over three degrees away from the WSRT phase centre had its side lobes drifting through the data cube at level exceeding the rms noise level in the combined data cube. Those were fitted and subtracted from the combined data cube with care being taken not to affect the H I signal present in the cube and to correctly follow the side-lobes as they change position in both R.A. and Dec with frequency (Fig. 2.23).

After *UVLIN* and *UVSUB* there were still residuals from the brightest continuum sources in the two data cubes, largely due to variations of the bandpass with position. In addition the H I signal was still surrounded by a negative baseline, due to the presence of that very weak signal in every measurement, that affected

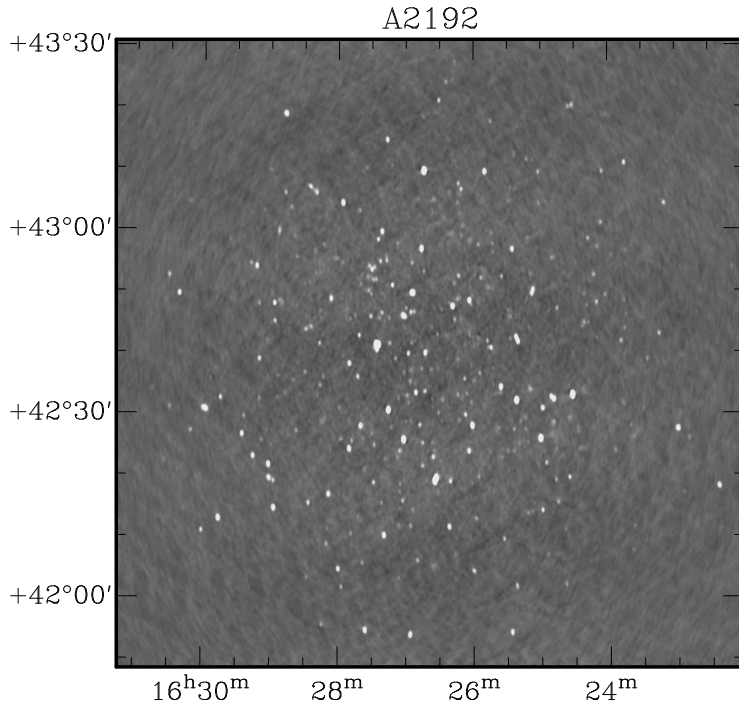


Figure 2.20: A radio continuum image of A2192 used as one of the sky models for self-calibrate IF1 of A2192. The model is produced as the one in 2.19, but only with phase calibration.

the baseline fitting with *UVLIN*. The remnants of the bright sources were cleaned and then blotted out of the data cubes.

The imperfections of the single first order run of *UVLIN* were cured in two steps and the results are briefed in Fig. 2.24. The first step was a series of iterations of clipping the H I signal and fitting and subtracting the continuum with the GIPSY task *conrem*. The continuum was fitted with first and second order polynomials, but the second order was always producing better results, probably due to the drifting with frequency side-lobes of the H I sources, before cleaning their signal. The results from this procedure are shown in the middle panel of Fig. 2.24. After that the source detection algorithm was run, and a mask containing the H I signal was made and used to flag it, in the initial cube, before the iterative continuum flagging. The produced in such a way data cube, containing only the imperfections from *UVLIN* but not the H I nor the continuum signal, was used for a linear fit, which was then subtracted from the H I data cube. The final view of the baseline around a H I source is shown in the right-hand panel of Fig. 2.24. Noticeable is the absence of the negative signal around the source (the frequency runs vertically) which is otherwise visible on the left and middle panels.

Following that, the H I signal was cleaned and restored in GIPSY. The combined beam pattern was produced using the same weights calculated for the com-

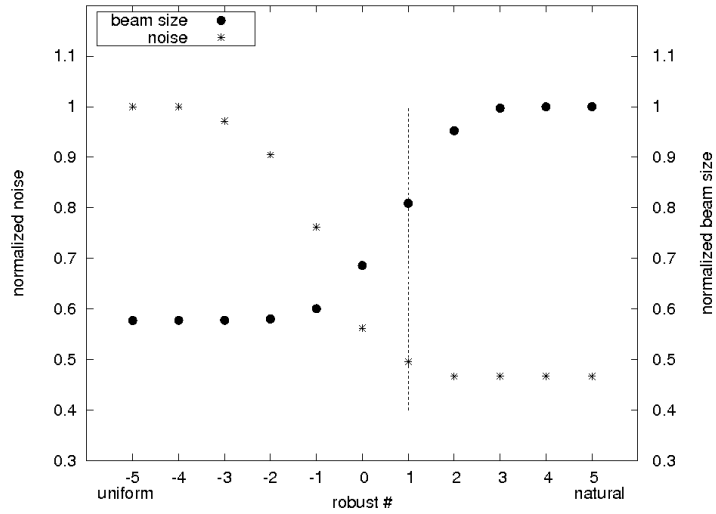


Figure 2.21: The distribution of the noise of the final data cube and beam size, relative to the weighting of the visibilities used in the imaging. Both the noise and the beam size are normalized to their peak values. See the text for details on the beam size and the noise in the final data cubes. Robust one was adopted in this thesis, marked here by the dashed line, as the best compromise between noise and resolution.

Frequency: 1201.276 MHz

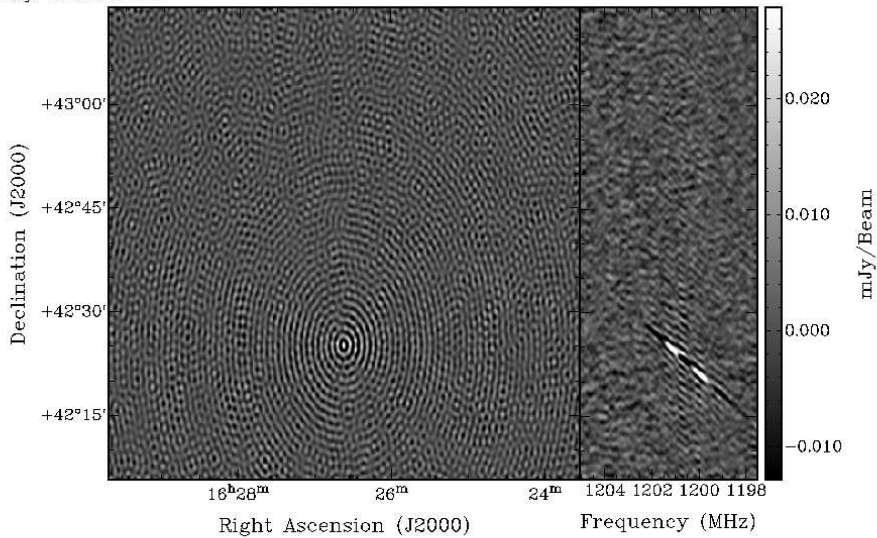


Figure 2.22: Image of the ghost (see text for details). The left side of the figure shows the image on the sky. The right side shows declination - frequency image at constant right ascension.

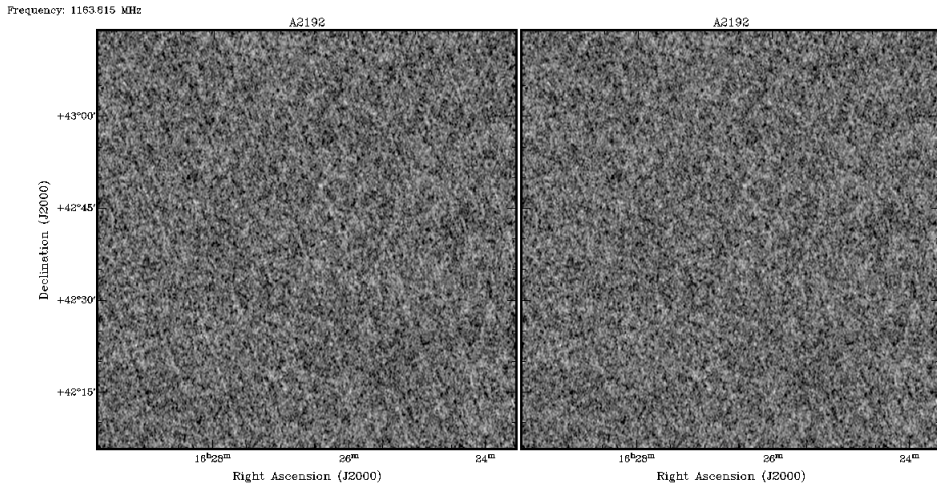


Figure 2.23: One channel from the A2192 data cube. On the left side showing the side lobes of "3C345" running diagonally through the image. On the right side the same channel after removing the side-lobes.

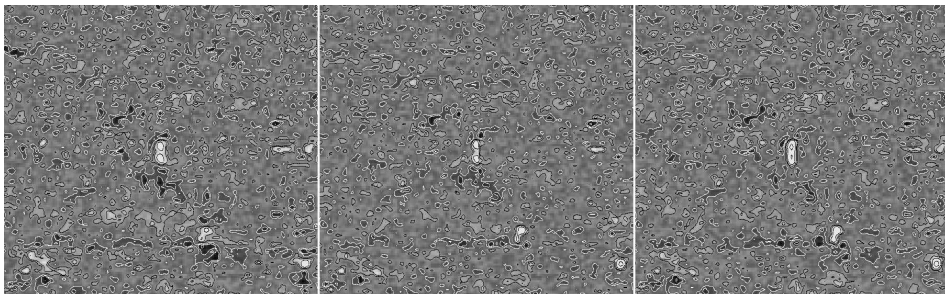


Figure 2.24: Example of a bandpass side-lobes after *UVLIN* (left), after the iterative *conrem* (middle), and in the final data cube (right). The contours are at 1, 2, 4 and 8σ . The negative contours are plotted in white. Frequency runs vertically and right ascension horizontally.

bination of the data cubes. The cleaning of the H I signal was repeated as the mask containing all the signal was continuously improved with a series of source finding runs at different resolutions (see section 2.2.4).

2.2.3 Quality of the data

Fig. 2.25 shows the rms noise in the two data cubes, after smoothing to a velocity resolution of 44 km s^{-1} . Visible is the increase of the noise at the high frequency end of the survey, due to the amount of data polluted by RFI (see Fig. 2.28). The regularly appearing peaks in the noise are often associated with the edge channels of every IF band, although other irregularities are clearly visible. The noise level

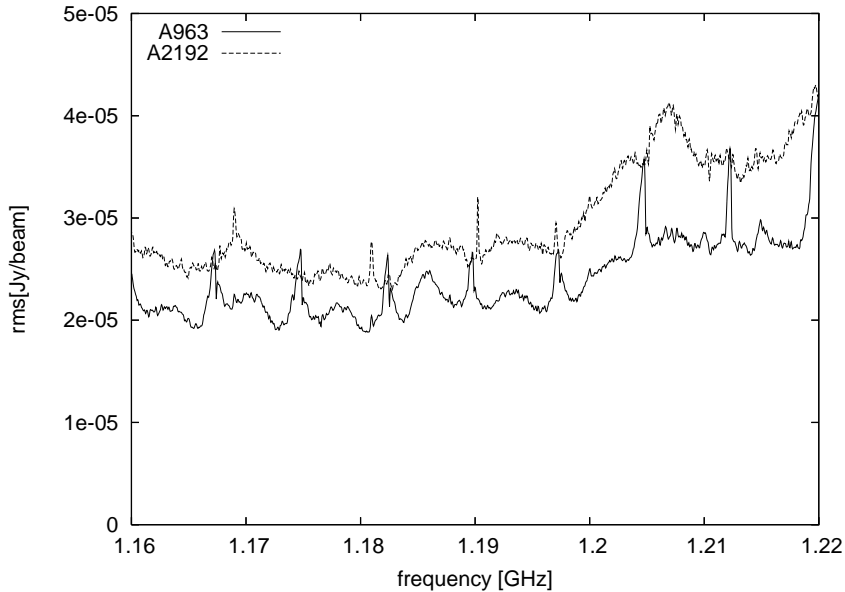


Figure 2.25: The rms noise in the two data cubes, after velocity smoothing down to 44 km s^{-1} . The figure is a re-print from Deshev et al. (2009).

achieved is very close to the expected one given the invested exposure time.

Fig. 2.26 shows the distribution of pixel values in the two data cubes at resolution of 80 km s^{-1} (gray lines). The data for A963 is shown on the left and A2192 on the right panel. The red lines show a Gaussian fit to the negative part of the histograms. The two fits have a mean of $-1.36 \mu\text{Jy}$ and $-0.28 \mu\text{Jy}$ for A963 and A2192, respectively, and a standard deviations of $23.98 \mu\text{Jy}$ and $26.90 \mu\text{Jy}$. The presence of positive signal in both cubes is visible, particularly in the A963 cube owing to the greater integration time (by a factor of 1.65). Also visible is the presence of (very few) strong negative peaks in the A963 data, above the expected Gaussian distribution, due to the already described problems with the calibration caused by the presence and distribution of strong continuum sources in the field.

Fig. 2.27 shows a slice through the A963 data cube at constant declination. Few "features" of the data are visible: a flagged region due to the presence of a strong continuum source, near the right edge of the image, few HI detections, as well as some of the structure in the noise.

Fig. 2.28 shows the amount of data lost due to RFI in percentage of all the data. This does not include the amount lost due to technical problems with the telescope, which was very small. The severity of the problem varies with the frequency, with the high frequency end being a factor of 1.5–7 more polluted. The best measurements, at around 1160MHz, have no less than 5% of the data lost due

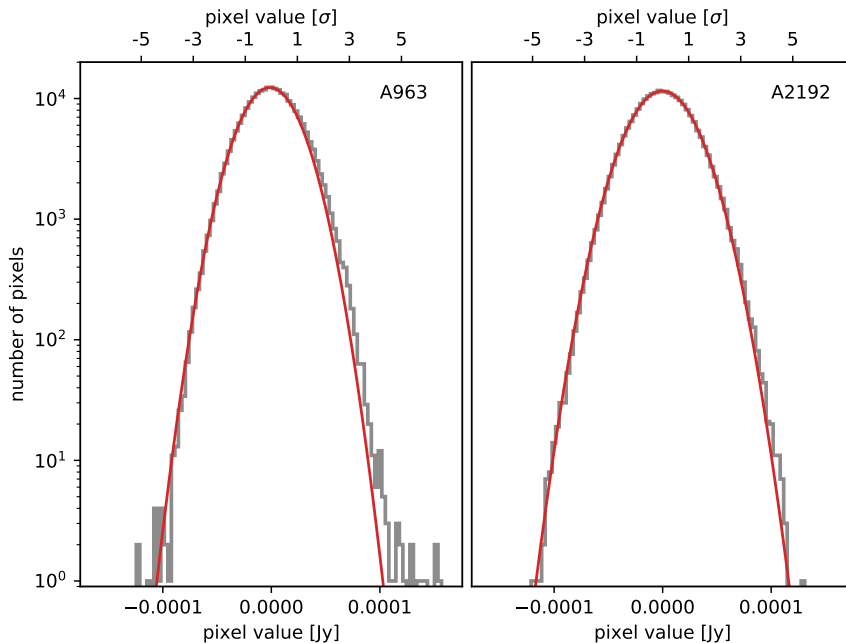


Figure 2.26: Histogram of the pixel distributions of the two data cubes at velocity resolution of 80 km s^{-1} (gray lines). The red lines show a Gaussian fit to the negative part of the histograms.

to RFI. This percentage is around the upper limit for the low redshift H I surveys, which are within the protected L band. Visible in the plot is also a clear trend with time. While the low frequency end is more or less the same for all 4 years of the survey, 2.5–3 times more data was lost, above 1.2GHz from the measurements from 2007 and 2008 when compared to the earlier ones. The likely, at least partial, cause for this was the introduction of the European satellite navigation system Galileo. The system is planned to have 30 operational satellites transmitting signals at 1176.45 MHz, 1207.14 MHz and 1227.6 MHz, among others (European Radio Navigation Plan <http://ec.europa.eu/DocsRoom/documents/33024>). During the period 2005-2008, when our WSRT data were collected, only two of those satellites were operational. The trend of ever increasing presence of man made interference in the L band is expected to continue in the future and we can conclude that redshifted 21 cm surveys of the universe, particularly around $z = 0.2$, will be exceedingly more difficult in the future, despite the vast improvement in observational capabilities that instruments like SKA will offer (<https://www.skatelescope.org/>).

Continuum flux density comparison

Due to the obvious lack of published H I flux densities at those redshifts, we are checking the accuracy of our calibration against published continuum flux densities. Fig. 2.29 shows a comparison between the flux densities of the continuum sources in the two fields, measured from the images similar to the ones shown in

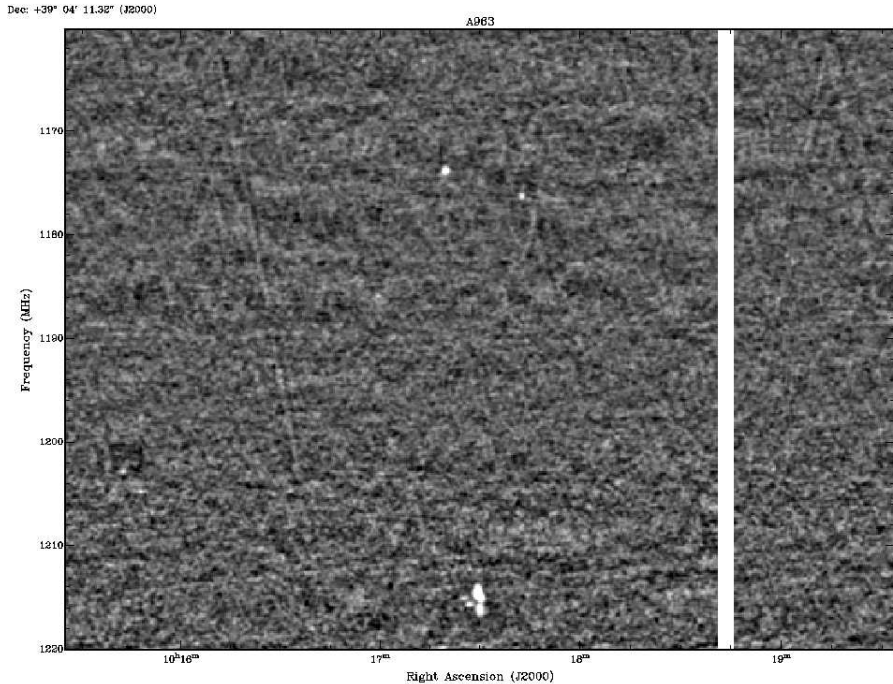


Figure 2.27: A slice at a constant declination through the data cube with resolution of 80 km s^{-1} . The white stripe on the right is a flagged region originally containing a strong continuum source. Visible is a group of 4 detections at bottom-middle (low z), as well as two more at similar right ascension but lower frequency. Mostly visible at lower R.A. (left), and spanning the whole frequency range are tilted straight lines caused by variations of the band-pass, for distant sources, and RFI. The rms noise increases slightly in the high frequency end of the survey (towards the bottom).

figs. 2.19 and 2.20 and the expected flux densities for those sources. The expected flux was interpolated from the flux values from the FIRST survey (Becker et al. 1995) at 1400 MHz, and the WENSS survey (Rengelink et al. 1997) at 325 MHz, assuming an exponential spectral index. In total 16 continuum sources that could be reliably measured in all eight bands of the WSRT survey were found to have published flux densities at 1400 and 330 MHz. 11 in the field of A963 and 5 in A2192. On Fig. 2.29 the strongest outliers for the two fields are not plotted or taken into account in calculating the statistics of the distribution. The strongly varying among the different bands errorbars in A2192 are most likely due to the small (4) number statistics. All the bands, except IF8 are very consistent with the expected flux density, within the errorbars. The deviation of IF8 is perhaps due to the increased amount of RFI in that band (see Fig. 2.28), which can increase the system temperature and lower the correlation, lowering as well the measured flux densities for sources in that band. The offset is however less than 10%. This is lower than the effect of other sources of error in the final H I flux density val-

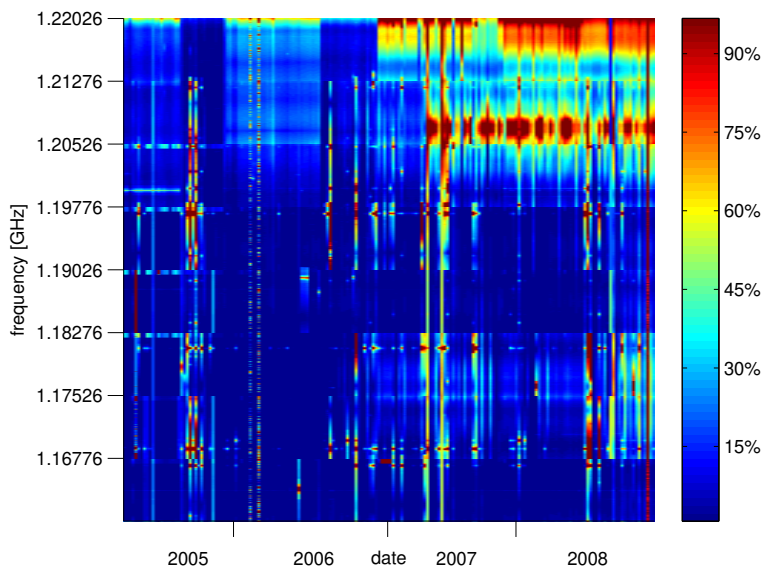


Figure 2.28: Amount of data lost due to RFI. The high frequency end of the survey is severely affected as well as the later observations.

ues, like for example, the imperfection of the masks for extracting the signal and continuum subtraction. After carefully checking the HI flux densities measured in IF8 compared to the ones from other bands, we decided that the IF8 fluxes are not less accurate than the other 7 bands.

Fig. 2.30 shows a comparison between the positions of the centroids of continuum sources. The top row shows the offset in the positions between our IF8 and the FIRST survey, the bottom between our IF1 and IF8. The vectors are magnified 100 times, for visibility. The negligibly small and random offsets are indicative of a good phase calibration. Excluding the few larger vectors, likely due to low signal to noise ratio, all the shifts in the positions are smaller than the pixel size in the continuum images ($6''$).

2.2.4 Source detection

Before searching for HI signal, we produced four data cubes per cluster with velocity resolution of 20, 40, 60 and 80 km s^{-1} . We masked out all the places with strong residuals from radio continuum emission and a perimeter of 5 pixels at the edge of all the cubes. The masked regions account for $\sim 10\%$ of the surveyed volume in the field of A963 and below 8% in the A2192 data cubes, where the continuum residuals of only two sources were visible, as opposed to the ~ 20 in the first one. Particular attention is required in the center of the data cube of A963. The imperfect model of “4C +39.29” causes the noise in the central $\sim 2'$ to deviate from the expected Gaussian distribution. This region in fact contains most of the

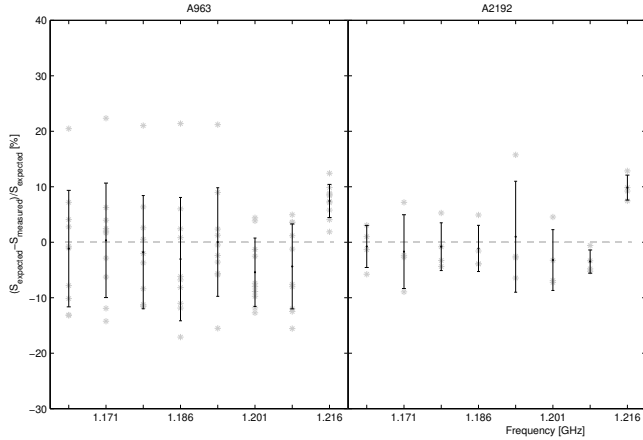


Figure 2.29: Comparison between the continuum flux densities calculated from WENSS and FIRST surveys values at 325 and 1400 MHz, and the measured fluxes in the eight bands of the WSRT survey. The comparison is based on 10 sources in the field of A963 (left), and 4 sources in the field of A2192 (right). The black points and the error bars shows the mean and the standard deviation of the flux differences for all the sources, while the gray stars show the individual sources.

negative detections found in that data cube. All the detections found there were discarded from the H I catalog. We clipped the cubes at a level of 3σ , 4σ , 5σ and 8σ and searched for peaks connected in the velocity direction. The adopted criteria for objects was a 3σ peak, if met in four adjacent velocity resolution elements, 4σ in three velocity resolution elements, 5σ peak in two and 8σ in one velocity resolution element. The catalog contains all the objects satisfying any of those criteria and at any velocity resolution. The comparison of the flux to the noise was done taking the local noise pattern for every detection. For every detection the mean noise vector from eight positions surrounding the detection and separated by one synthesised beam was taken.

To get an estimate of the number of false detections we repeated the search, with the same conditions for negative peaks. The results from both the positive and negative detection search are shown in figs.2.32 – 2.35. Visible on those figures is the stronger tendency of the positive detections to follow the expected sensitivity pattern of the primary beam, while the negative objects are much more uniformly distributed over the sky coverage of the data cubes. All the positive detections were visually inspected and the ones that are clearly associated with some localised structures in the noise or with a concentration of negative detections were discarded. The rest were examined for counterparts in the optical B and R and the NUV and FUV Galax data. Again the ones without a counterparts within the 3σ contours were discarded. This selection was based on the relatively high total H I mass detection limit, and the fact that no H I survey has ever shown

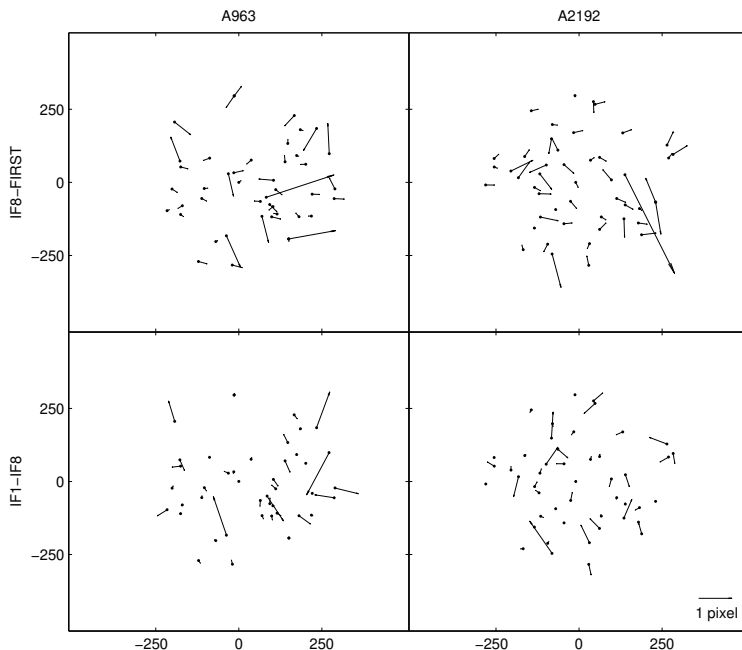


Figure 2.30: Vectors showing the distances between the positions of continuum sources. The left panel is for the field of A963, the right one for A2192. The top row shows the offset between IF8 and the FIRST survey, the bottom between IF1 and IF8. For clarity the vectors are magnified 100 times.

the presence of a population of dark H I clouds with total gas mass as high as $10^9 M_{\odot}$.

2.2.5 Correction for instrumental broadening

Tables 2.2 and 2.3 list the widths of the global H I profiles of sources at 20% and 50% of their peak flux. Those values were measured from the highest resolution data cube, and are the average between two measurements taken inside-out and outside-in. The finite instrumental, velocity resolution results in a broadening of the velocity profiles of the galaxies which has to be corrected for. The lower resolution profiles showed no dependence on the method of measurement, and were used to estimate the necessary correction for instrumental broadening. We adopt a linear correction with resolution R. We apply a correction δW to the observed profile width in a sense $W = W^{obs} - \delta W$. In order to estimate δW we fit a straight line to the widths of the velocity profiles of all the sources, measured at resolution of 20, 40 and 80 km/s. The distribution of the slopes of all the fits is shown with dotted lines in Fig. 2.31. The applied corrections are shown with the vertical dashed lines, and are the mean of the distribution of the slopes of the sources shown with solid line. Those sources were selected, to satisfy a minimum profile

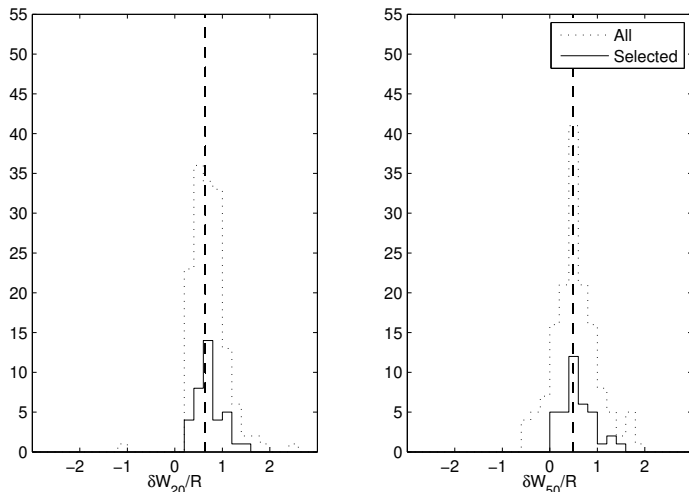


Figure 2.31: Distribution of the estimated correction of the velocity width for all the sources in the two clusters, for the width measured at 20% of the peak flux (left), and 50% (right). The dashed lines show the mean of the distribution of the selected sources (solid line), which is the applied correction. See the text for details.

width of 240 km s^{-1} , at the lowest resolution, difference between the inside-out and outside-in measurements no greater than 3 channels, rms of the fit no greater than 30 km s^{-1} , and to have a positive slope no greater than 2. The selection criteria were set to neglect the effects of noise in the measurements, and affect the final correction values by $< 2\%$. The final applied corrections are $\delta W_{20} = 0.5915 \times R$ and $\delta W_{50} = 0.4272 \times R$, where R is the velocity resolution in km s^{-1} .

For comparison, the most widely used approach to correct for instrumental broadening is presented by Bottinelli et al. (1990). Using a more elaborate, but similarly empirical approach they find $\delta W_{20} = 0.55 \times R$, and $\delta W_{50} = 0.13 \times R$. Verheijen & Sancisi (2001) find a minor deviation from Bottinelli et al.’s result, increasing with decreasing resolution, resulting in $\delta W_{20} \sim 0.76 \times R$ and $\delta W_{50} \sim 0.52 \times R$. The second paper used a more analytical approach, assuming a Gaussian shape of the profile. The intermediate incidence of our δW values, produced by a purely empirical approach is encouraging. The insignificant deviations can be attributed partially to the lower velocity resolution we are using in our research (80 km s^{-1}), but are most likely determined by the significantly lower signal to noise level of our sources.

In total the survey detected 158 galaxies, 116 in the field of A963 and 42 in the field of A2192. Their main properties are listed in tables 2.2 and 2.3. The tables list the following parameters: Column(1)–Internal designation of the source; (2)–RA in J2000.0; (3)–Dec in J2000.0; (4)– z ; (5)–Peak flux density, corrected for primary beam attenuation; (6)–Total flux in the line, corrected for primary beam attenuation; (7)–Total H I mass; (8)–Width of the profile at 20% of the maximum;

(9)–Width of the profile at 50% of the maximum; (10)–Profile type; (11)–Absolute B-band magnitude; (12)–Absolute R-band magnitude. The total H I mass is calculated as $M_{\text{HI}} = 2.36 \times 10^5 \times d^2 \times S dv$. Where d is the luminosity distance, S is the total flux density in the line and dv is the channel width in km s^{-1} . While the source detection is done at a range of velocity resolutions, all the measurements are taken from the highest resolution data cube ($\sim 17 \text{ km s}^{-1}$). The types of global H I profiles are 1-double peaked, 2-Gaussian, 3-Distorted and 4-Boxy, with the exact definition taken from Verheijen & Sancisi (2001). Few sources, that are truncated by the bandwidth of the observations, have no quoted profile type or width. The uncertainties in the flux density show the rms noise in every channel showing emission from the given source. Those are then summed in quadrature to give the uncertainty in the total flux in the 21 cm line and converted to uncertainty in M_{HI} according to the formula given above. The quoted uncertainties are likely underestimated as we do not account for the errors in making the masks for source extraction. Two H I detections in the field of A963 are not covered by the optical INT data. For those we provide the SDSS g and r band magnitudes instead.

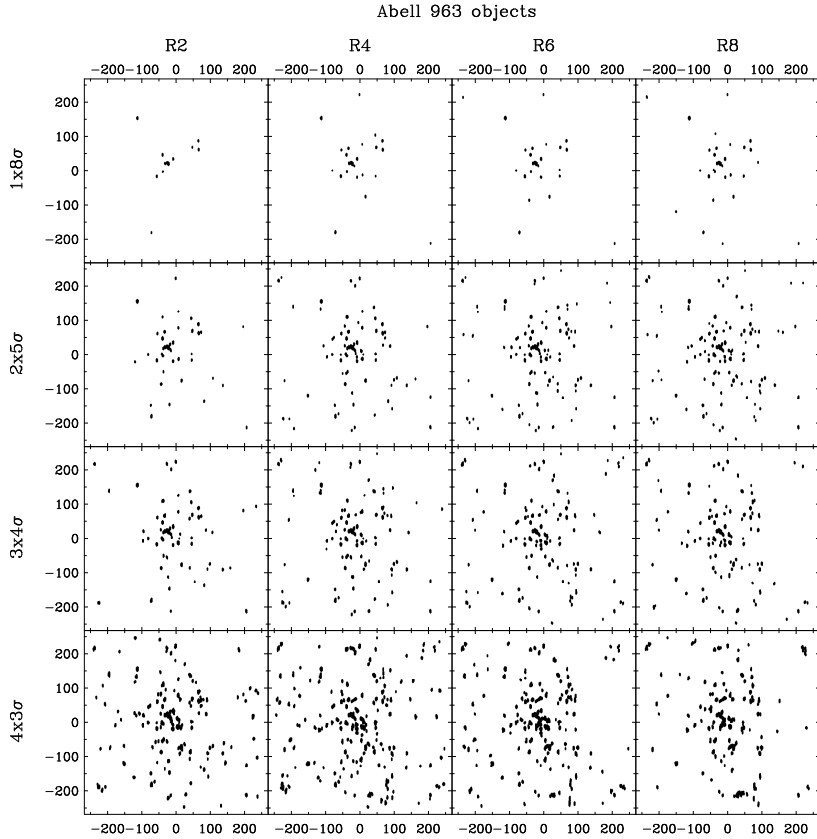


Figure 2.32: Map showing all the objects found in the data cube of A963 at different combinations of resolution and detection criteria. For clarity the size of the objects is increased by 50%.

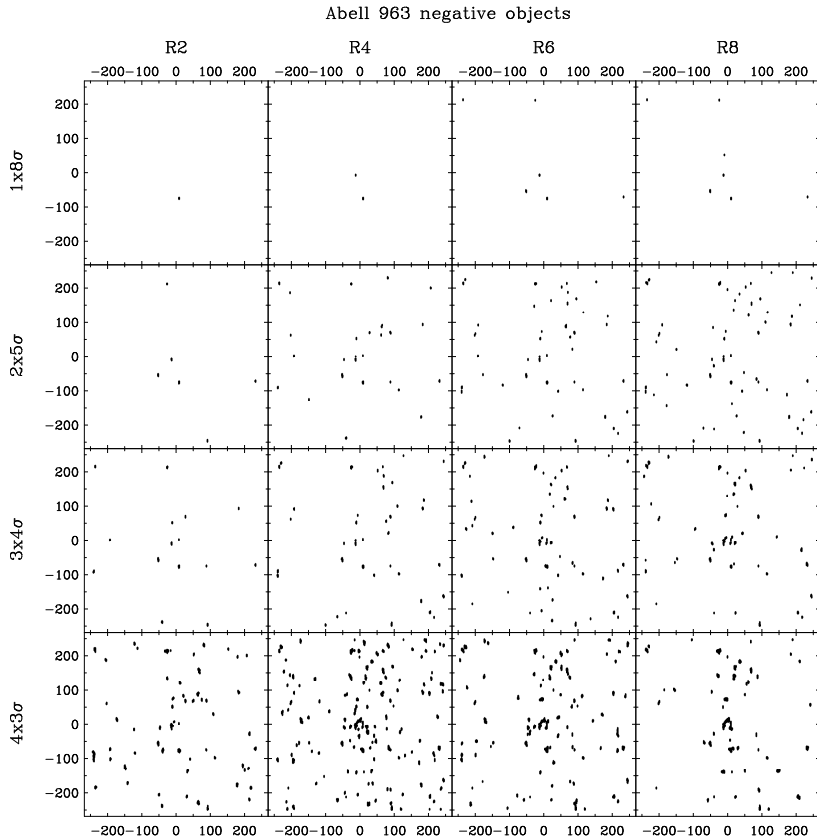


Figure 2.33: Map showing all the negative objects found in the data cube of A963 at different combinations of resolution and detection criteria. For clarity the size of the objects is increased by 50%.

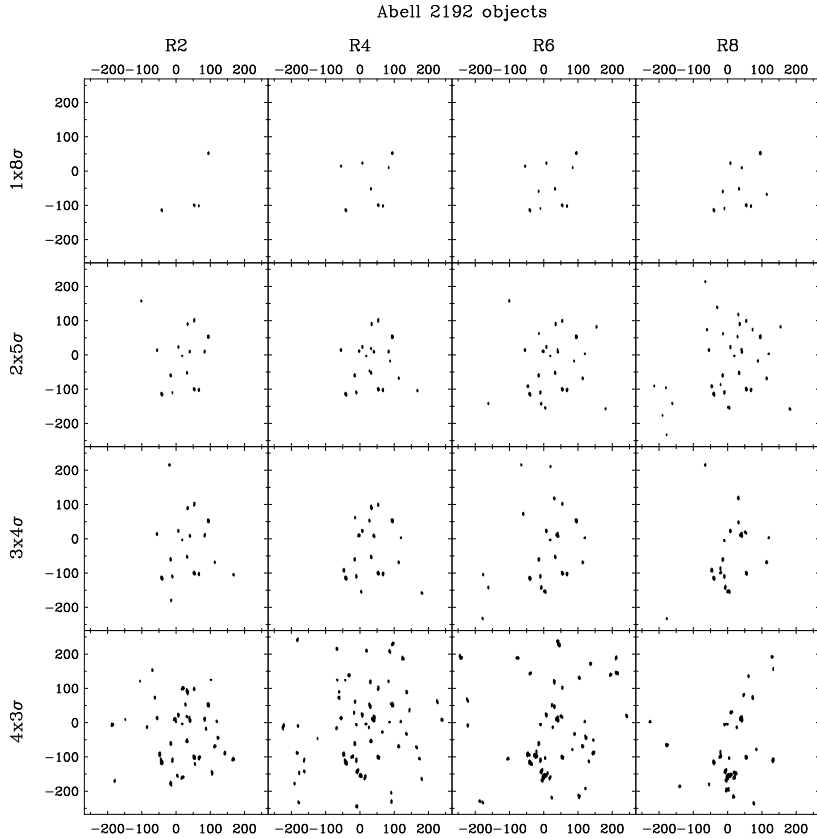


Figure 2.34: Map showing all the objects found in the data cube of A2192 at different combinations of resolution and detection criteria. For clarity the size of the objects is increased by 50%.

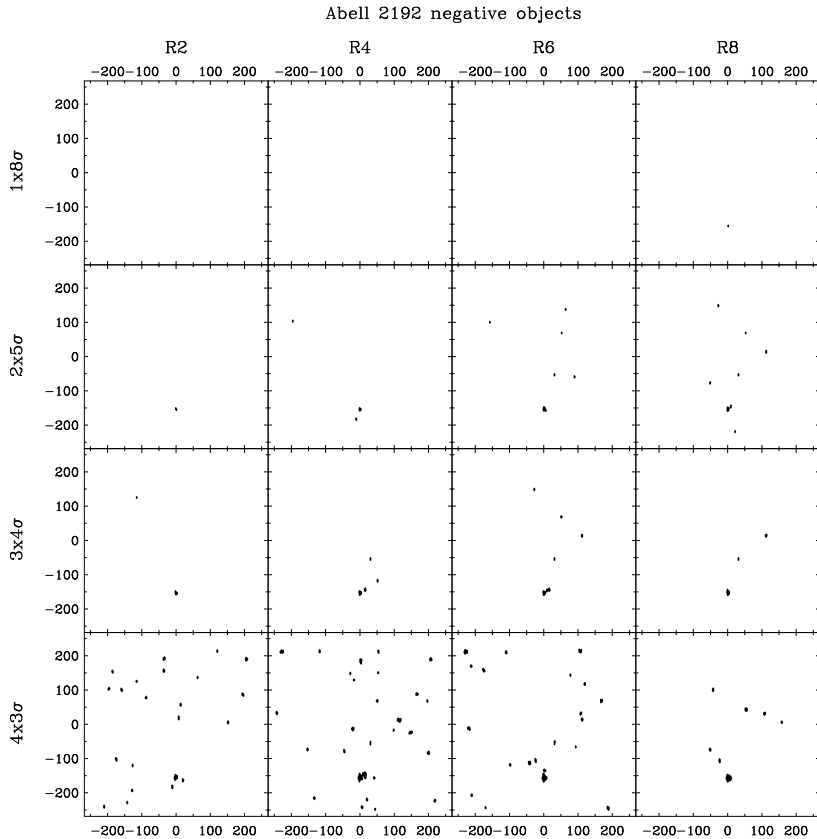


Figure 2.35: Map showing all the negative objects found in the data cube of A2192 at different combinations of resolution and detection criteria. For clarity the size of the objects is increased by 50%.

Table 2.2: A963 H I detections

name	RA [deg]	Dec [deg]	redshift	Peak flux density [μ Jy/beam]	total H I flux [mJy km s ⁻¹]	H I mass [10 ⁹ M _⊙]	W ₂₀ [km s ⁻¹]	W ₅₀ [km s ⁻¹]	profile type	B mag (11)	R mag (12)
(1)	(2)	(3)	(4)	(5)	(6)	(7)	(8)	(9)	(10)	(11)	(12)
A963H136	153.6628	38.9132	0.174	545	56.30±0.73	7.9±1.0	107	70	2	-18.60	-19.85
A963H131	153.8498	39.1639	0.190	187	36.23±1.21	6.2±2.0	385	341	1	-20.49	-21.30
A963H133	153.8971	38.9619	0.220	110	17.40±0.74	4.0±1.6	215	34	3	-18.89	-19.55
A963H135	153.9000	38.7615	0.206	263	36.40±0.68	7.3±1.3	229	169	2	-20.77	-21.25
A963H132	153.9033	39.0606	0.210	166	27.26±0.68	5.7±1.4	198	156	3	-19.57	-20.38
A963H134	153.9174	38.8223	0.204	266	48.71±0.70	9.5±1.3	261	180	3	-20.95	-21.93
A963H138	154.0021	38.8699	0.209	159	16.99±0.54	3.5±1.1	127	110	2	-19.38	-19.70
A963H139	154.0265	38.8579	0.207	183	34.75±0.81	7.1±1.6	268	184	2	-19.55	-20.30
A963H141	154.0464	38.8231	0.207	196	60.64±1.13	12.3±2.2	474	450	3	-21.56	-22.53
A963H1100	154.0569	39.0773	0.190	158	45.81±1.21	7.7±1.9	413	357	1	-20.21	-21.13
A963H140	154.0610	38.8566	0.207	144	33.06±0.93	6.7±1.8	280	242	3	-19.47	-20.12
A963H1137	154.0748	38.7151	0.170	295	30.53±0.57	4.1±0.7	113	76	2	-20.25	-20.95
A963H197	154.0875	39.1345	0.207	72	10.50±0.41	2.1±0.8	179	164	1	-19.37	-19.86
A963H189	154.0880	39.2641	0.167	170	35.63±1.05	4.6±1.3	288	231	2	-18.33	-18.98
A963H196	154.0979	39.1651	0.210	111	12.29±0.40	5.4±0.8	139	72	3	-23.64	-24.67
A963H1143	154.1000	39.1281	0.202	120	15.27±0.51	2.9±0.9	169	95	2	-19.23	-19.67
A963H147	154.1044	38.7340	0.208	163	34.43±0.93	7.0±1.8	361	237	2	-18.40	-18.90
A963H194	154.1045	39.1848	0.168	189	52.43±1.46	6.9±1.8	393	349	1	-19.67	-20.21
A963H186	154.1106	39.3166	0.217	256	74.71±1.23	16.8±2.7	424	388	2	-20.03	-21.12
A963H199	154.1165	39.0829	0.165	147	30.69±1.27	3.9±1.5	301	209	1	-19.50	-19.87
A963H195	154.1181	39.1589	0.211	314	42.29±0.68	8.9±1.4	208	126	2	-21.61	-22.27
A963H190	154.1209	39.2162	0.210	315	84.40±1.12	17.7±2.3	432	290	3	-20.47	-22.05
A963H146	154.1512	38.7438	0.207	172	33.86±0.94	6.9±1.8	285	123	2	-19.61	-20.13
A963H187	154.1675	39.2855	0.203	135	30.15±0.80	5.9±1.5	346	327	2	-18.65	-18.60
A963H142	154.1693	38.9079	0.202	88	13.57±0.52	2.6±1.0	228	221	3	-20.46	-22.39
A963H191	154.1714	39.1737	0.210	186	49.85±1.08	10.5±2.2	395	278	1	-20.64	-21.15
A963H1115	154.1770	39.0262	0.165	276	39.40±1.00	5.0±1.2	0 ^a	0 ^a	0 ^a	-20.19	-20.56
A963H1118	154.1773	38.9846	0.169	183	51.02±1.74	6.8±2.2	409	252	3	-19.62	-20.10
A963H188	154.1797	39.2538	0.218	146	16.29±0.53	3.7±1.2	94	36	2	-20.00	-20.50
A963H193	154.1850	39.1293	0.208	99	15.83±0.59	3.2±1.2	241	227	2	-19.68	-20.45
A963H184	154.1904	39.3296	0.169	312	67.67±1.45	9.0±1.8	320	251	2	-19.55	-19.89
A963H144	154.1932	38.8318	0.201	162	31.28±0.64	6.0±1.2	256	185	2	-18.22	-18.99

Table 2.2: continued

name	RA [deg] (2)	Dec [deg] (3)	redshift (4)	Peak flux density [μ Jy/beam] (5)	total H I flux [mJykm s ⁻¹] (6)	H I mass [10 ⁹ M _⊙] (7)	W ₂₀ [km s ⁻¹] (8)	W ₅₀ [km s ⁻¹] (9)	profile type (10)	B mag (11)	R mag (12)
A963H145	154.1932	38.7895	0.209	126	13.17±0.43	2.7±0.9	100	73	2	-20.07	-20.56
A963H192	154.1958	39.1509	0.210	95	11.92±0.52	2.5±1.0	147	114	3	-19.42	-19.70
A963H166	154.2401	38.8865	0.198	113	45.17±1.63	8.4±2.9	577	526	1	-17.08	-18.01
A963H160	154.2548	38.7162	0.203	97	24.00±0.92	4.7±1.7	348	232	2	-19.89	-20.51
A963H1125	154.2560	39.0024	0.165	164	20.34±0.65	2.6±0.8	0 ^a	0 ^a	0 ^a	-18.96	-19.45
A963H1140	154.2587	38.8631	0.216	106	21.62±0.94	4.8±2.0	308	266	3	-17.91	-19.03
A963H163	154.2611	38.8528	0.206	222	58.44±1.18	11.7±2.3	369	342	1	-19.33	-20.29
A963H181	154.2687	39.1709	0.220	147	24.54±0.85	5.6±1.9	264	94	3	-19.49	-20.19
A963H159	154.2704	38.7149	0.181	181	50.94±1.40	7.8±2.0	418	305	4	-19.05	-20.17
A963H183	154.2704	39.3015	0.208	161	20.61±0.52	4.2±1.0	166	128	2	-19.36	-20.07
A963H162	154.2732	38.8243	0.204	156	40.82±1.22	8.0±2.3	497	459	3	-20.63	-21.61
A963H182	154.2890	39.2998	0.219	142	14.20±0.53	3.2±1.2	108	74	2	-18.96	-19.58
A963H180	154.2892	39.1941	0.218	115	26.30±0.83	6.0±1.8	291	247	1	-19.72	-20.25
A963H161	154.2958	38.7899	0.207	104	25.20±1.04	5.1±2.0	375	216	2	-18.23	-18.50
A963H167	154.2993	38.9051	0.216	146	32.40±0.95	7.2±2.0	353	289	3	-19.14	-20.01
A963H1142	154.3010	39.1899	0.210	64	7.12±0.51	1.5±1.0	136	113	2	-18.34	-18.90
A963H158	154.3028	38.7414	0.206	88	12.09±0.61	2.4±1.2	204	144	2	-19.68	-20.30
A963H179	154.3223	39.2265	0.211	107	24.86±0.82	5.2±1.7	337	326	2	-20.29	-20.71
A963H1130	154.3314	39.0994	0.210	259	42.16±0.60	8.8±1.2	247	161	2	-19.57	-19.92
A963H1124	154.3318	38.9765	0.217	206	35.39±0.76	7.9±1.6	271	160	3	-19.41	-19.68
A963H157	154.3354	38.7682	0.207	125	24.96±0.80	5.0±1.6	335	241	2	-19.90	-20.42
A963H177	154.3366	39.1815	0.198	111	34.31±1.20	6.4±2.1	411	324	3	-20.32	-21.50
A963H128	154.3479	39.4698	0.203	386	66.62±0.80	12.9±1.5	262	188	2	-18.65	-19.07
A963H115	154.3514	38.5522	0.179	404	80.11±1.16	12.1±1.7	276	229	1	-18.05	-20.22
A963H1133	154.3551	39.0556	0.208	164	44.36±1.06	9.1±2.1	375	326	1	-20.35	-21.13
A963H1134	154.3600	39.0855	0.169	158	28.87±1.14	3.8±1.4	275	232	1	-19.17	-19.53
A963H19	154.3627	38.6963	0.206	228	25.14±0.42	5.1±0.8	134	84	2	-21.06	-21.98
A963H1139	154.3644	38.7763	0.201	124	37.02±1.17	7.1±2.1	471	422	3	-20.64	-21.46
A963H1122	154.3680	38.9993	0.200	79	12.67±0.54	2.4±1.0	226	214	2	-19.56	-20.01
A963H156	154.3726	38.7743	0.169	146	16.26±0.54	2.2±0.7	130	107	3	-18.41	-19.17
A963H1123	154.3734	38.9751	0.204	63	16.57±0.90	3.3±1.7	393	358	2	-19.75	-20.67
A963H1135	154.3747	39.0698	0.169	1038	310.63±3.16	41.6±4.0	542	268	2	-21.15	-21.73

Table 2.2: continued

name	RA [deg]	Dec [deg]	redshift	Peak flux density [μ Jy/beam]	total H I flux [mJykm s ⁻¹]	H I mass [10 ⁹ M _⊙]	W ₂₀ [km s ⁻¹]	W ₅₀ [km s ⁻¹]	profile type	B mag (11)	R mag (12)
(1)	(2)	(3)	(4)	(5)	(6)	(7)	(8)	(9)	(10)	(11)	(12)
A963H114	154.3753	38.5326	0.205	340	66.86±0.94	13.2±1.8	338	94	2	-21.60	-22.86
A963H113	154.3793	38.5738	0.204	215	58.43±0.99	11.5±1.9	377	310	2	-21.30	-22.07
A963H153	154.3818	38.9002	0.216	131	22.39±0.82	5.0±1.8	266	174	3	-20.02	-20.49
A963H176	154.3928	39.2325	0.218	73	8.69±0.54	2.0±1.2	146	66	2	-19.86	-20.30
A963H1132	154.3981	39.0695	0.210	245	50.44±1.15	10.5±2.3	290	106	3	-20.26	-21.12
A963H172	154.4048	39.1676	0.218	213	65.61±1.28	14.8±2.8	500	431	1	-20.44	-21.51
A963H1138	154.4102	38.9098	0.206	136	32.69±0.95	6.6±1.8	407	303	3	-20.14	-20.88
A963H155	154.4122	38.8048	0.168	177	51.53±1.76	6.8±2.2	471	408	2	-18.98	-19.71
A963H1131	154.4141	39.0641	0.200	104	12.10±0.53	2.3±1.0	87	61	2	-19.50	-19.88
A963H175	154.4149	39.2636	0.218	166	56.93±1.17	12.9±2.6	469	446	1	-20.03	-21.11
A963H1121	154.4159	39.0144	0.208	196	31.78±0.63	6.3±1.2	196	164	1	-20.66	-21.92
A963H152	154.4202	38.8999	0.215	108	20.07±0.81	4.4±1.7	322	286	2	-19.13	-19.66
A963H173	154.4202	39.1262	0.209	272	37.25±0.79	7.7±1.6	183	129	2	-20.38	-20.78
A963H1145	154.4272	39.0214	0.208	140	27.96±0.93	5.7±1.8	291	158	2	-19.61	-20.67
A963H112	154.4283	38.5687	0.202	275	40.40±0.63	7.8±1.2	217	166	3	-18.16	-19.07
A963H154	154.4291	38.8317	0.207	220	37.68±0.72	7.6±1.4	290	159	2	-19.11	-19.38
A963H174	154.4350	39.2055	0.211	133	23.99±0.70	5.0±1.4	288	195	3	-19.85	-20.77
A963H1120	154.4357	39.0791	0.200	110	13.47±0.52	2.6±0.9	154	115	2	-19.83	-20.36
A963H1119	154.4511	39.0970	0.219	78	24.70±1.17	5.7±2.6	492	365	1	-19.59	-20.65
A963H151	154.4546	38.9000	0.207	170	23.05±0.66	4.7±1.3	382	243	3	-18.80	-19.35
A963H170	154.4629	39.1569	0.200	189	35.42±0.86	6.7±1.5	302	175	3	-19.52	-19.96
A963H1114	154.4674	38.9825	0.202	271	88.01±1.49	16.9±2.7	535	412	3	-19.70	-21.02
A963H1113	154.4676	39.0196	0.203	112	20.65±0.71	4.0±1.3	281	152	2	-19.07	-19.47
A963H110	154.4844	38.6363	0.204	153	27.57±0.69	5.4±1.3	269	186	2	-20.56	-20.95
A963H169	154.4887	39.1754	0.199	113	26.62±0.88	5.0±1.6	286	184	2	-18.47	-18.87
A963H1112	154.4981	39.0419	0.218	102	16.36±0.53	3.7±1.2	193	137	1	-18.87	-19.59
A963H1151	154.4999	39.1107	0.210	119	27.95±0.82	5.8±1.6	335	285	1	-20.56	-21.19
A963H1141	154.5003	39.2805	0.199	135	33.99±1.15	6.3±2.0	373	341	3	-18.76	-19.48
A963H168	154.5029	39.2957	0.204	123	22.94±0.70	4.5±1.3	274	201	3	-18.68	-19.03
A963H1111	154.5075	39.0695	0.202	85	11.47±0.41	2.2±0.8	142	129	3	-17.84	-18.38
A963H111	154.5115	38.6204	0.203	515	91.60±0.69	17.8±1.3	226	178	2	-20.73	-21.27
A963H149	154.5158	38.8542	0.204	105	22.06±0.62	4.4±1.2	273	239	2	-18.20	-18.50

Table 2.2: continued

name	RA [deg]	Dec [deg]	redshift	Peak flux density [μ Jy/beam]	total H I flux [mJykm s ⁻¹]	H I mass [10 ⁹ M _⊙]	W ₂₀ [km s ⁻¹]	W ₅₀ [km s ⁻¹]	profile type	B mag (11)	R mag (12)
(1)	(2)	(3)	(4)	(5)	(6)	(7)	(8)	(9)	(10)	(11)	(12)
A963H17	154.5160	38.6903	0.205	228	79.44±1.50	15.9±2.9	571	508	3	-21.54	-22.49
A963H1144	154.5254	39.1309	0.208	99	41.27±0.80	8.5±1.6	203	156	3	-20.45	-21.38
A963H1109	154.5387	39.1218	0.207	132	37.99±1.00	7.7±1.9	436	369	2	-20.37	-21.09
A963H1108	154.5388	39.0217	0.204	163	30.09±0.69	5.9±1.3	223	186	4	-17.84	-17.77
A963H1107	154.5766	39.0707	0.217	170	23.34±0.60	5.2±1.3	160	64	2	-19.73	-20.82
A963H1104	154.5831	39.0031	0.206	147	31.79±0.83	6.4±1.6	315	225	3	-20.50	-21.10
A963H1106	154.6105	39.0782	0.220	119	15.23±0.66	3.5±1.5	207	90	2	-19.22	-19.62
A963H123	154.6315	39.3686	0.218	932	141.25±0.87	31.8±1.9	207	133	2	-22.18	-23.17
A963H121	154.6369	39.3183	0.187	248	42.74±0.85	7.0±1.3	257	166	2	-18.73	-18.86
A963H122	154.6371	39.3346	0.204	159	24.77±0.51	4.9±1.0	216	199	2	-19.04	-19.66
A963H1105	154.6383	39.0675	0.203	136	38.52±0.97	7.5±1.8	405	321	1	-21.39	-22.15
A963H1103	154.6465	38.9718	0.167	224	63.19±1.65	8.2±2.0	404	325	1	-20.55	-21.60
A963H125	154.6480	39.5097	0.201	509	64.50±0.64	12.3±1.2	168	134	2	-18.47	-19.15
A963H16	154.6522	38.6643	0.218	311	69.65±1.05	15.7±2.3	345	166	2	-18.79	-19.15
A963H1102	154.6924	38.9873	0.201	179	35.08±0.73	6.7±1.3	240	213	1	-20.60	-21.36
A963H15	154.7391	38.7572	0.176	430	81.39±1.20	11.8±1.6	247	179	3	-20.51	-21.28
A963H1101	154.7641	39.0384	0.217	198	22.71±0.44	5.1±1.0	165	126	2	-19.38	-19.97
A963H119	154.8088	39.1924	0.204	269	77.82±1.13	15.4±2.1	487	473	3	-20.98	-21.92
A963H12	154.8924	38.6031	0.201	778	188.30±0.85	35.8±1.6	360	354	3	-21.63 ^b	-22.83 ^c
A963H11	154.9424	38.6041	0.209	832	114.82±0.53	23.8±1.1	170	143	2	-20.36 ^b	-21.34 ^c

Notes. (a) Global profile truncated by the survey bandwidth; (b) SDSS absolute g'-band magnitude; (c) SDSS absolute r'-band magnitude;

Table 2.3: A2192 H I detections

name	RA [deg]	Dec [deg]	redshift	Peak flux density [$\mu\text{Jy}/\text{beam}$]	total H I flux [mJy km s^{-1}]	H I mass [$10^9 M_{\odot}$]	W_{20} [km s^{-1}]	W_{50} [km s^{-1}]	profile type	B mag (11)	R mag (12)
(1)	(2)	(3)	(4)	(5)	(6)	(7)	(8)	(9)	(10)	(11)	(12)
A2192H1.36	245.9278	42.6863	0.175	460	89.41±1.19	12.5±1.6	212	134	2	-17.33	-18.27
A2192H1.24	246.2189	42.4735	0.189	215	41.66±0.99	6.9±1.6	233	173	3	-19.17	-19.67
A2192H1.26	246.2840	42.5688	0.187	132	13.93±0.55	2.3±0.9	125	49	3	-20.97	-21.80
A2192H1.48	246.2937	42.6744	0.187	129	27.03±0.96	4.4±1.5	271	260	3	-19.96	-20.49
A2192H1.25	246.3135	42.5150	0.187	209	34.58±0.71	5.5±1.1	218	180	3	-20.31	-20.95
A2192H1.37	246.3683	42.7840	0.189	427	50.03±0.78	8.3±1.2	150	123	3	-21.34	-21.91
A2192H1.46	246.3895	42.6265	0.201	73	14.46±0.95	2.4±1.4	340	306	1	-17.68	-19.41
A2192H1.45	246.4003	42.9319	0.168	124	20.28±0.89	2.6±1.1	199	150	1	-19.72	-20.27
A2192H1.47	246.4014	42.6905	0.190	162	14.21±0.42	2.4±0.7	77	54	3	-19.71	-20.27
A2192H1.38	246.4357	42.8304	0.170	226	49.08±1.41	6.5±1.8	314	255	1	-20.89	-22.14
A2192H1.23	246.4509	42.4410	0.190	290	32.68±0.87	5.4±1.4	118	90	2	-20.87	-21.34
A2192H1.21	246.4863	42.4043	0.190	116	13.67±0.71	2.3±1.1	154	106	2	-19.31	-20.08
A2192H1.42	246.4915	42.8875	0.169	252	64.12±2.34	8.3±2.9	536	504	1	-21.28	-22.36
A2192H1.22	246.4926	42.4459	0.189	269	63.39±1.25	10.4±1.9	304	282	1	-21.28	-22.20
A2192H1.49	246.4997	42.7107	0.175	133	20.22±1.28	2.8±1.7	226	111	2	-19.82	-20.75
A2192H1.39	246.5125	42.8469	0.189	92	18.83±1.13	3.1±1.8	332	219	3	-19.47	-20.53
A2192H1.63	246.5317	42.6895	0.190	134	36.26±1.70	6.0±2.7	406	304	3	-20.91	-21.68
A2192H1.50	246.5329	42.7037	0.190	74	14.82±0.86	2.5±1.4	259	249	2	-20.90	-21.68
A2192H1.40	246.5494	42.8642	0.188	167	17.49±0.69	2.9±1.1	127	49	2	-19.74	-20.35
A2192H1.19	246.5550	42.5500	0.224	164	31.55±0.96	7.4±2.2	0 ^a	0 ^a	0 ^a	-21.36	-22.03
A2192H1.52	246.5598	42.7742	0.192	121	20.75±0.83	3.5±1.3	252	121	3	-19.60	-20.32
A2192H1.20	246.5680	42.5619	0.224	70	8.07±0.64	1.9±1.5	0 ^a	0 ^a	0 ^a	-18.88	-19.35
A2192H1.62	246.5688	42.7845	0.191	93	12.33±0.83	2.1±1.3	159	93	2	-17.67	-17.32
A2192H1.60	246.5756	42.6356	0.191	79	22.15±1.57	3.7±2.5	499	480	1	-19.64	-20.63
A2192H1.41	246.5910	42.8907	0.188	107	11.20±0.69	1.8±1.1	104	70	2	-21.99	-23.26
A2192H1.59	246.5984	42.6600	0.172	133	20.69±1.10	2.8±1.4	188	172	2	-18.29	-18.85
A2192H1.53	246.6316	42.7197	0.191	169	26.27±1.01	4.4±1.6	201	151	3	-21.50	-22.16
A2192H1.56	246.6576	42.6922	0.209	117	11.93±0.50	2.4±1.0	105	86	3	-20.63	-21.82
A2192H1.57	246.6846	42.6530	0.191	84	15.79±0.99	2.6±1.6	294	278	1	-19.19	-19.74
A2192H1.16	246.6847	42.4253	0.189	192	32.29±1.14	5.3±1.8	236	149	3	-21.95	-22.77
A2192H1.18	246.6991	42.5328	0.221	147	25.49±0.90	5.8±2.0	247	202	3	-20.65	-21.51
A2192H1.14	246.7160	42.4517	0.188	82	17.75±0.98	2.9±1.5	279	226	1	-20.59	-21.07

Table 2.3: continued

name	RA [deg]	Dec [deg]	redshift	Peak flux density [μ Jy/beam]	total HI flux [mJykm s ⁻¹]	HI mass [10 ⁹ M _⊙]	W ₂₀ [km s ⁻¹]	W ₅₀ [km s ⁻¹]	profile type	B mag (11)	R mag (12)
(1)	(2)	(3)	(4)	(5)	(6)	(7)	(8)	(9)	(10)	(11)	(12)
A2192H115	246.7190	42.4760	0.221	87	18.48±0.94	4.2±2.1	315	297	2	-19.96	-20.60
A2192H131	246.7480	42.9781	0.186	151	19.06±0.58	2.7±1.2	140	118	3	-15.69	-17.11
A2192H111	246.7770	42.4147	0.188	387	103.83±1.59	17.0±2.5	419	394	1	-21.58	-22.64
A2192H112	246.7959	42.4652	0.173	246	32.79±1.12	4.5±1.4	202	127	2	-20.60	-21.50
A2192H128	246.8191	42.6997	0.190	123	15.42±0.70	2.3±1.3	117	61	2	-16.74	-17.79
A2192H129	246.8357	42.8290	0.220	89	16.76±0.88	3.8±1.9	279	205	2	-20.74	-21.78
A2192H130	246.8366	42.8651	0.174	94	13.97±1.06	1.9±1.4	194	112	3	-20.43	-21.81
A2192H127	246.9081	42.6367	0.201	97	10.82±0.48	2.0±0.9	151	107	2	-25.30	-26.14
A2192H133	246.9591	43.0175	0.189	253	30.48±0.71	5.0±1.1	151	59	2	-20.16	-20.64
A2192H12	247.1850	42.4369	0.171	223	40.05±0.90	5.4±1.1	213	199	4	-19.20	-19.66

Notes. (a) Global profile truncated by the survey bandwidth;

2.3 Wide field optical imaging of Abell 963 and Abell 2192

2.3.1 Observations

THE observations presented in this chapter were collected as a complimentary data to the HI survey presented in chapter 2.2.

The optical imaging of the two fields covered by the entire primary beam of WSRT was done with the Wide Field Camera (WFC) on the 2.54m Isaac Newton Telescope (INT) at the “Observatorio de la roque muchachos” on the island of La Palma, Spain. The camera, mounted in the primary focus of the telescope, consist of four thinned EEV CCD chips plus a fifth one for the autoguider. The active area of the scientific chips is 2048×4100 pixels. Including the overscan regions the total area is 2148×4128 pixels. Neglecting the interchip spacing, this mosaic camera covers $34' \times 34'$ on the sky. The pixels are $13.5 \times 13.5 \mu\text{m}$, corresponding to $0.333'' \times 0.333''$ on the sky.

The two fields, containing the galaxy clusters of interest Abell 963 and Abell 2192, were imaged in the Harris B and R filters. Every field was covered with 30 individual exposures, distributed in 6 partially overlapping pointings. In each pointing 5 individual exposures were collected, dithered around the center of the pointing, in order to fill the gaps between the chips. The largest gap between the chips is $1098 \mu\text{m}$, corresponding to $\sim 27''$ on the sky. The amplitude of our dithers was chosen to be $35''$. The integration time of every individual exposure was 480 sec for the B band and 360 sec for the R band. The total integration time per field amounts to 10800 sec or 3 hours for the R-band imaging and $30 \cdot 480 = 14400$ sec or 4 hours for the B-band imaging. In order to reduce the readout noise, the slow readout mode was used, with a readout time of 48sec. In total 9 observing nights were allocated in April 2007, 2008 and 2009, of which 6 yielded some usable scientific data. A summary of the number of exposures used in making the mosaic images and the atmospheric conditions during the observations is presented in table 2.4. For all those nights, bias frames and sky flatfields in both filters were taken in the beginning and the end of the night. The dark current at the operating temperature of the camera of -153°C is considerably less than $1 e^-/\text{hour}$, and was neglected during the data processing.

2.3.2 Data reduction

The data reduction was done primarily with the *mscred* package in IRAF³. For additional refinements of the world coordinate system (WCS) the Kapteyn package for Python (Terlouw & Vogelaar 2015), and Groningen Image Processing SYstem (GIPSY, van der Hulst et al. 1992) were also used. The photometric calibration of the images was made entirely in GIPSY.

First the overscan was subtracted from every single exposure, and the images were trimmed with the *ccdproc* task. The *biassec* and *trimsec* values used

³IRAF is distributed by the National Optical Astronomy Observatory, which is operated by the Association of Universities for Research in Astronomy (AURA) under cooperative agreement with the National Science Foundation.

date	used exposures	seeing	weather conditions
17.Apr.2007	20	1.0–1.2	cirrus
18.Apr.2007	12	>1.1	clouds
19.Apr.2007	25	1.2–1.4	clear
04.Apr.2008	3	1.2–1.4	clouds
05.Apr.2008	0	-	high humidity
06.Apr.2008	0	-	storm
26.Apr.2009	0	-	high humidity
27.Apr.2009	29	>1.4	cirrus
28.Apr.2009	31	< 1.1	clear

Table 2.4: The exposures used in the final mosaic images, with the dates when they were taken and the atmospheric conditions.

were [2110:2150,4130:4190] and [54:2096,3:4096], respectively. At this point a mask was created, containing all the pixels with contribution from bad pixels and columns. After that a detailed analysis of all the bias frames was made, and a two dimensional master bias frame per observing run was medianly combined with *zerocombine*, and subtracted from all the scientific exposures and the flatfields. The night to night variations in the two dimensional shape of the bias was found negligible.

No fewer than 3 sky-flatfield images were collected in the beginning and the end of every night. After a careful examination and selection, the median of the morning and the evening flats was taken to produce a master flatfield image, one per night and per filter, representing a map of the pixel-to-pixel variations in sensitivity. This was done with *flatcombine*, with *crreject* algorithm, thus creating one master flat field image per observing run. Every master flatfield image, containing 4 individual images- one from every chip, was then normalised to the highest median from all 4 chips. All the scientific exposures were then divided to the corresponding flatfield image. With this step the signature of the detectors was considered removed.

A rough initial coordinate system was written in the headers, as calculated from the pointing of the telescope, and the appropriate rotation was applied to the images, in order to bring them to the standard astronomical orientation. The so made coordinate system was then refined with the *mscpeak* task, from the *mscfinder* package. The task was run in interactive mode, to align the catalog stars in the images with their positions as taken from the NOAO USNO-A2.0 catalog (Monet 1998) by the *mscgetcat* task. A fourth order Chebyshev polynomial was fitted to the catalog positions. The task creates an astrometric solution, which is applied to all the images with the *mscsetwcs* task. The projection used was "tan".

The next step was to subtract the sky from the images. For that an object mask was created, with *objmask*. The task was run three times for every image. Objects with different sizes were selected during every run, and the mask for those objects was grown to a different size, to be able to properly mask out the faint wings of

the galaxies and the scattered light from bright stars. All three masks, created for every image, were then combined with *imexpr*, including the bad pixel masks. A zero order sky was then fitted and subtracted with *mscscopysub*. All the images were then manually examined and if the automatic sky subtraction was found imperfect, the sky level was manually estimated and subtracted.

Because of the long wavelength tail of the Harris R filter, a fringe correction had to be made. The median of all the R band images was used, to create an image of the fringe pattern. This image was then subtracted from the R band images.

All the steps described so far were done chip by chip. The so processed mosaic exposures, free of detector and filter introduced artifacts and sky emission, and containing a proper WCS - tan headers were then reconstructed into a single image using the *mscimage* task. All the exposures, that were to contribute to one of the two final mosaic images were resampled to a common reference WCS so they can be registered with integer pixel shifts (the two band images of every field are treated here as one). A 2-D sinc interpolation was used for the data and a linear one for the masks, containing the bad pixels and the data free areas of the image. Prior to the reprojection all the bad pixels had to be set to zero. All the reprojected mosaic images were then run through the *mscsmatch* task, for additional refinement of the coordinate system and further remove any astrometric errors caused by atmospheric refraction and any translational and rotational uncertainties. The positions of the objects in the images were again matched against the USNO-A2.0 catalog positions. The achieved rms of the positional residuals, with fitting fourth order polynomial is $\lesssim 0.4''$.

The produced in this way 120 individual exposures were then scaled, in preparation for the final stacking. This was done with the IRAF task *mscimatch*. First the exposures were divided into groups of 5 that were to form every individual of the six pointings, that make the entire final mosaic image. Then a catalog with the positions of stars within the overlapping regions between every individual group of 5 exposures was made with *mscgetcat* from the USNO-A2.0 catalog. The task determines the mean value within a box around those coordinates, and in a larger square region around the box. A linear fit between the values for a reference image and a target image is computed. Only the multiplicative scale factor to match the intensities of the target image to the reference image was determined from the task, as the sky was already subtracted and the zero point was considered stable. *Mscismatch* was run interactively for every group of five exposures, and their relative scales were determined. *Mscistack* was then used to produce every one of the 24 pointings, applying the previously calculated scales. A new catalog of stars were made, covering the regions with overlaps between the pointing, and a new pointing to pointing scales were then determined with *mscimatch*. Pointings 1 and 3 were scaled relative to pointing 2. Pointings 4 and 6 were scaled relative to pointing 5, and pointing 5 was scaled to match the flux of pointing 2. The initially estimated scales for every individual exposure were then multiplied by the scales of the pointing they belong to. During the final stacking all 30 exposures participate in the final mosaic image with scales which are product of their individual exposure scale coefficient and the scale coefficient of the pointing they belong to.

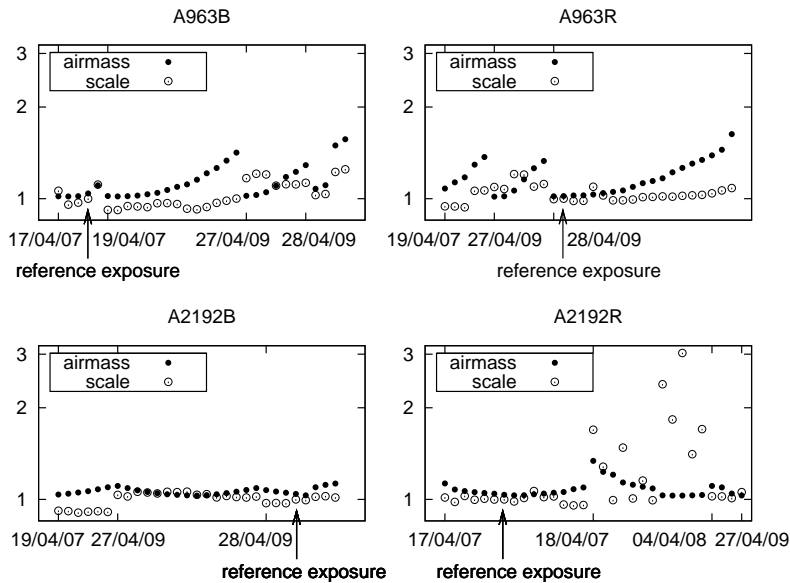


Figure 2.36: The scales for all the exposures used for the four mosaic images with the airmass at which they were taken. The horizontal axis shows the date at which the exposures were made. The position of the exposure used as a reference for the flux scaling is marked by an arrow.

Effectively this scales all the exposures for a given image relative to one chosen exposure, taken at a good conditions and close to the center of the final mosaic. The scales for each exposure are plotted in Fig. 2.36, together with the airmass at which the exposures are acquired. The fact that the scales do not follow the trend of the airmass reflects the lack of photometric conditions during all three observing runs.

The final stacking of all 30 exposures into one mosaic image, covering the entire one square degree field was done with the task *mscstack*. This is a routine, that registers all the pixels on the fly, with integer shifts based on the WCS of the images, while ignoring the pixels described in the masks produced by *mscim-age*. A median combine operation without any rejection algorithm was found to produce the best images, relatively free of cosmic ray events and satellite trails.

2.3.3 Astrometric calibration

The astrometric solutions found for every individual exposure by the *mscsmatch* and written in the headers were applied to the pixel data with the Kapteyn package for Python, prior to the final stacking with *mscstack*. This step was found necessary, after the unsatisfactory results from the on-the-fly registration done

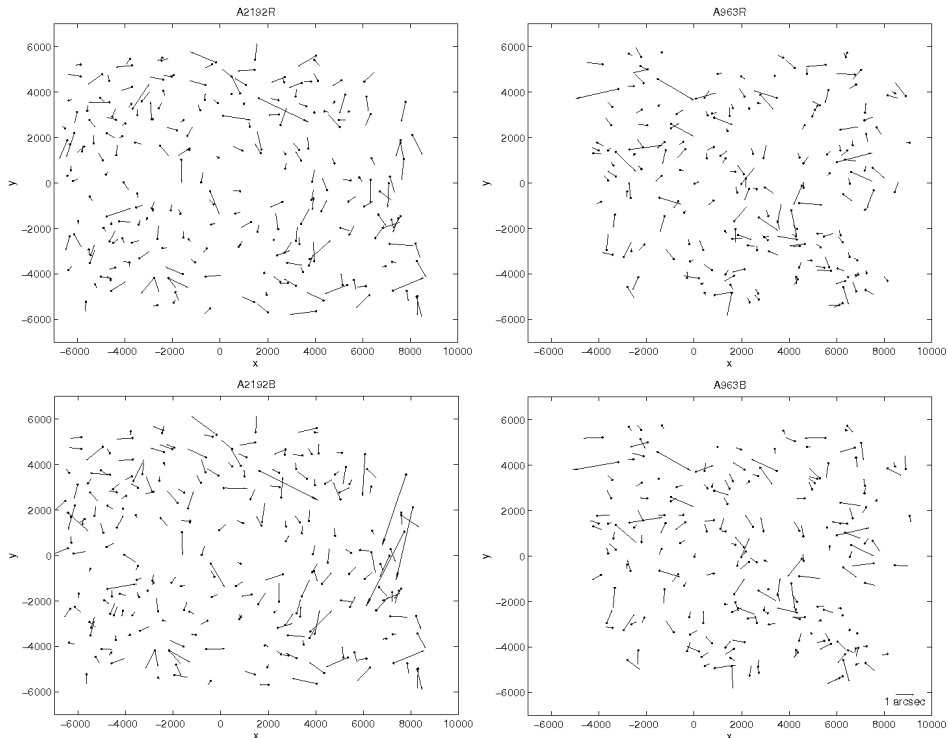


Figure 2.37: Vectors showing the difference (enlarged 250 times) in the positions of stars between our INT imaging and USNO-A2.0 catalog, after the final astrometric calibration. The size of one arcsecond is shown in the bottom right corner.

by *mscstack*, which was introducing mismatch between the individual exposures. The images produced in this way were then read into GIPSY for additional refinement of the astrometry and for photometric calibration. First the images were reprojected, to have a common projection center with the H I maps produced by WSRT of the same fields (see Section 2.2). Then the accurate sky coordinates of ~ 150 stars per field were taken from the USNO-A2.0 catalog and their pixel coordinates were measured. After that the GIPSY task *astrom* was used to measure the deviations of the image positions from those in the catalog. The task creates a “classical” header, and was run with the reference pixels as fixed parameters (CRPIXX, CRPIXY), and the reference sky position, rotation angle and the pixel scale (CRVALX, CRVALY, CROTA, CDELTX, CDELTY) as free parameters. The calculated corrections were applied with *reproj* and the residual deviations are shown in Fig. 2.37. The figure shows the direction and the size of the residuals in the astrometry for all four images, at the position of the ~ 150 stars used for the final astrometric calibration. The length of all the vectors shows the residuals greatly enlarged (250 times) for clarity. In the bottom right corner the size of one arcsecond also enlarged 250 times is shown.

Fig. 2.38 shows the distribution of the astrometric residuals of objects taken from our images and from USNO-A2.0 catalog in RA and Dec. The graphs con-

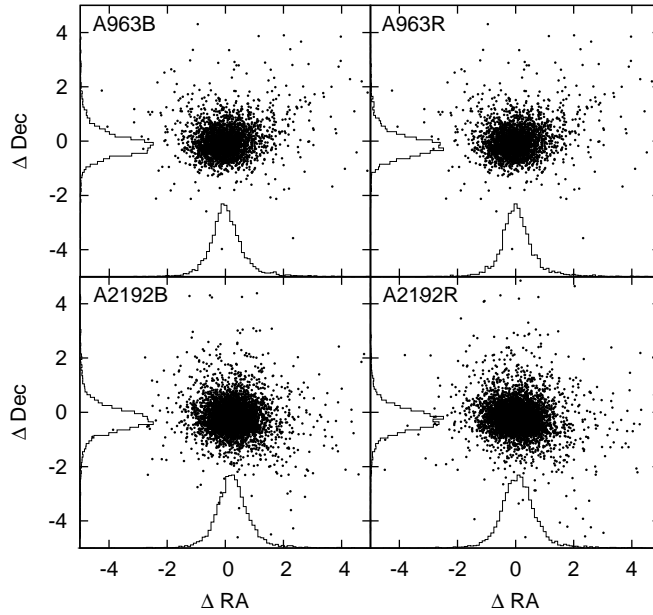


Figure 2.38: The distribution of the difference between the coordinates in our imaging and USNO-A2.0. The axes show offset in arc seconds.

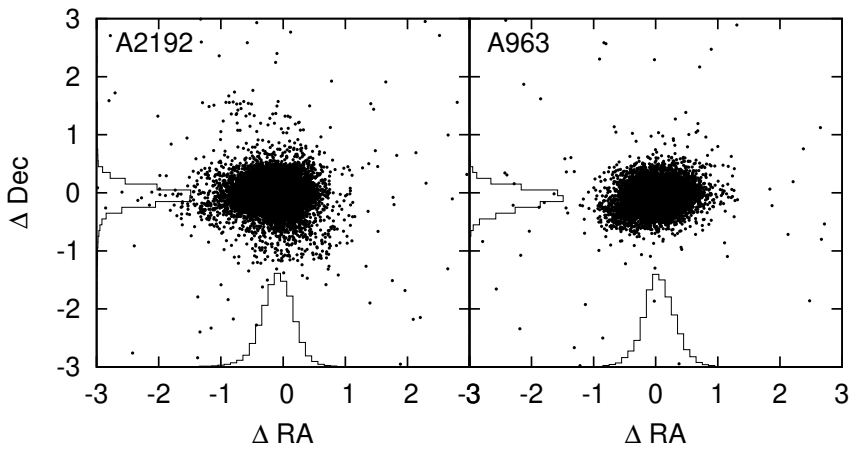


Figure 2.39: The distribution of the difference between the positions of sources in the red and the blue images of the two fields.

tain ~ 5000 objects per image, extracted with Source Extractor (SExtractor Bertin & Arnouts 1996) as explained in the next section. The histograms show the relative distribution of the residuals in both directions. The largest standard deviation of the histograms is $0.7976''$ and the mean is well within one pixel from zero ($1\text{pix} = 0.333''$). Over all, the astrometry residuals are $\lesssim 0.8''$ (1σ) in any direction. These residuals also include the uncertainties of the USNO-A2.0 positions ($\sim 0.25''$), as well as the proper motions of all the objects, which should have significant contribution to the width of the distribution of the residuals even though we avoided stars with high proper motions. Fig. 2.39 shows the internal accuracy of the astrometry, inferred by matching the coordinates of ~ 15000 sources, extracted with SExtractor from the B and the R image of both fields. The residuals are $< 0.41''$ (1σ) in any direction.

2.3.4 Photometric calibration

The photometric calibration of the images was based on SDSS photometry of semi-randomly selected stars. We extracted a catalog with the psf magnitudes (psfMag) of stars from SDSS. The only limitations of the stars were, to have a r-band magnitude above 17.66 mag., as a star brighter than this magnitude would have a peak flux of $\sim 50,000$ ADU in a single raw exposure from our INT imaging, taken at the best possible conditions, in terms of airmass and seeing. This criteria would keep us well within the linear regime of the WFC's CCDs. Additional limitations of stars no fainter than $r = 19.66$ was enforced, to ensure enough signal to noise and of stars spanning a range of colours $0 < g-r < 3$, to allow for a more complete estimation of the colour dependence of the zero point. The so defined search in the SDSS database for a point sources within our two - one square degree fields yielded ~ 900 sources per field.

The SDSS psf magnitudes are based on a model of the point spread function fitted to the object with an additional aperture correction estimated from an image of a bright star, to account for the weak wings of the stellar profile. Those are claimed to be the optimal measure of a given star's brightness. Those SDSS ugriz magnitudes were then converted to the Johnson B and Kron-Cousin R magnitudes, following the transformation equations derived by Lupton (2005) by matching the SDSS DR4 to published photometry for standard stars (Stetson 2000).

$$B = u - 0.8116 * (u - g) + 0.1313; \quad \sigma = 0.0095 \quad (2.3)$$

$$R = r - 0.2936 * (r - i) - 0.1439; \quad \sigma = 0.0072 \quad (2.4)$$

An additional conversion from Harris to Johnson and Kron-Cousin filters is not necessary, as it is thought that the transmission curves of the Harris filters, when convolved with the typical CCD response provides a close match to the Johnson B and the Kron-Cousins R bandpass (INT observer's guide). Fig. 2.40 shows the transmission curves of the Johnson-Kron-Cousin filters and the SDSS filters.

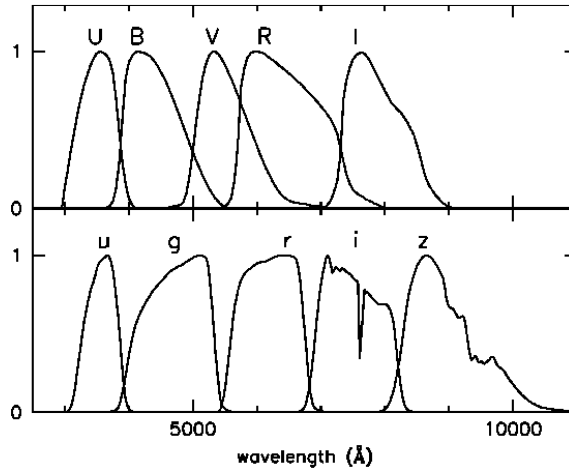


Figure 2.40: The filter transmission curves of the Johnson-Kron-Cousin system (top), and the SDSS filters.

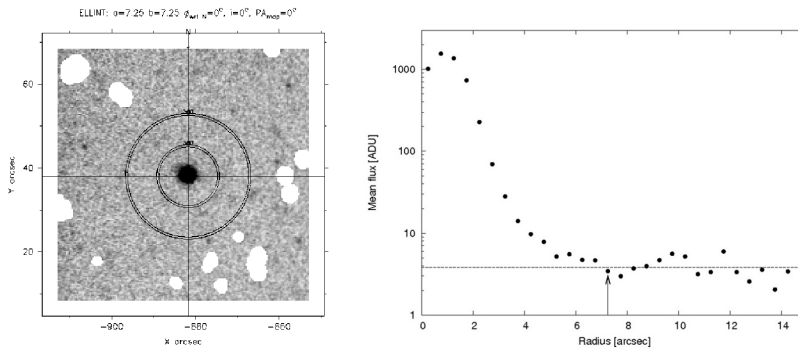


Figure 2.41: Example of the aperture photometry used for the photometric calibration. On the left is the image of the star with all other sources masked out. The inner aperture encircles the flux added to the star, the part between it and the outer circle is used to estimate the local background. The right plot shows the profile of the star, with the arrow at the position of the inner circle. The dashed line is the local background.

The images of all the stars extracted from SDSS were examined, and stars sitting in a relative isolation and on a uniform background, free of scattered light from nearby bright stars or extended sources, were selected for aperture photometry. The total number of stars on which the photometry calibration was based on was ~ 150 per field.

Prior to the photometry, all other objects around the given star were masked out, and the flux was measured within 30 annuli with a width of $0.5''$ and with increasing radius up to $15''$. A manually selected number of the outermost annuli was used for estimation of the local background, and the measured flux within each annulus was corrected with that value. Figure 2.41 shows an image of one of the stars used for photometric calibration and its flux profile. On the left of the figure is the image of $1' \times 1'$ around the star, with the rest of the sources masked out. Shown are two of the 30 annuli within which the flux was measured. The inner one has a diameter of $7.25''$ and all the flux inside that circle is added to the star after correction for the local background. The local background is the mean of the area between the two circles. On the right hand side of the figure the mean value for a given annulus is plotted against its radius. The vertical arrow marks the size of the star, and the horizontal dashed line is the estimated level of the local background. In this case 3.830 ADU. The so measured fluxes were converted to magnitudes and compared to the published SDSS magnitudes to calculate the photometric zero point.

2.3.5 Source extraction

The catalog with all the sources found in the two fields was made with SExtractor. The program was run in dual mode, with the R-band image as a detection image. The images were filtered with a Gaussian with $\text{FWHM} = 2.5$ pixels. The sources were selected to have at least five contiguous pixels ($\text{DETECT_MINAREA} = 5$) with a flux 2σ above the local background ($\text{DETECT_THRESH} = 2.0$). The deblending parameter DEBLEND_MINCONT was set to 0, as this was found to give the best results for the cluster members at $z = 0.2$ we were aiming for. At our seeing level those galaxies rarely show any structures that will cause SExtractor to shred them. In the same time no other deblending setup was able to separate all the galaxies in the crowded central region of Abell 963. The global background was estimated and subtracted with a mesh size of (BACK_SIZE) of 128 and with median filtering with the size of 9 pixels (BACK_FILTERSIZE). This way the extended halos around the very bright stars was removed. This elevated background was causing an erroneous estimation of the Kron radius, hence unreasonably big apertures for the photometry of nearby sources. In addition, the extended light from the cD galaxy in the center of A963 was causing similar errors in the aperture photometry for the very important galaxies in the center of the cluster. The cD galaxy was modeled with GALFIT (Peng et al. 2002) and subtracted, to allow for a better estimation of the Kron radius of the surrounding galaxies. Fig. 2.42 shows the automatic apertures in the center of A963, before (middle panel) and after (right panel) subtracting the model of the light distribution of the cD

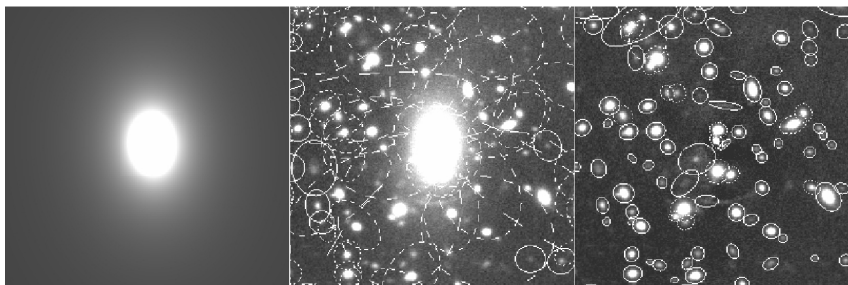


Figure 2.42: The model of the cD galaxy(left), and the SExtractor "apertures" check image before(middle) and after(right) subtracting the model for the cD galaxy

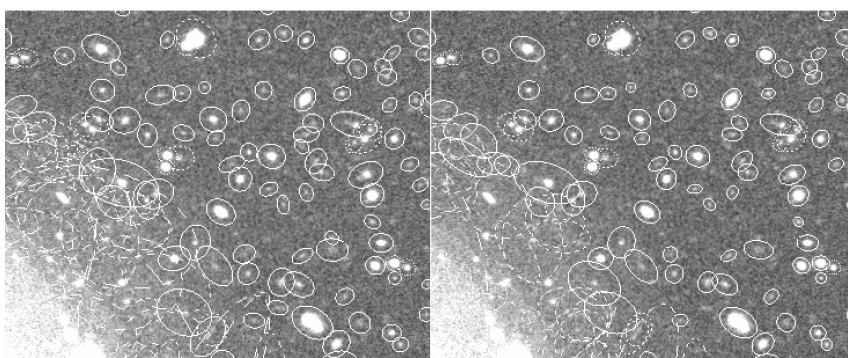


Figure 2.43: The automatic apertures, estimated by SExtractor, before (left) and after (right) subtracting the global background.

galaxy (left panel). The automatic apertures for individual galaxies are following more closely their light distribution in the latter case, but also the deblending of adjacent sources is improved significantly. The magnitude of the cD galaxy were taken from the GALFIT model.

Fig. 2.43 shows the automatic apertures in a region adjacent to a bright star, before (left) and after (right) subtracting the global background, containing the halos around the bright stars. The net effect of this extra step is to reduce the area where bright stars are affecting the automatic photometry performed by SExtractor. The unrealistically large apertures affect sources out to a few arcminutes away from the brightest stars. Obviously there are still regions, very close to the bright stars, where the apertures are too large, causing a systematic offset of the measured magnitudes. Those are much smaller than before, and were flagged in the final catalog. For all the objects in the catalog the flux was estimated in an automatic apertures (MAG_AUTO), with sizes determined by "PHOT_AUTOPARAMS 2.5, 3.5" .



Figure 2.44: The centre of the A963 as imaged by SDSS (left) and by the INT observations presented here (right).

2.4 Additional data

As a comparison sample we use data from the Arizona Cluster Redshift Survey (ACReS, Haines et al. 2013). This survey combines spectroscopic data of galaxies in 30 clusters with $0.15 < z < 0.3$, drawn from the Local Cluster Substructure Survey (LoCuSS, Smith et al. 2010) sample. ACReS uses the same instrument (Hectospec), and the same instrument setup as the MMT survey of A520 (sect.2.1). ACReS target selection is based on J and K bands near-infrared imaging done with the United Kingdom Infrared Telescope and Mayall telescope at Kitt Peak National Observatory. Thanks to its target selection, which very efficiently removes foreground and background objects, ACReS is highly complete for cluster member galaxies. This is shown in Haines et al. (2013). In addition to the MMT observations, ACReS includes a number of cluster member galaxies with previously published redshifts. We use this combined data set to calculate global cluster parameters and cluster membership of the comparison sample.

In addition we also use the data from a multi-fibre spectroscopy observations of galaxies in the field of A963 and A2192 with William Herschel Telescope at La Palma, presented in details in Paper III and used extensively in the analysis presented in Paper II.

3

Results and Discussion

3.1 Analysis of A520

WHEN analysing the population of galaxies in clusters, as measured by observations of individual galaxies, as is the case with the here discussed data, it is very important to assess correctly the completeness of the survey. This is presented in details in Paper I and we will not repeat it here. Instead we will concentrate here on the results from the survey (Sect. 2.1) and discuss what the implications of these results are in combination with the results from the H I survey of A963 and A2192 presented in Section 3.2.

For this part of the analysis we use two data sets - the MMT data, presented in Section 2.1 and the full data set which includes the MMT data and the data from Girardi et al. (2008) (G08). Imaging, and hence colour and stellar mass, and redshifts are available for the full data set, while spectral information is available only for the MMT data set.

Throughout this chapter we use data from the ACRoS survey as a comparison sample presented in details in Paper I and in Section 2.4.

3.1.1 Spectral classification

We split galaxies into passive and star forming based on the absence/presence of emission lines in their spectra. Fig. 3.2 demonstrates the three spectral classes in which we split our galaxies. The Figure shows the strength of the 4000 Å break plotted as a function of a galaxy's stellar mass. The average $D_n(4000)$ for the star forming galaxies in the comparison sample is shown with the thick blue line and the standard deviation with the blue shaded region. The red line and shaded region show the same for the passive galaxies in the comparison sample. The individual symbols show the individual galaxies in A520, red circles for passive and blue stars for star forming galaxies. In every mass bin, the passive galaxies that have $D_n(4000)$ lower than the average for the star forming galaxies are marked with green diamonds. These galaxies constitute our sample of recently quenched galaxies.

On Fig. 3.3 we show one spectrum, representing each spectral class. For the recently quenched galaxies (middle panel), the plotted spectrum is a sum of the spectra of all 12 such galaxies found in A520. The top and bottom panels show

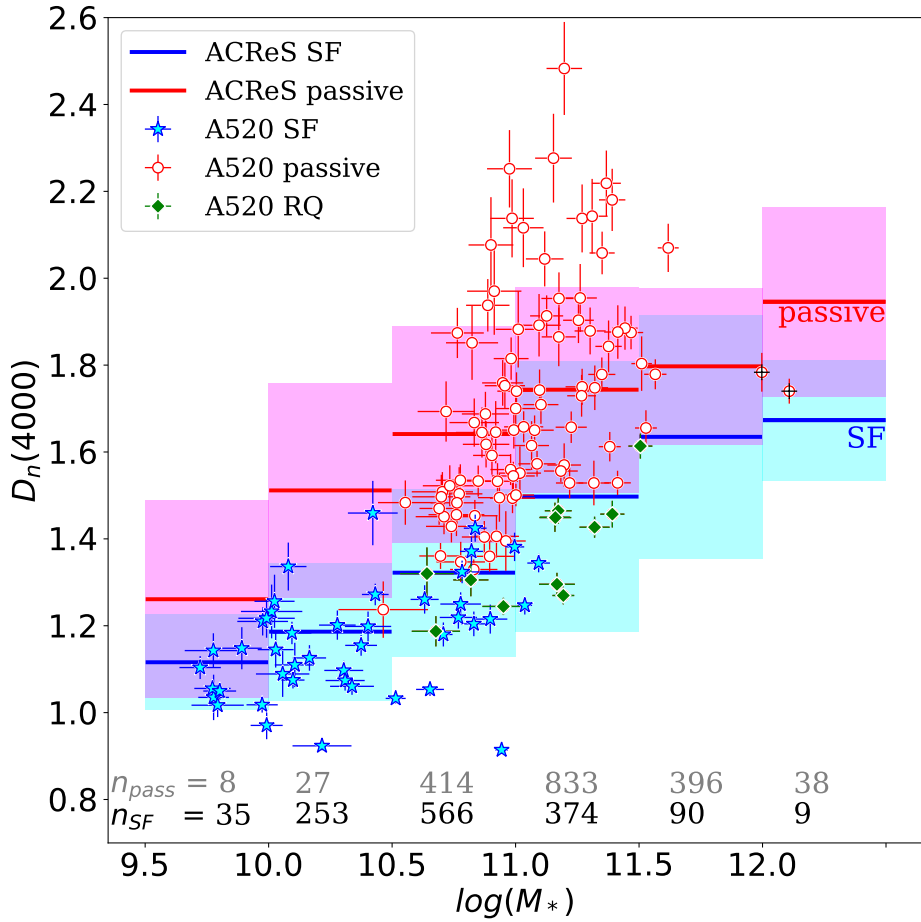


Figure 3.2: Strength of the 4000 Å break per stellar mass. Three spectral classes of A520 cluster-members are shown, passive (red circles), star forming (blue stars), and recently quenched (green diamonds). The average relation for passive and star forming galaxies in the comparison sample is shown with blue and red lines and shaded regions, respectively. The number of passive and star forming galaxies from the comparison sample in each mass bin is written at the bottom of the Figure. The Figure is a reprint from Paper I.

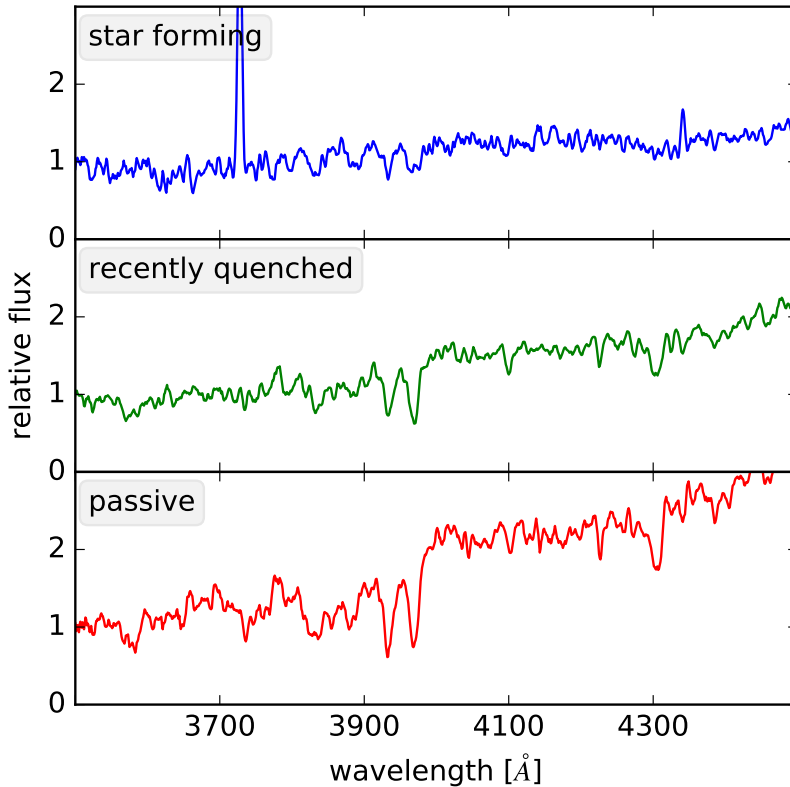


Figure 3.3: Example of spectra representative for the three spectral classes - star forming, recently quenched and passive, from top to bottom. The spectrum in the middle is a stack of all 12 recently quenched galaxies found in A520, the top and bottom ones are a stack of 12 randomly selected star forming and passive galaxies, respectively. The Figure is a reprint from Paper I.

a sum of 12 spectra randomly chosen from the star forming and passive A520 members, respectively. The spectrum of the star forming galaxies has a strong [O II] 3727 Å line in emission. Although both the middle and bottom panels show the 4000 Å break, it is noticeably stronger in the bottom one. The different relative depth of the H + H ϵ and K absorption lines of ionised calcium are also noticeable and indicative of the age of the stellar populations.

3.1.2 Substructure

Fig. 3.4 shows the distribution of the measured redshifts from the MMT survey presented in Section 2.1 and from Girardi et al. (2008)(G08). Exactly 700 redshifts are plotted: 407 from the MMT survey and 293 from G08. The inset in the Figure shows the concentrations of galaxies associated with cluster A520 in greater detail. Because the merger happens very close to the plane of the sky (G08) there are no two clearly separable peaks in the z distribution. The two cD galaxies however

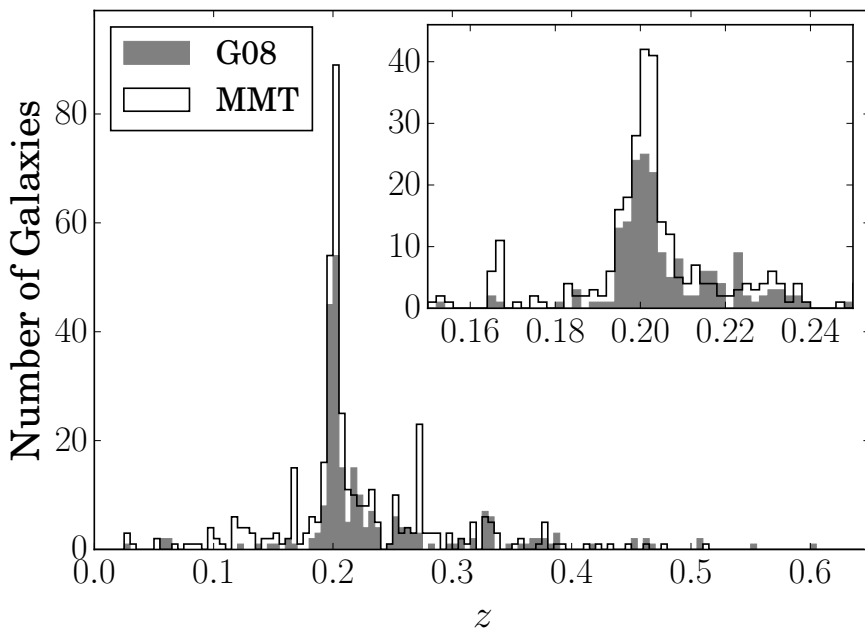


Figure 3.4: The distribution of z from the MMT survey presented in Section 2.1 (black empty histogram) and from Girardi et al. (2008) (filled gray histogram). The inset shows the peak associated with A520 in greater detail. The Figure is a reprint from Paper I.

do show a redshift difference of ~ 0.003 .

Analysing the structure of the cluster A520 as a whole we use the Dressler-Shectman test, as in Section 3.2. The results shown on Fig. 3.5 fully confirm the results from X-ray observations Markevitch et al. (2005); Wang et al. (2016), weak-lensing analyses (Mahdavi et al. 2007; Okabe & Umetsu 2008; Jee et al. 2012, 2014; Clowe et al. 2012; Hoekstra et al. 2015), and G08’s analysis of galaxy population, which show the highly structured distribution of cluster-members demonstrating the recent accretion of sub-clusters. To produce Fig. 3.5 we created a set of 1000 mock catalogues of cluster galaxies with random distributions in z matching that of the confirmed A520 members in terms of mean, standard deviation and total number of galaxies. We then ran the DS test on these and added the calculated deviations of all the galaxies per cluster dividing the sum by the number of galaxies. These averages are plotted with the black line, while the arrow shows the average deviation of A520 member galaxies. The more virialised clusters are expected to show lower average deviation, while clusters with stronger recent accretion of substructures should show higher average deviations. The position of A520 beyond the extreme end of the distribution of mock clusters shows that it is highly unlikely that the picture of A520 can emerge from random sampling of Gaussian data and that this cluster is very likely far from virialised.

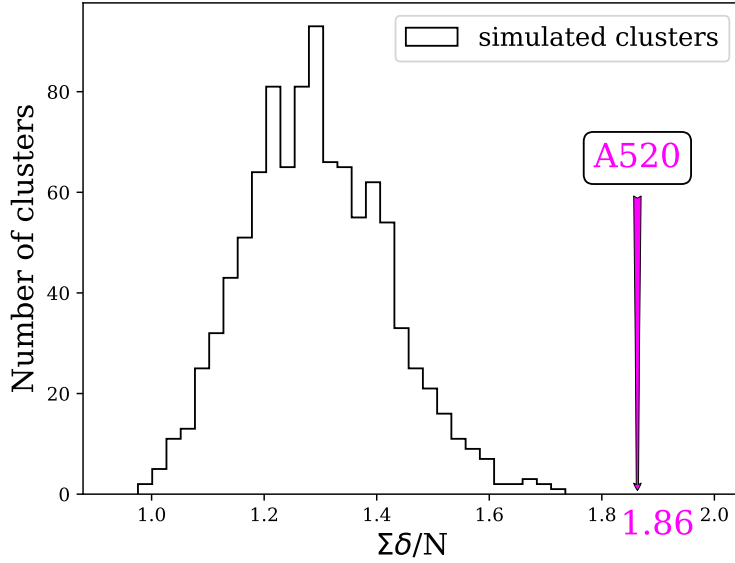


Figure 3.5: Distribution of the average deviation per galaxy from the 1000 separate DS-test runs on mock cluster data (black line) and the average deviation of the 315 members of A520.

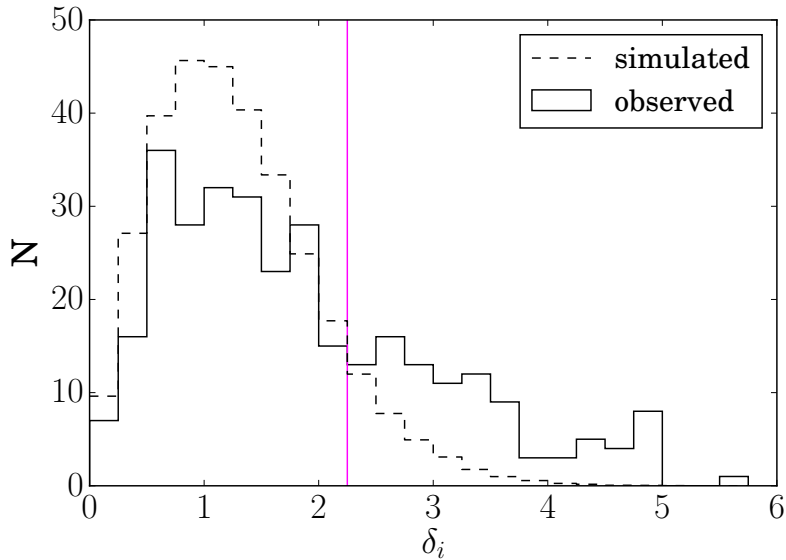


Figure 3.6: The distribution of deviations, calculated with DS test, per galaxy member of A520 (solid line) and all the galaxies from the 1000 Monte-Carlo realisations of cluster data (dashed line). The vertical magenta line shows the value $\delta_i = 2.25$ above which we consider galaxies to be part of a substructure. The Figure is a reprint from Paper I.

Fig. 3.6 shows the distribution of deviations for individual galaxies, members of A520 (black, solid line), and members of the mock clusters catalogues (dashed line), divided by 1000. The deviation above which the distribution of galaxies in the Monte-Carlo clusters drops below that of A520 galaxies is $\delta_i = 2.25$. In the following analysis we select all galaxies with $\delta > 2.25$ as members of a substructure.

Fig. 3.7 shows the distribution on the sky of A520 cluster-members with their deviations encoded in the size and colour of their symbols. Galaxies with $\delta > 2.25$ are shown with magenta circles while the rest with gray circles. The positions of the main mass concentrations from Jee et al. (2014) are annotated. Both P2 and P4 are recovered by the DS test, although the group of magenta circles closest to P2 are somewhat offset from the peak of the black contours showing the mass distribution. The recovery of the central substructures is very sensitive to the choice of central cluster velocity and dispersion. A series of other substructures are also visible, which we have approximately outlined with dotted black lines and named A520i1, i2 and i3. A520i3 likely contains two separate substructures. The one closer to the centre of the cluster is recovered by G08 (the "E" clump on their Fig.11) and by Jee et al. (2014) (clump number 5). The more distant part of A520i3 is outside the area covered by the analysis presented in these two articles. A520i2 is designated "W" by G08. The majority of the galaxies belonging to A520i1 are at $r \gtrsim R_{200}$ and are not covered by G08 nor by any of the weak-lensing analyses. All three substructures outlined in Fig. 3.7 are aligned with the secondary filament proposed by G08 (see also Section 1).

Fig. 3.8 shows the distribution of the cluster-members on the colour – magnitude plots. The galaxies, from both the full data set (empty symbols) and the MMT data set (filled symbols) are split into two bins of cluster centric distance (top and bottom rows) and being inside or outside of a substructure (left and right column). The numbers at the bottom of each panel indicate the total number (n), the number of blue galaxies (n_B) and the number of star forming galaxies (n_{SF}) in the MMT data set and in brackets in the full data set. The comparison of the fractions of blue and star forming galaxies is shown on Fig. 3.9, where the left panel shows the MMT data from which we can derive the fraction of star forming galaxies and the right panel shows the full data set from which we can only derive the fraction of blue galaxies. As expected, the distance to the cluster centre has by far the strongest effect on both the star forming and blue fractions, which are significantly higher outside R_{200} than inside it. The effect of the cluster-centric distance on f_{SF} is stronger for galaxies not belonging to a substructure. The much shallower slope of the solid black line on the left panel of Fig. 3.9 shows that the galaxies belonging to substructures already have reduced f_{SF} outside R_{200} . This is in line with the results of the large body of work on group pre-processing (e.g. Balogh et al. 1999; McGee et al. 2009; Jaffé et al. 2016). Inside R_{200} however, this trend is reversed, with the galaxies with $\delta_i > 2.25$ showing higher f_{SF} than the ones with $\delta_i < 2.25$. This is expected since the substructures indicate recent infall (see also Vijayaraghavan & Ricker 2013), although it suggests that smaller structures harbor higher fractions of star forming galaxies, contrary to the results

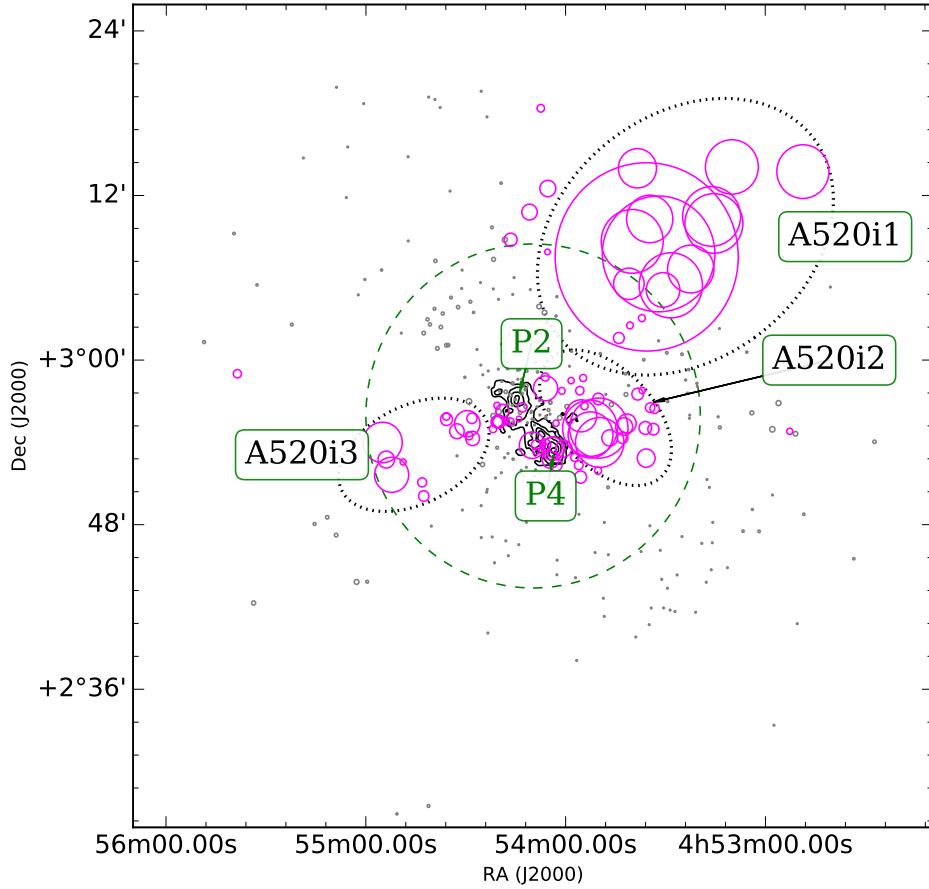


Figure 3.7: Results from the DS test of A520. Each galaxy, member of A520, is represented with a circle with a radius proportional to e^δ . The galaxies with $\delta > 2.25$ are shown in magenta. Separate groups of high δ galaxies are outlined with dotted ellipses and name tags. The green dashed circle has a radius equal to R_{200} of the cluster. The black contours show the mass distribution from Jee et al. (2014). The two main mass concentrations - P2 and P4 are also shown. The Figure is a reprint from Paper I.

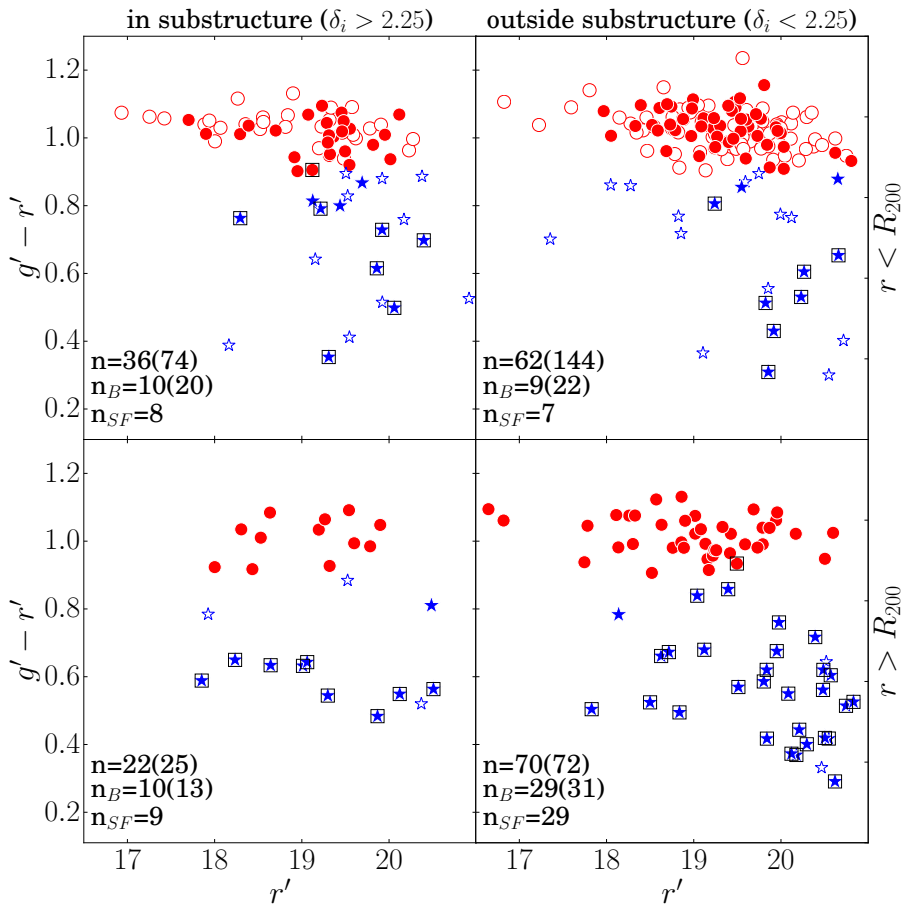


Figure 3.8: Colour magnitude diagrams of all the cluster-members of A520. The four plots present the galaxies in two bins of cluster-centric distance, inside and outside R_{200} (top and bottom row) and in two bins of DS deviations, $\delta > 2.25$ and $\delta \leq 2.25$ (left and right columns). The galaxies from G08 are shown with empty symbols and the ones from the MMT survey with filled ones. The blue and red galaxies are indicated with red circles and blue stars, respectively. Galaxies from the MMT survey with emission lines in their spectra have black squares around their symbols. The total number of galaxies in each panel is indicated for the MMT data set and in brackets for the full data set. Also shown are the number of blue and star forming galaxies. The Figure is a reprint from Paper I.

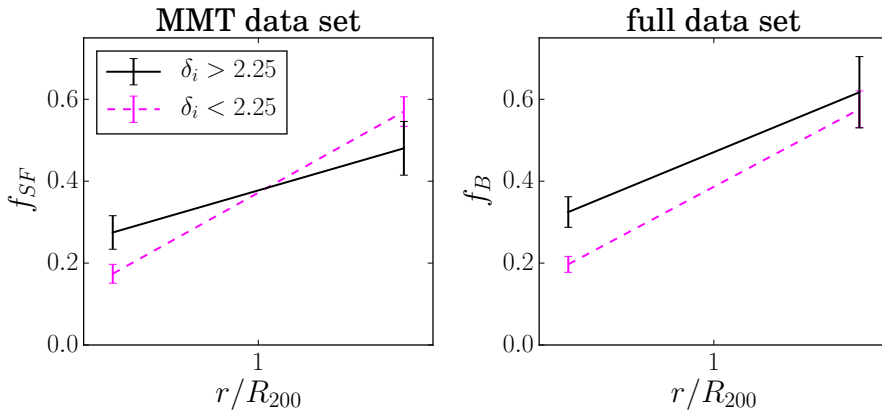


Figure 3.9: The fraction of star forming galaxies (left) and of blue galaxies (right) in A520 as a function of cluster-centric distance. The solid black and magenta dashed lines show the galaxies in and out of substructure, respectively. The points are weighted for completeness. The Figure is a reprint from Paper I.

of Bianconi et al. (2018). This result also implies that galaxies are not instantly quenched once they pass R_{200} , as shown by Haines et al. (2015). The results for the blue fraction f_B , shown in the right panel of Fig. 3.9 paint a similar picture inside R_{200} . Outside R_{200} the substructure does not seem to play a role in determining the colours of the galaxies as both galaxies in and out of substructures show statistically identical f_B . We have validated that these results do not vary significantly with a different cut-off value for δ_i .

In order to assess how the population of galaxies in A520 compares with that of a set of clusters at similar redshift, selected not to be merging, we present on Fig. 3.10(left) the fraction of star forming galaxies as a function of cluster-centric distance normalised to R_{200} of each cluster. f_{SF} of the near field of the clusters is shown with a large empty symbol as the outer-most point. The mean radial trend of f_{SF} in the sample of comparison clusters is shown with thick, dashed, magenta line and $\pm 1\sigma$ of the cluster to cluster variation with the shaded magenta region. The solid, black line shows the same relation for A520. The number of galaxies in each bin (N_{SF} / N_{all}) is indicated on top with magenta for the comparison sample and in black for A520. Both curves are corrected for completeness as explained in Paper I. The selection of the 10 comparison clusters, from the ACRoS survey, is explained in Paper I. In order to assign a timescale to the processes that convert the field population with $\sim 65\%$ star forming fraction to the largely passive cluster population we have over-plotted the lines with different colours, taken from Haines et al. (2015). These lines represent galaxies that are being instantly quenched a certain amount of time after they cross R_{200} for the first time upon accretion. This time delay is indicated by the different colours as shown at the top of the Figure. These lines are based on observations of galaxies infalling into the 75 most massive clusters in Millennium simulation (Springel et al. 2005).

Comparing A520 with the comparison sample it becomes obvious that A520's centre is devoid of star forming galaxies to a much greater extent than the average non-merging cluster at the same $z \simeq 0.2$. The innermost point of the comparison sample shows $f_{SF} = 0.23 \pm 0.08$ while at the same normalised distance A520 has only $f_{SF} = 0.05 \pm 0.02$. Within the comparison sample the 10 clusters cover $0.13 < f_{SF} < 0.42$. None of them are dominated by passive galaxies to the extent to which A520 is. The cluster with the highest fraction of star forming galaxies in the comparison sample is A963, which we analyse in detail in Section 3.2. The difference between A520 and A963 shown on this Figure resembles closely the results of Butcher & Oemler (1984). Comparing the radial trend of f_{SF} for A520 with the lines from the simulations we see that at R_{200} it agrees with the ~ 2 Gyr line (in agreement with Haines et al. (2015) and the comparison sample). Moving closer to the cluster centre, below $\sim R_{500}$, A520's line drops more rapidly than any of the thin lines, suggesting an additional mechanism for quenching. This innermost region is populated by the galaxies that have experienced the high-velocity core passage and the impact with the intra-cluster matter of the other sub-cluster in the merger.

The black dashed and dotted lines on Fig. 3.10 (left) show the fraction of star forming galaxies as a function of cluster-centric distance measured only within the green and blue shaded regions on the right-hand side of the Figure. This panel shows the distribution on the sky of the passive (red circles) and star forming (blue stars) galaxies, members of A520, together with the merger axis and R_{200} radius. This is discussed in greater detail below, in relation to the discussion on Fig. 3.11.

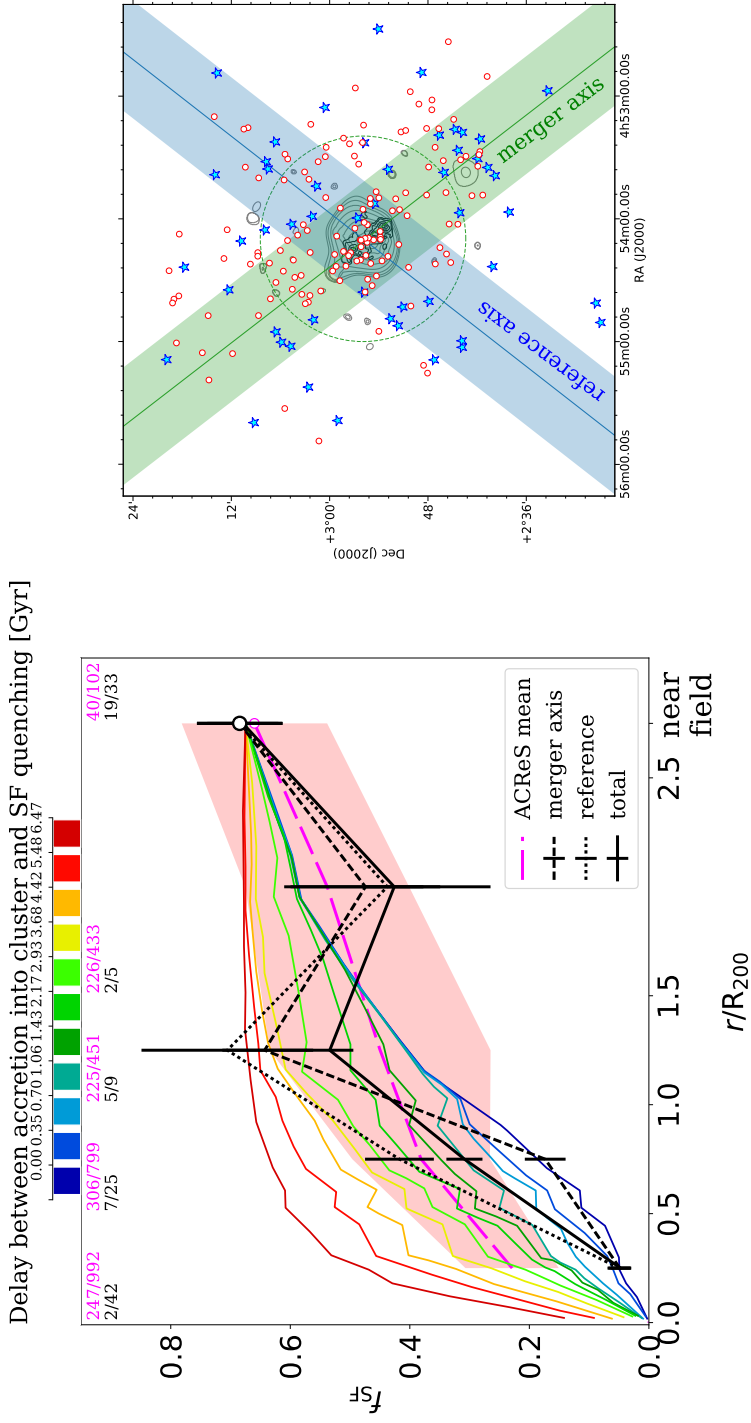


Figure 3.10: *Left* A completeness-corrected fraction of star forming galaxies as a function of cluster-centric distance in A520 (black lines), and in the average comparison cluster (dashed, magenta line). The dotted and dashed black lines show f_{SF} -radius relation along the blue and green stripes on the right panel. The outer most point, indicated with a large circle, shows the fraction of star forming galaxies in the near field region of the clusters. The numbers at the top of each bin show the number of star forming galaxies / number of all galaxies in the bin for the comparison sample in magenta and for A520 in black. The thin lines of different colours show the expected f_{SF} -radius relation from Haines et al. (2015).

Fig. 3.11 shows the distribution of galaxies with different properties on the sky. To describe the cluster we use gray and black contours showing the X-ray emission and the mass concentration (Jee et al. 2014), respectively, as well as the dashed circle, which has a radius equal to R_{200} , the solid, green line, which connects the two biggest mass concentrations, and thus indicates the most probable axis of the merger, and the dotted ellipses, which encompass the substructures recovered by the DS test and X-ray imaging (see also Fig. 3.7). To describe the galaxies, members of A520, we use large symbols: red circles for the passive population, blue stars for the star forming population, large, magenta diamonds for the AGNs, and small, green diamonds for the recently quenched galaxies. The small gray dots show galaxies with available spectroscopic redshifts, that are not members of the cluster. The Figure shows that the majority of the star forming galaxies inside R_{200} are found in substructures. The total number of star forming galaxies in and out of substructures is approximately equal but as a fraction of all the galaxies substructures carry double the star forming fraction - 22% and 11% in and out of substructures respectively (indicated on Fig. 3.8). Another noticeable feature of Fig. 3.11 is that the band surrounding the merger axis is occupied mostly by passive galaxies (green shaded area on the right panel of Fig. 3.10). Along the merger axis there are no star forming galaxies out to R_{200} . Perpendicular to the merger axis, the substructures carry star forming galaxies much closer to the cluster centre (blue shaded area on the right panel of Fig. 3.10). To demonstrate this more clearly we present the right panel on Fig. 3.10 and the associated dashed and dotted lines on the left panel. These lines show the fraction of star forming galaxies calculated over the coloured stripes on the right panel of Fig. 3.10, along the merger axis (green, shaded area and dashed line) and approximately perpendicular to the merger axis (blue, shaded area and dotted line). Along the blue, shaded region the star forming fraction is comparable to that of the comparison clusters and only drops in the central bin. Along the green shaded region f_{SF} is consistently below that out to R_{200} . The central bins are the same, as indicated on the right panel of Fig. 3.10. Note that the largest concentration of star forming galaxies outside R_{200} is within A520XX which lies exactly on the merger axis.

The recently quenched galaxies (RQ), indicated with green diamonds on Fig. 3.11 are also not uniformly distributed on the sky. All of them are found in substructures. The ones with $r < R_{200}$ are all to the west of the cluster center in substructures A520i2 and A520i1. The RQs outside R_{200} are all found in A520XX. This substructure is also unusually rich in star forming galaxies. It also contains the two galaxies with the highest stellar mass in the MMT survey (marked with black crosses on Figures 3.11 and 3.2. We did not target the two cD galaxies near the centre of A520.), which also exhibit an unusually low $D_n(4000)$ index for their stellar mass, indicating possible presence of young stars, although not sufficient to label them as recently quenched.

Fig. 3.12 shows the smoothed, completeness-corrected number densities of member galaxies of A520 and the ten comparison clusters, projected on the sky. The density of passive galaxies is shown as a background image with a loga-

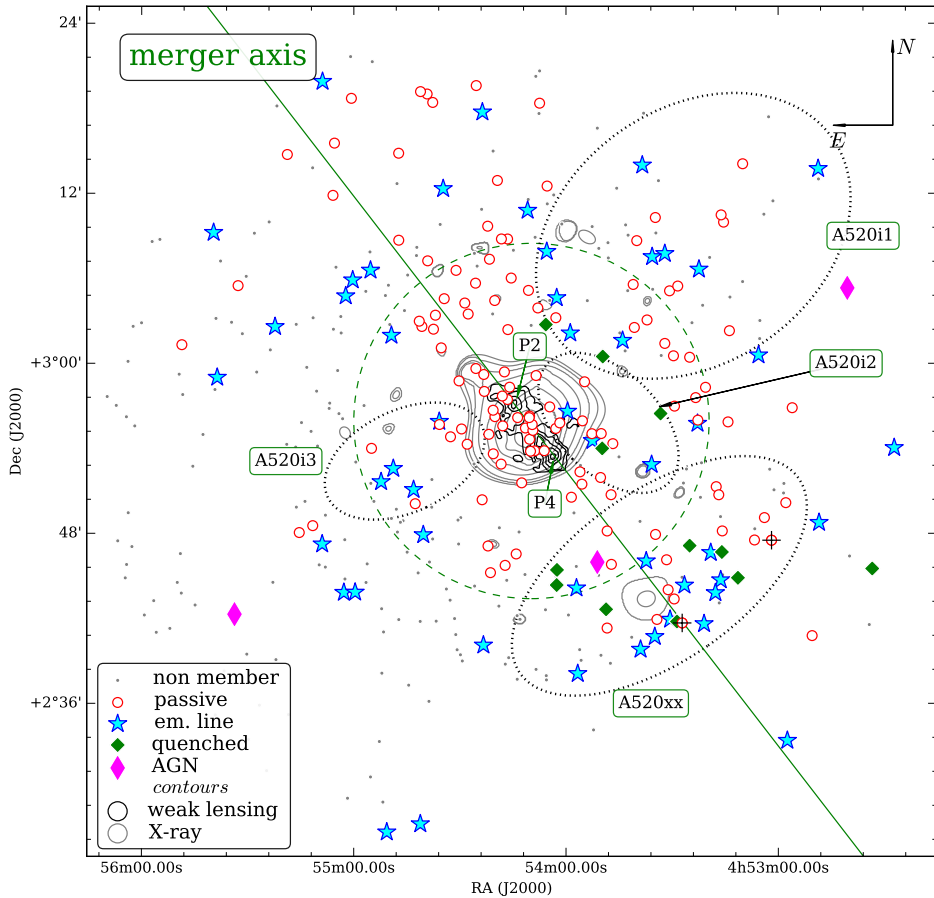


Figure 3.11: Distribution on the sky of the member galaxies of A520 and their properties. The small gray dots represent galaxies with spectra known not to be in the cluster. The blue stars and the red circles are star forming and passive cluster-members. cluster-members with a spectrum with a contribution from AGN are shown with large magenta diamonds and the recently quenched cluster-members are shown with green diamonds. The black contours show a cluster mass map derived from weak-lensing. The gray contours show X-ray emission associated with extended sources. The dotted ellipses with name tags outline the structures found with the DS test and the structure A520XX discussed in details in the text. The green, dashed circle has a radius equal to R_{200} and the solid green line goes through the centres of the two major mass concentrations thus showing approximately the axis along which the merger progresses. The Figure is a re-print from Paper I.

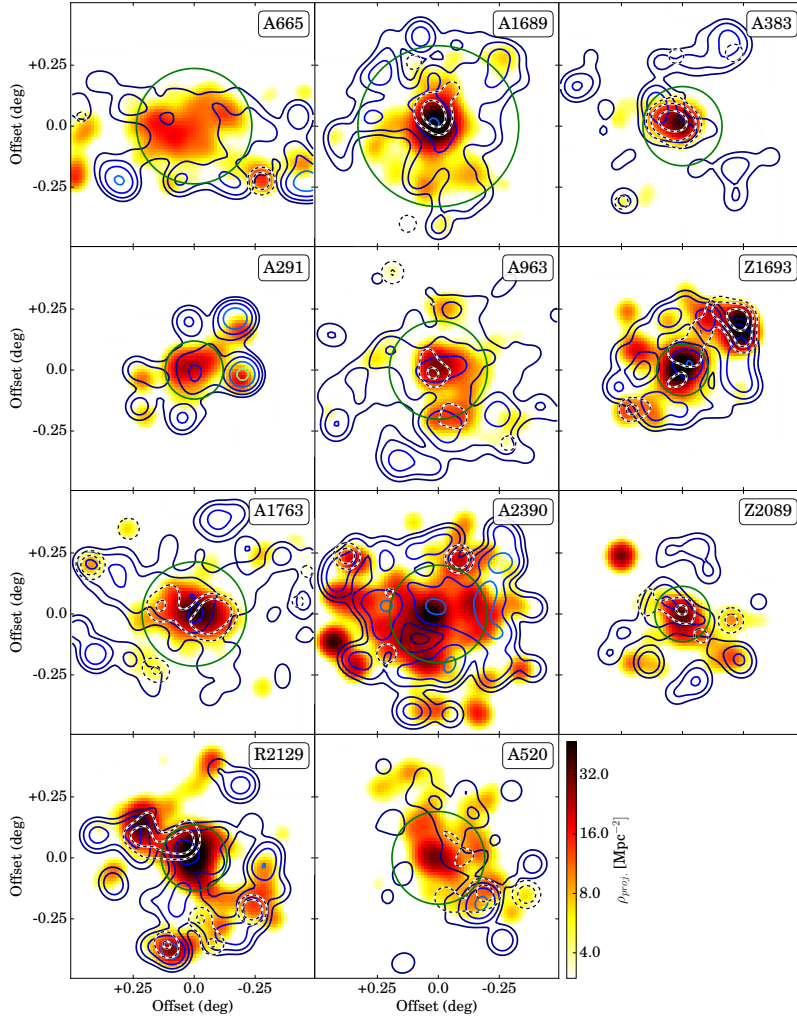


Figure 3.12: Projected number density distribution of cluster-members of different types for A520 and the comparison sample. The name of each cluster is written in the top right corner of the panel. The colour background image with "heat" colour scheme shows the number density distribution of the passive galaxies. The blue contours show the number density of star forming galaxies. The contours are plotted at the levels of the tick marks on the colour bar. The black, dashed contours show the projected number density of recently quenched galaxies. R_{200} of each cluster is indicated with a solid, green circle. The Figure is a re-print from Paper I.

rithmic representation according to the colour bar. The density of star forming galaxies is shown with solid blue contours. The contours are drawn at density levels corresponding to the tick marks on the colour bar. The dashed contours show the smoothed, projected number density of recently quenched galaxies. The green circles have radii equal to R_{200} of the corresponding cluster. All the panels have the standard astronomical orientation, also indicated on Fig. 3.11, north is up and east to the left. The comparison sample is selected to contain clusters for which we couldn't find a reference that claims they are merging. We did a visual inspection of position velocity plots of their member galaxies which also did not reveal any obvious ongoing mergers. It is obvious that despite this selection, all the clusters show a very complex distribution of both passive and star forming galaxies. Often the separate peaks in the passive galaxy distribution are accompanied by a corresponding peak in the density of star forming galaxies. This is expected because, even though the fraction of star forming galaxies goes down towards the centres of all clusters, the overall galaxy density goes up at least an order of magnitude more. This is also an indication that galaxies are not instantly quenched once they cross R_{200} .

Some clusters, like A665 for example, show no well defined peak in the distribution of passive galaxies and an offset concentration of star forming ones. In the case of A520 (last panel) the distribution of passive galaxies is clearly elongated along the merging axis (only shown on Fig. 3.11 which has the same orientation). The associated concentration of star forming galaxies is offset to the right and it has a similar elongation but no well defined peak. The peak associated with A520XX, lying on the R_{200} circle in an approximately 5 o'clock direction does exhibit peaks in the concentration of all three galaxy types. Note that A520XX lies exactly on the merger axis, which presumably coincides with the axis of the filament along which the merging sub-clusters were travelling. The presence of massive galaxies, extended X-ray emission and the relatively high density of galaxies with self-similar distribution is intriguing. It is possible that A520XX represents a large group or a small cluster which is infalling towards the core of A520 for the first time. Note that we have very few targeted galaxies beyond $\sim 1.5 R_{200}$ along the merger axis in this direction. Also the X-ray imaging ends approximately where the extended emission associated with A520XX lies. It is thus reasonable to expect that we are not sampling the entire extent of this substructure. If this is indeed an infalling cluster, its richness of star forming and recently quenched galaxies could be taken as a sign that infalling galaxies, even when embedded in relatively massive structures, can experience a rejuvenation of their star formation activity. A similar conclusion, although for individual galaxies, was reached in Paper II by stacking optical spectra of galaxies in the infall region of A963. The clearly decreased $D_n(4000)$, even in the most massive galaxies (within our sample) of this substructure, is indicative of truly extensive rejuvenation. Further observations are needed to fully analyse this substructure and to assess whether the galaxies infalling as part of large structures are experiencing different effects upon accretion when compared to individual galaxies. Note, that on the opposite side of the cluster core, along the merger axis, the mixture of passive and star

forming galaxies lacks the overall increase in density, as well as the concentration of star forming and recently quenched galaxies.

The lack of star forming galaxies in the core of A520 is intriguing. The author is tempted to speculate that the two main merging cores (P2 and P4 on Fig. 3.11) have experienced a burst of star formation while at distance from each other, much like A520XX. Observed more than 1 Gyr after that, we see no sign of any current or recent star formation in their spectral line indices nor in $D_n(4000)$. We did a test using Bruzual & Charlot (2003) models to estimate the timescale on which $D_n(4000)$ will show the presence of a recent star formation. Even if the star burst builds as much as 15% of the final stellar mass of the galaxy, within 0.5 Gyr $D_n(4000)$ will return back to the expected relation shown on Fig. 3.2. A520 is observed at least 0.2 Gyr after core passage (Paper I and also Girardi et al. (2008)).

In order to further test how self-similar the distributions of passive and star forming galaxies in all the clusters in the comparison sample and in A520 are we use a Modified Hausdorff Distance (MHD). The original Hausdorff distance (Huttenlocher et al. 1993), named after Felix Hausdorff, was designed to measure how far two subsets are from each other and has found extensive application in shape matching. The modification, introduced by Dubuisson & Jain (1994), is designed to make the results less susceptible to outliers, by using the average minimum distance rather than the maximum. In essence MHD gives the average minimum distance between the two data sets:

$$d(X, Y) = \frac{1}{N_X} \sum_{x_i \in X} \min \|x_i - y_i\| \quad (3.1)$$

The test is particularly useful for the purpose of comparing "on-the-sky" distributions of galaxies as the MHD value is found to increase monotonically as the difference between the two sets of points increases (Montes & Trujillo 2019). In our case, the different clusters are sampled at different rates which can bias the MHD values as the more densely sampled clusters will naturally show lower MHD. In addition, the MHD value does correlate well with the density of star forming galaxies. To correct for this we multiply the calculated MHD for each cluster with the square root of the average density in galaxies per Mpc^2 , and in the same way but only taking the density of star forming galaxies into account. The results are shown in Fig. 3.13. The histograms of corrected MHD values for all 30 clusters in the ACREs survey are shown in blue. The distribution of corrected MHD values for the ten comparison clusters, shown also on Fig. 3.12, are shown with the black histograms, with the name of each cluster indicated in its corresponding bin. The left panel shows the MHD values multiplied by the total galaxy density. The right panel shows MHD multiplied by the density of star forming galaxies. When corrected by the total galaxy density, A520 shows a MHD value of 1159 which exceeds that of all ACREs clusters. When removing the dependence of the MHD on the blue fraction, A520 moves closer to the ACREs distribution but still remains close to its the upper extreme, with only A267 showing greater $\text{MHD} \times \Sigma_{SF} = 686.5$. With $\text{MHD} \times \Sigma_{SF} = 641(412)$, A963 is the third(fourth) lowest within the full ACREs sample, when corrected by the total galaxy density (star forming

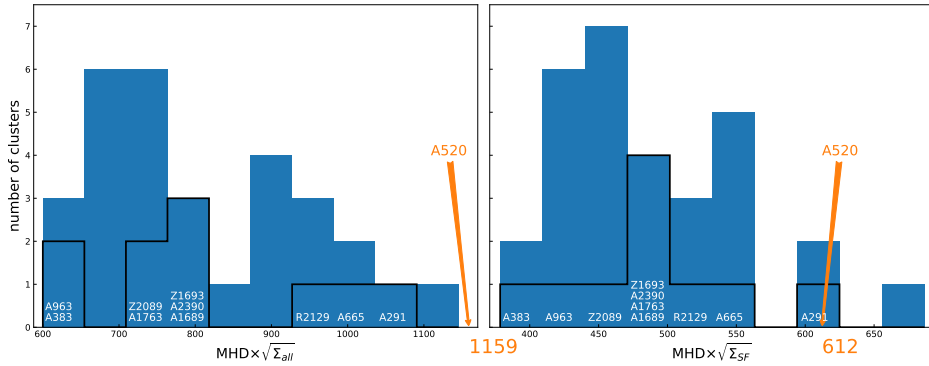


Figure 3.13: Corrected MHD for the full ACRoS sample (blue, filled histogram) and for the comparison sample (black histogram). The name of each cluster from the comparison sample is written in its bin of MHD. The MHD value for A520 is indicated with the arrow. The distribution on the left shows MHD corrected for the overall galaxy density, and on the right corrected for the density of star forming galaxies.

galaxy density). Among the comparison sample, A963 is the second lowest in both cases, with only A383 showing lower MHD. In both cases A520 is higher than the entire comparison sample.

Regarding one of the goals of this work – determining the role of cluster mergers in the evolution of cluster galaxies, we can draw some conclusions based on the evidence presented above. There is little doubt that A520 is a cluster in the process of formation. There is also little doubt that it is more deficient in star forming galaxies than our comparison sample. Observing A520 ~ 0.2 Gyr after the core passage indicates that galaxies participating in a cluster merger have their star formation quenched well before they reach the cluster core. If the onset of environmental effects during a cluster merger is accompanied by an initial burst of star formation that happens at large cluster-centric radii ($>R_{200}$). This view is supported by the lack of star forming galaxies along the merger axis, by the lack of reduced $D_n(4000)$ values around the cluster core, and by the elevated fraction of star forming and recently quenched galaxies belonging to A520XX sub-structure (see Fig. 3.11). We should keep in mind that this conclusion is based on analysis of one cluster only and there is no general consensus in the literature as to what the effect of cluster mergers on their constituent galaxies is (Poggianti et al. 2006; Chung et al. 2009; Stroe et al. 2013, 2014; Cohen et al. 2014; Stroe et al. 2015; Sobral et al. 2015; Stroe et al. 2016). Even considering all the studies referenced above, the number of cluster mergers analysed in detail is small. Combined with the large uncertainties in determining e.g. the presence of a merger, the mass ratio, the age of the merger, its orientation or the presence of substructure in general, this makes our conclusions tentative at best.

However, the recent accretion of a large fraction of the current cluster-members is accompanied by a reduced rather than elevated fraction of star form-

ing galaxies. Our current data can only give us a hint as to whether this is due to pre-processing or rapid quenching at earlier stage of the merger (substructure A520XX). However, the stark contrast between A520 and A963's star forming fractions does indicate that the modes of accretion determine, to some extent, the blue fractions observed by BO84. The spread of all H I detections in A963 to the east of the cluster core, where no large-scale structure filaments or any substructures are observed, indicates that pre-processing is very important in determining the blue fraction of clusters.

The work of Haines et al. (2009) needs to be discussed here as it analysed clusters at similar redshift and using LoCuSS- the parent data set of our comparison sample. Their goal was also to probe the nature of the BO effect and its scatter, and they also checked if the fraction of star forming galaxies correlated with the recent merging history of the clusters as measured by the offset between the BCG and the peak of the X-ray emission. They concluded that there is no correlation, although their Figure 6 shows that there are no clusters with a high star forming fraction among recent mergers (high separation). Thus our result is consistent with their finding.

Note, that analysing clusters in projected phase-space can actually obscure information about the different nature of the galaxies accreted along filaments and otherwise. Simply assuming that cluster-centric distance is all that defines galaxy properties also assumes spherical symmetry of the cluster and isotropic accretion. None of these are necessarily true for all clusters. A large fraction of the galaxies fall onto clusters along filaments, but probably an even larger fraction of all groups, where pre-processing can take place, are accreted along filaments (Sarron et al. 2019). As stated earlier, and in Chapter 4, while projected phase-space analysis can teach us a lot, a full observed phase-space analysis is needed to get as close as possible to the full picture of the coevolution of galaxies and their host clusters.

3.2 Analysis of A963

3.2.1 Dynamical analysis

THE cluster-membership assignment used for the analysis of A963 and A520 is explained in detail in Papers I, II and III. While there are subtle variations in the approaches taken, the differences are cosmetic and unlikely to drive any of the conclusions presented in this and the next chapters. Paper III reveals that A963 represents a conglomerate of at least three clusters accompanied by smaller substructure. In this Section (as in Paper II) we concentrate on the main cluster A963_1, which we will, for brevity, refer to as A963.

In order to discover any substructure within the galaxy distribution we employ two different techniques. The first one is looking at X-ray observations for any extended emission associated with a galaxy concentration on the sky. With this technique we discovered three substructures within A963, probably representing infalling groups (Haines et al. 2018). The same method was applied to A520 where it resulted in the mapping of one substructure (A520XX, Paper I) discussed in Section 3.1.2. The second method for discovering substructure in clusters employed here is the widely used Dressler-Shectman test (Dressler & Shectman 1988). The test takes every galaxy and its N nearest projected neighbors, calculates their central velocity and velocity dispersion and compares this to the cluster's central velocity and total velocity dispersion to get a deviation (δ), according to the formula:

$$\delta^2 = [(N + 1)/\sigma^2][(\bar{v}_{\text{local}} - \bar{v})^2 + (\sigma_{\text{local}} - \sigma)^2]. \quad (3.2)$$

Where \bar{v} and σ are the central velocity and velocity dispersion of the cluster as a whole, and the subscript *local* indicates the values for the group of $N+1$ galaxies.

This test uncovered four substructures in A963 and three in A520. Curiously while both methods (X-ray and DS test) show that both A963 and A520 are not completely virialised and show some amount of substructure, the individual substructures do not, in general, overlap, i.e. the two methods show different substructures.

The distribution of substructures within A963 seems to indicate a preferred direction (North – South) along which the substructures are distributed, with an additional extension to the west. In order to map the large scale structure around A963 on Figures 3.15 and 3.16 we plot the distribution on the sky and z of all the galaxies with available spectroscopic data from SDSS. Note that at those redshifts SDSS is not complete and only samples the most massive, usually red, galaxies residing at the tip of the local red sequence. This incompleteness was the reason for our spectroscopic campaign with the William Herschel Telescope (WHT) presented in Papers II and III and in Section 2.4. However, SDSS have the advantage of very extended sky coverage around A963 which is useful for mapping the large-scale structure (Joeveer & Einasto 1978). Fig. 3.15 does show extended over-density of galaxies to the northeast and southeast of the cluster stretching through the $\sim 9^\circ$ covered by the Figure and being approximately aligned with the distribution of substructure within the cluster. The Figure also shows a more loose

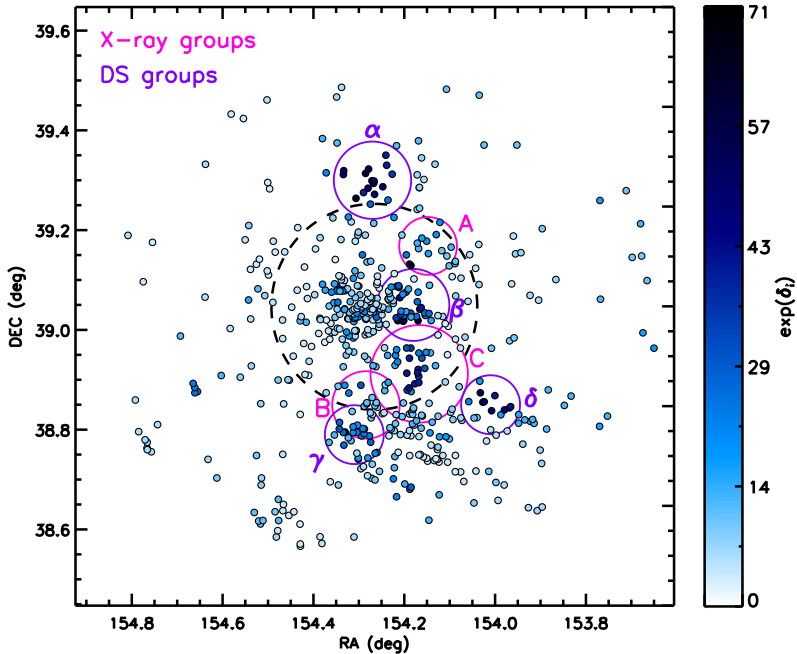


Figure 3.14: The distribution on the sky of all spectroscopically confirmed members of the main cluster in A963. The DS test results for this cluster are colour coded with the darker colours indicating larger deviations, according to the colour bar. Separate substructures found with the DS test are outlined with blue circles. The magenta circles indicate substructures found by their extended X-ray emission. The dashed circle has a radius equal to R_{200} of A963. The Figure is a reprint from Paper II.

over-density of galaxies to the west of the cluster, approximately aligned with the direction indicated by the westerly extension of the distribution of substructures within the cluster. Fig. 3.16 shows the velocity distribution of the galaxies within these three structures and A963 cluster-members. Indeed these structures show a relatively narrow velocity dispersion at all cluster-centric distances and their overall appearance on this projected phase-space plot is very similar to the filaments found around Virgo (Lee et al. 2015) and Coma (Falco et al. 2014).

In order to examine more closely the distribution within A963 and its substructure of galaxies with different star formation properties and gas content we present Figures 3.17 and 3.18. The first one is very similar to Fig. 3.14 but with added information. The galaxies are colour coded according to their NUV-R colours. Those with $2.5 < \text{NUV-R} < 4.0$ and $\text{NUV-R} < 2.5$ are shown in light and dark blue, respectively. The passive galaxies with $\text{NUV-R} > 4.0$ are shown with red diamonds. The larger symbols indicate greater total luminosity. Galaxies

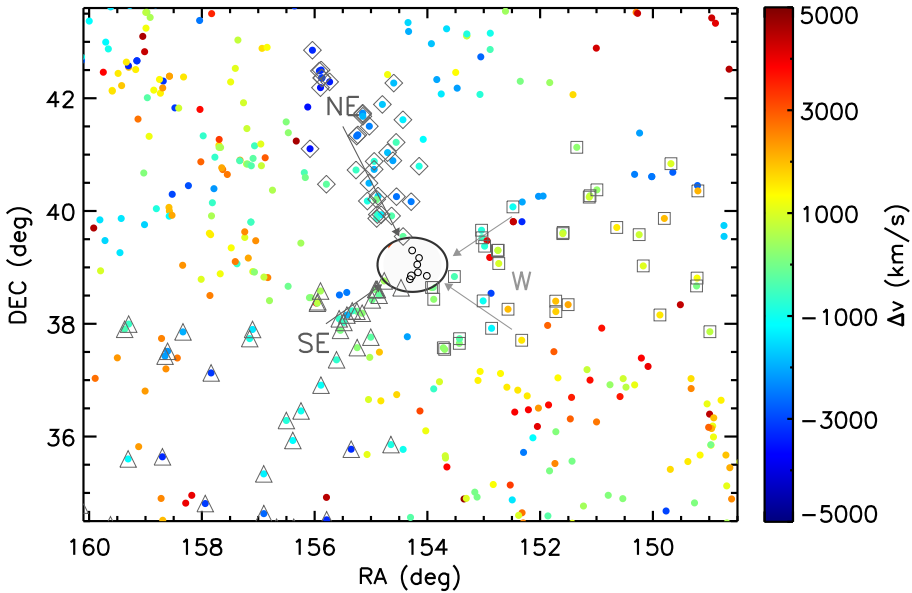


Figure 3.15: The large scale structure around A963 as mapped by SDSS spectroscopic targets. The large black circle has a radius equal to $3 \times R_{200}$ of the cluster (~ 5.8 Mpc at $z = 0.2$). The small circles inside it mark the DS and X-ray substructures indicated on Fig. 3.14. The points outside $3 \times R_{200}$ of the cluster have a redshift range of 0.184–0.224. The Figure covers $\sim 9^\circ \times 9^\circ$ on the sky. The separate points are colour coded according to their peculiar velocity with respect to the centre of A963. The diamonds, squares and triangles show galaxies outlining the three possible filaments along which galaxies, and larger structures, are being delivered to the cluster. The Figure is a reprint from Paper II.

detected at 21 cm have gray boxes drawn around their coloured symbols. A few things are immediately obvious; not only are the passive galaxies strongly clustered towards the cluster centre but also the regions occupied by the substructures show stronger prevalence of passive galaxies. A notable exception is the DS group δ which is dominated by blue galaxies. To the east of the cluster, where no substructures have been detected, there is a relative lack of passive galaxies. Looking at the distribution of the HI detected galaxies a similar picture emerges. There are very few detections inside R_{200} of the cluster and within the groups, with the exception of δ and the X-ray group A, which is also relatively rich in blue galaxies. The majority of the HI detections are found to the east of the cluster centre and span the entire N-S extent of the Figure, with the apparent decrease in their density away from the cluster likely due to primary beam attenuation. Note that at similar cluster-centric distances to the west there is a lack of HI detections.

Fig. 3.18 allows us to take a closer look at the possible reasons behind the observed galaxy distribution in this cluster. A few separate regions are outlined in-

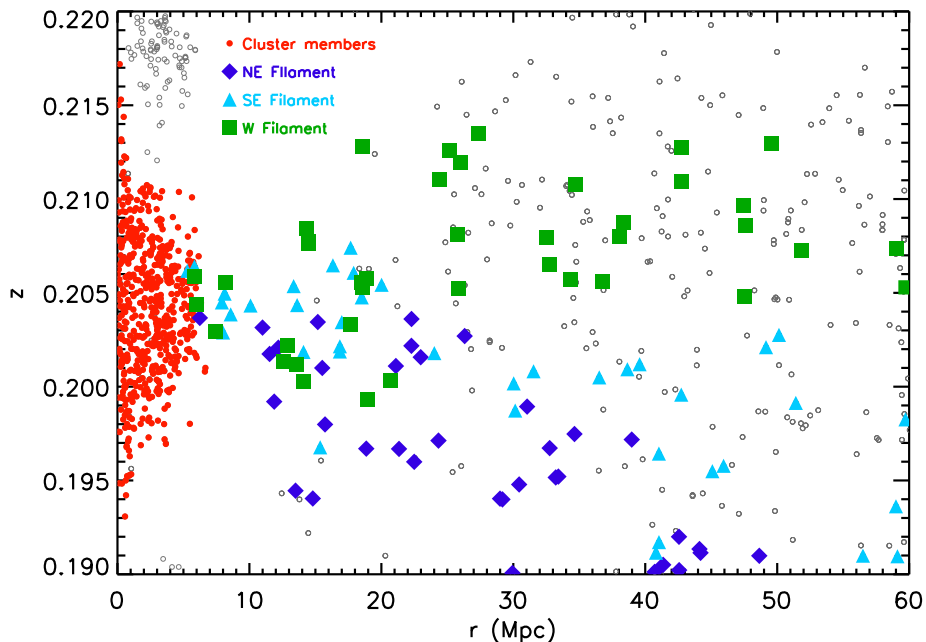


Figure 3.16: The galaxies shown on Fig. 3.15 in projected phase-space. The cluster-members are shown with red dots, and the galaxies associated with the three filaments with triangles, squares and diamonds of different colour. The rest of the galaxies are shown with empty small circles. The Figure is a reprint from Paper II.

dicating galaxies with a different accretion history. The exact boundaries of these regions are a result of N-body simulations and theoretical prescriptions detailed in (Jaffé et al. 2015). The virialised region is dominated by the oldest cluster-members, stripping indicated regions of high ICM density and/or high relative velocity where ram-pressure stripping (RPS) is highly efficient (Gunn & Gott 1972). Recent infalls encompass all the remaining cluster-member galaxies which are at high cluster-centric distances and/or with peculiar velocities too high to be in virial equilibrium with the cluster potential. As expected, the recent infalls region is where most of the blue galaxies reside, although there is a great number of passive galaxies there too (see Paper II for details as well as, for example, Haines et al. (2015) for exhaustive discussion on backsplash galaxies and the general incidence rate of passive galaxies in the field). The H I however offers a much clearer picture than even the NUV-R colours do. The stripping and virialised regions are almost completely devoid of H I detections. This is not surprising since the emission at optical and NUV wavelengths is indicative of the age of the stellar populations which changes on a longer timescale than the galaxy’s gas content, and is also the result of all the environmental processes that can suppress, but also inspire, star formation. The total gas content on the other hand reacts much faster to any disturbance, and as such shows the presence of fast-acting, possibly hydro-

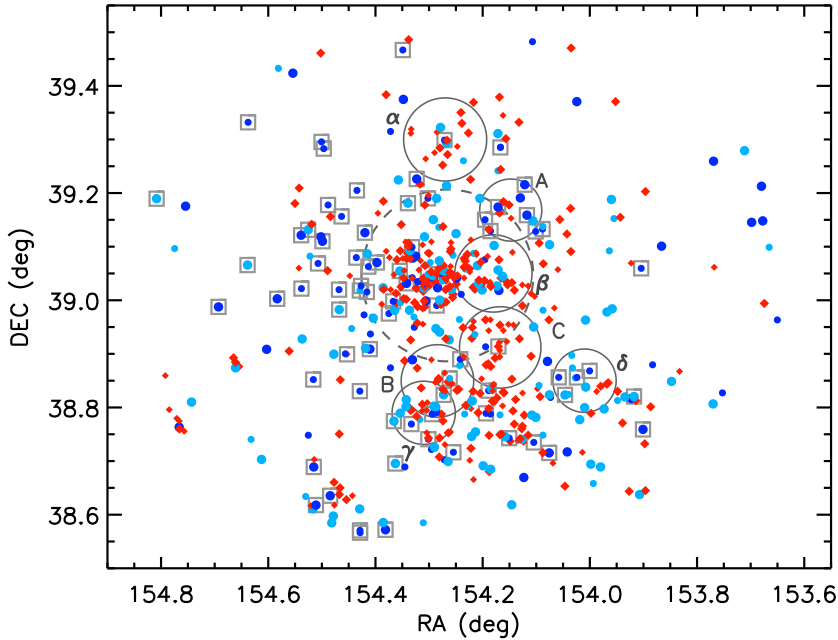


Figure 3.17: Distribution of the A963 members on the sky, colour coded according to their $\text{NUV} - R$ colours. Galaxies with integral $2.5 < \text{NUV} - R < 4.0$ and $\text{NUV} - R < 2.5$ colours are shown with light and dark blue circles, respectively. Those with $\text{NUV} - R > 4.0$ are shown with red diamonds. The size of the symbols indicate their total R-band luminosity. The H I detected galaxies are outlined with gray squares. The substructure information from Fig. 3.14 is carried over. The Figure is a reprint from Paper II.

dynamical, mechanisms for gas removal. These act, of course, on a population that already consists of at least 40% passive galaxies (Haines et al. 2015), being a combination of the general field and groups.

It is clear that even though A963 is unusually rich in blue galaxies (Butcher & Oemler 1984) it is not necessarily rich in H I detected galaxies. Looking at the projected phase-space shows that most likely the lack of H I is driven by ram-pressure stripping and, in general, is associated with the virialised region of the cluster, which is populated by the oldest cluster-members. Looking at the observed phase-space and sky distribution there is a hint at a possible depletion of H I in galaxies already in filaments prior to their accretion onto clusters. This is a result in line with the findings from the ALFALFA survey (Crone Odekon et al. 2018) but also from optical studies Kuutma et al. (2017).

3.2.2 H I analysis

Fig. 3.19 shows the ratio of actual H I content of galaxies to their expected H I content calculated from galaxies of similar morphological types and sizes. The definition of deficiency used here is described in detail in Paper II and differs

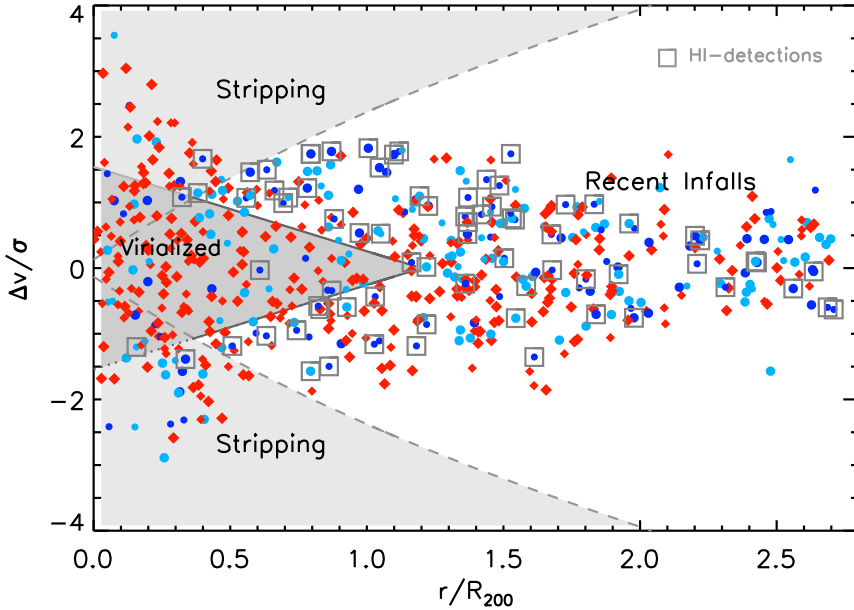


Figure 3.18: phase-space distribution of the galaxies shown on Fig. 3.17 with the same symbols and colours. Shaded areas indicate regions of interest discussed in the text. The Figure is a reprint from Paper II.

slightly from the original one of Haynes & Giovanelli (1984), largely due to the higher redshift of our targets which inhibits precise morphological classification. The data for the Coma cluster from Boselli & Gavazzi (2006) is shown for comparison with red symbols, and the mean deficiency is shown with the blue and red dashed lines for A963 and Coma, respectively. The shaded regions show 1σ around the two means. The open symbols show A963 members undetected at 21 cm. For these the lower limit in deficiency is plotted. Both A963 and Coma are similarly massive ($\sim 10^{15} M_{\odot}$), and both clusters show increase in deficiency with decreasing cluster-centric distance. However, the galaxies residing close to the centre of Coma are twice as deficient in HI as the central members of A963.

Figures 3.20 to 3.23 show the results of stacking of spectra extracted from the HI data cube at the positions of galaxies with known redshift. A similar approach for understanding the gas content of galaxies that are not directly detected has been used regularly with both single dish data (e.g. Fabello et al. 2011; Delhaize et al. 2013) and interferometric data (e.g. Verheijen et al. 2007; Geréb et al. 2015). We present the individual stacked spectra in the following Figures and summarise the results on Fig. 3.23. The spectra were extracted at the positions of known cluster-members and integrated spatially over the area of the synthesised beam. In order to show the significance of any detection of signal in the stacked spectra, comparison spectra were extracted at eight positions surrounding the location of the known galaxy and stacked in the same way. On each of the following Figures

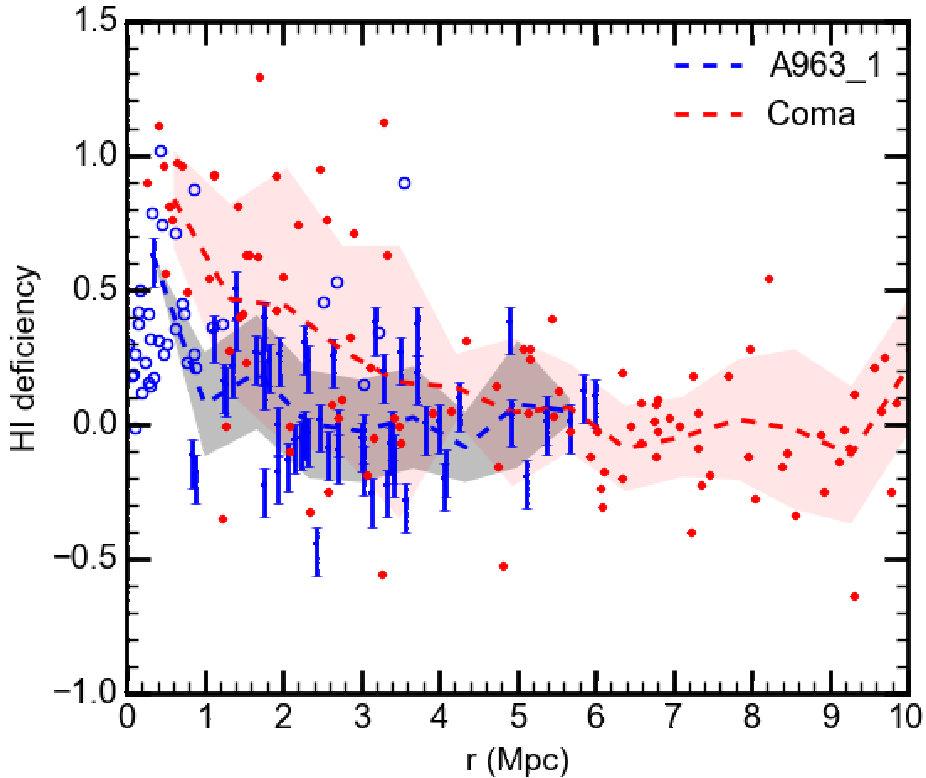


Figure 3.19: The HI deficiency as a function of cluster-centric distance for the blue galaxies in A963 (blue dots and circles for HI detected and undetected galaxies, respectively. The non detections are shown as lower limits), and in the Coma cluster (red dots, (Boselli & Gavazzi 2006)). The dashed blue and red lines with the associated shaded regions show the mean HI deficiency and 1σ uncertainty in A963 and Coma, respectively. The Figure is a reprint from Paper II.

these eight baseline stacks are shown with thin gray lines. The spectra were extracted from the data cubes without using any spectral smoothing. The velocity range of the stacked spectra is $\sim \pm 1800 \text{ km s}^{-1}$, allowing for assessment of the noise in the surrounding area and baseline.

Fig. 3.20 shows the stacked spectra of galaxies inside (left column) and outside R_{200} of the cluster, and with NUV-R colours > 4.0 (top row) and < 4.0 (bottom row). The total number of spectra in the stack (N_{gal}) and the number of direct HI detections ($N_{HI\,det}$) are indicated in each panel. The horizontal bar in the middle of each plot shows the velocity range integrated to calculate the average total HI mass in these galaxies. The red galaxies show much lower gas mass, as already indicated by the number of direct detections, with an average of $\langle M_{HI} \rangle < 0.13 \times 10^9 M_{\odot}$ and $\langle M_{HI} \rangle < 0.34 \times 10^9 M_{\odot}$ at $r < R_{200}$ and $r > R_{200}$, respectively. The emission from the blue galaxies is obvious and the average HI mass of the blue galaxies inside R_{200} is $\langle M_{HI} \rangle < 1.23 \times 10^9 M_{\odot}$, while those outside R_{200} show roughly double that amount.

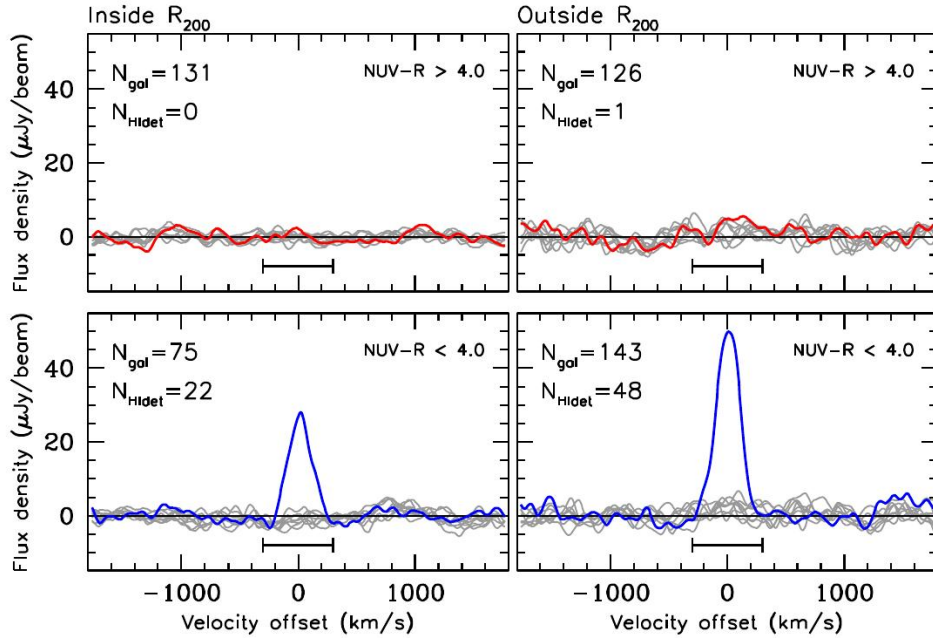


Figure 3.20: Stacking of HI spectra of red galaxies (top row) and blue galaxies (bottom row), inside R_{200} (left column), and outside R_{200} (right column). The stacks exclude group galaxies. The NUV-R colour range for the selection of galaxies and the total number of galaxies in each stack (N_{gal}), as well as the number of individually detected galaxies ($N_{H\text{Idet}}$), are indicated in each panel. The thin gray lines show the eight reference stacks of spectra extracted at reference positions around each source ~ 1 synthesised beam away. The Figure is a reprint from Paper II.

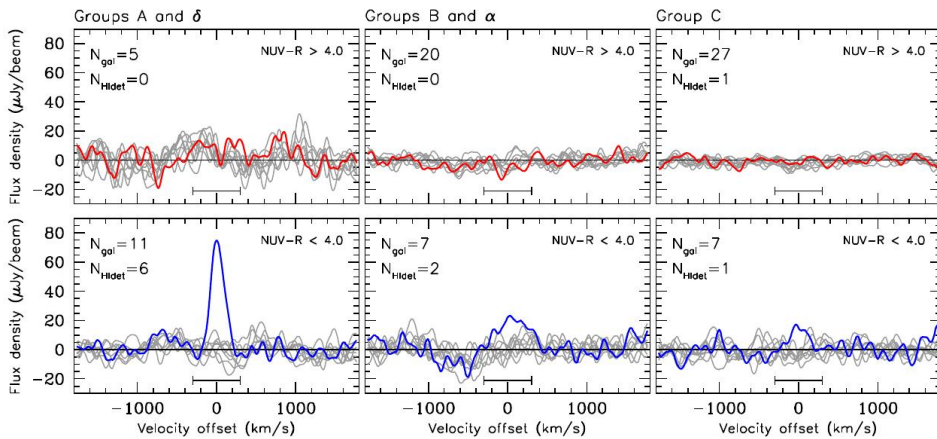


Figure 3.21: Stack of HI spectra of group galaxies split by colour (red - top row and blue - bottom row), and by group mass (low - left column, intermediate - middle column and high - right column). The Figure is a reprint from Paper II.

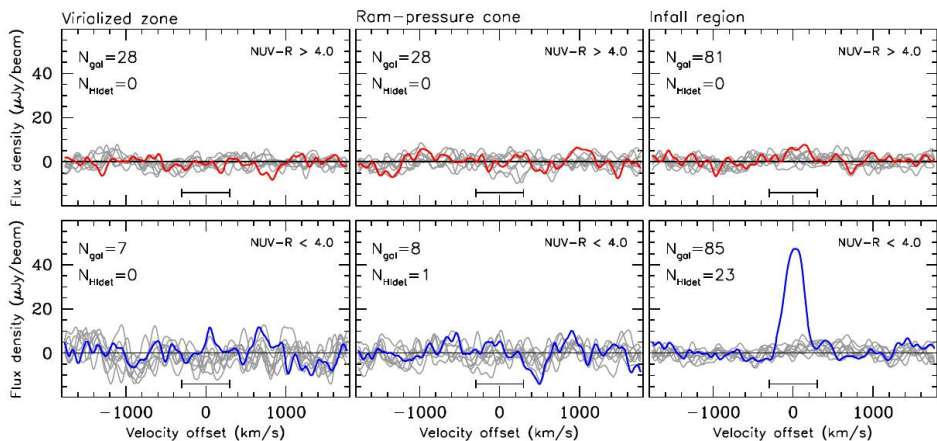


Figure 3.22: Stack of H I spectra of galaxies in different phase-space bins. Virialised zone - left column, ram-pressure stripping zone - middle column, and infall region - right column. Galaxies are split by colour as on Fig. 3.20. The stacks include only cluster-member galaxies and not group galaxies. The Figure is a reprint from Paper II.

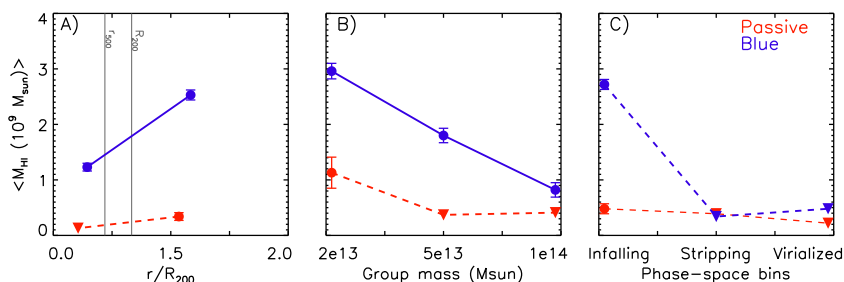


Figure 3.23: A summary of the results from the stacking of H I spectra presented on Figs.3.20–3.22. The detected H I mass is shown as a function of cluster-centric distance (left panel), group mass (middle panel), and phase-space bin (right panel). The results for red and blue galaxies are shown with red and blue lines and symbols, respectively. The Figure is a reprint from Paper II.

Fig. 3.21 shows the stacked spectra of galaxies - members of the five infalling groups with reliable mass estimate from those presented on Fig. 3.14. The groups are allocated to three bins of total mass, starting with the lowest group mass shown in the left column (groups A and δ with $\langle M \rangle = 1.75 \times 10^{13} M_{\odot}$), intermediate mass - $\langle M \rangle = 4.6 \times 10^{13} M_{\odot}$ (groups B and α) on the middle column, and high group mass - $\langle M \rangle = 1.0 \times 10^{14} M_{\odot}$ for group C shown on the right-hand column. As before, the group member galaxies are split into red and blue reflecting their NUV-R integrated colours with the red galaxies shown on the top row and the blue ones on the bottom row. None of the stacked spectra of red galaxies show any solid detection. The panels showing the stacked spectra of blue galaxies all show a clear detection of H I emission with total H I mass decreasing as a function of group mass, from $\langle M_{\text{H I}} \rangle < 2.96 \times 10^9 M_{\odot}$ in the lowest mass groups to $\langle M_{\text{H I}} \rangle < 0.82 \times 10^9 M_{\odot}$ in group C.

Fig. 3.22 shows stacked spectra of galaxies residing within the separate regions in projected phase-space outlined on Fig. 3.18. In the three columns from left to right we show galaxies from the virialised zone, ram-pressure dominated zone and from the infall region. The top row shows red galaxies while the bottom row shows blue galaxies. The number of galaxies in each stack varies drastically reflecting the underlying variation of galaxy colour with environment, as well as the relative size of the regions. Neither red nor blue galaxies residing in the virialised or RPS regions show any 21 cm emission. The passive galaxies in the infall region have on average $\langle M_{\text{H I}} \rangle = 0.48 \times 10^9 M_{\odot}$. The blue galaxies in the infall region show the strongest detection with an average H I mass of $\langle M_{\text{H I}} \rangle = 2.72 \times 10^9 M_{\odot}$.

Fig. 3.23 summarises the results of the spectral stacking presented in this section. On panel (A) the H I mass detected in blue and red galaxies found at cluster-centric distances below and above R_{200} is shown. On the middle panel (B) the dependence of H I mass on group mass is shown, and on panel (C) the average H I mass of galaxies along their path of accretion onto clusters is shown. In almost all cases the galaxy colour is a good indicator of the cold gas content of the galaxy. The Figure also demonstrates the effects of the environment in which galaxies reside on their cold gas content. Larger structures are occupied by more gas-poor galaxies. This trend can be traced starting on panel (B) and continues to the right-most point on panel (C). This is essentially a continuum of structures of ever increasing mass and moves deeper into these structures. The fact that the gas content of passive galaxies throughout this sequence shows very little change can be inferred from other studies (e.g. Zabludoff et al. 1996; Fujita 2004; Haines et al. 2015; Bianconi et al. 2018). Looking at Fig. 3.18, we see that inside R_{200} (the left-most point on panel (A) of Fig. 3.23) we have all three regions from the phase-space present. This explains the high gas content shown by the blue galaxies on panel (A). Dissecting the projected phase-space, as shown on Fig. 3.18, although limited in its scope, is important in understanding the evolution of galaxies as they are continuously pulled by gravity towards ever deeper gravitational potentials across the large scale structure of the universe.

Panel (C) on Fig. 3.23 also shows that ram-pressure stripping plays an im-

portant role and is probably the process that removes the H I from the infalling, gas-rich population. It is exactly during the transition between the infalling and RPS-dominated regions that blue galaxies lose all their gas and become indistinguishable from the passive populations, as far as H I is considered. However, the infalling region contains many passive galaxies which not only have red colours but contain little to no detectable amount of H I. While we know that groups with masses $M \leq 10^{14} M_{\odot}$ do pre-process their constituent galaxies and already show an increased fraction of passive galaxies (Papers II and III, but also Balogh et al. (1999); Fujita (2004); McGee et al. (2009); De Lucia et al. (2012); Bianconi et al. (2018)), not all the galaxies are accreted onto clusters as members of such groups and some of these are also already passive before they reach the outskirts of the cluster (groups deliver $\sim 40\%$ of the cluster galaxies by number (McGee et al. 2009)). For these galaxies the processes that govern their transformation from star forming to passive must be secular in nature: AGN and star formation feedback or bar formation (see e.g. Boselli & Gavazzi 2006, 2014, and references therein for an extensive review on the possible external and internal processes that can alter a galaxy’s fate). The physical mechanism carrying out the pre-processing of galaxies in groups is likely starvation, as only the most massive groups have dense enough ICM and/or high enough velocity dispersion for RPS to be effective. It is worth pointing out that, due to their lower mass, groups of galaxies probably have much lower accretion rates than clusters, so the majority of group galaxies have likely been in these groups for a long enough time even for low-efficiency processes to have an effect. Due to the relatively low velocity dispersion, particularly in low-mass groups, galaxy–galaxy interactions are expected to be very efficient.

Having defined the understanding of the nature of the Butcher–Oemler effect as one of the goals of this work, what can we conclude from this analysis? While the H I deficiency shown on Fig. 3.19 does indicate slightly elevated gas content in the central parts of the cluster, the stacking of H I spectra from blue galaxies shown on Fig. 3.20 indicates that the gas removal mechanisms working at $z = 0.2$ are as efficient as the ones working in the local universe. This is also supported by Fig. 3.22, which indicates the importance of ram-pressure as a gas removal mechanism in A963 (and presumably all clusters). The decreased deficiency, when compared to Coma on Fig. 3.19 can be attributed to the lack of morphological information, as described earlier, as well as the relatively high minimum detectable M_{HI} . The latter pushes many of the galaxies in the centre of the cluster below our detection limit. These galaxies are plotted as lower limit in deficiency and not taken into account in determining the average relation (blue, dashed line on Fig. 3.19).

An increased fraction of blue galaxies in the cluster interior could result either from reduced efficiency of the cluster-related quenching mechanisms or by increased accretion of galaxies, which, combined with the fact that quenching is not instant, will also elevate the blue fraction. Fig. 3.17 shows that the majority of the H I detections lie to the east of cluster centre where we do not find any substructures or LSS filaments. This leads us to conclude that A963 is indeed accreting a substantial population of galaxies not associated with any large groups and not in-

falling along filaments (which can also cause a reduction of the HI content Crone Odekon et al. 2018).

4

Conclusions

THIS thesis presents a multi-wavelength analysis of the galaxies in clusters at intermediate redshift. We concentrate on two clusters at $z = 0.2$, known to be in different evolutionary stages, the relatively relaxed A963 and the major merger A520, often nicknamed "the train wreck". We employ multi-object, optical spectrography, ultra-deep H I imaging, optical and infrared imaging as well as X-ray imaging. We compare our two protagonists with a sample of 30 clusters with $0.15 < z < 0.35$ with a total count of $\sim 28,000$ galaxies, sampling a range of environments. The H I data presented here is unique in terms of the integration time invested and the resulting noise levels achieved. It is also the only blind, interferometric survey probing redshifts where purely cosmological effects, like the Butcher–Oemler effect, start to play a role. Alongside analysis of the properties of cluster-member galaxies in projected phase-space we also analyse the distribution of galaxies on the sky and connect this with the large-scale structure surrounding the clusters.

Based on the analysis presented in this thesis we draw the following conclusions:

- Major cluster mergers do quench star formation.
- The star formation activity in galaxies is related to the formation history of the structure within which they reside.
- The galaxies in A963 responsible for the Butcher–Oemler effect show an H I content similar to that in local clusters.
- The Butcher–Oemler effect is most likely a result of increased accretion rate of galaxies not associated with smaller structures (no pre-processing) rather than evolution in the efficiency of environmental effects.
- The scatter of the Butcher–Oemler effect is due to, at least partially, different evolutionary histories of the clusters.
- To get closer to the full picture of the coevolution of galaxies and the structure they are embedded in we need to analyse the full observed phase-space.

- Even relatively low-sensitivity, wide-field, redshifted H I surveys can be very informative about the working of the environmental effects in distant clusters.
- Man-made radio frequency interference has effectively closed certain redshifts for H I studies.
- Outside the local universe we will only ever be able to measure three of the seven dimensions (full phase-space plus time) in which galaxies live. However, by connecting the evolution of galaxies with the known parts of the history of the clusters in which they are embedded we can, at least partially, add a fourth dimension – time, to the picture.

References

- Abell, G. O. 1958, *The Distribution of Rich Clusters of Galaxies.*, The Astrophysical Journal Supplement Series, 3, 211
- Allen, S. W. 1998, *Resolving the discrepancy between X-ray and gravitational lensing mass measurements for clusters of galaxies*, MNRAS, 296, 392
- Alpaslan, M. 2009, *A quick guide to FXCOR*, ArXiv e-prints, arXiv:0912.4755
- Andreon, S. 2006, *Some Thoughts and Some New Results about the Butcher-Oemler effect*, in *The Fabulous Destiny of Galaxies: Bridging Past and Present*, ed. V. Le Brun, A. Mazure, S. Arnouts, & D. Burgarella, 463
- Andreon, S. & Ettori, S. 1999, *Is the Butcher-Oemler Effect a Function of the Cluster Redshift?*, ApJ, 516, 647
- Andreon, S., Quintana, H., Tajer, M., Galaz, G., & Surdej, J. 2006, *The Butcher-Oemler effect at $z \sim 0.35$: a change in perspective*, MNRAS, 365, 915
- Baldry, I. K., Balogh, M. L., Bower, R. G., et al. 2006, *Galaxy bimodality versus stellar mass and environment*, MNRAS, 373, 469
- Balogh, M. L., Morris, S. L., Yee, H. K. C., Carlberg, R. G., & Ellingson, E. 1999, *Differential Galaxy Evolution in Cluster and Field Galaxies at $z \sim 0.3$* , ApJ, 527, 54
- Bamford, S. P., Nichol, R. C., Baldry, I. K., et al. 2009, *Galaxy Zoo: the dependence of morphology and colour on environment*, MNRAS, 393, 1324
- Becker, R. H., White, R. L., & Helfand, D. J. 1995, *The FIRST Survey: Faint Images of the Radio Sky at Twenty Centimeters*, ApJ, 450, 559
- Bekki, K. 1999, *Group-Cluster Merging and the Formation of Starburst Galaxies*, ApJ, 510, L15
- Bertin, E. & Arnouts, S. 1996, *SExtractor: Software for source extraction.*, A&AS, 117, 393
- Bianconi, M., Smith, G. P., Haines, C. P., et al. 2018, *LoCuSS: pre-processing in galaxy groups falling into massive galaxy clusters at $z = 0.2$* , MNRAS, 473, L79
- Boselli, A. & Gavazzi, G. 2006, *Environmental Effects on Late-Type Galaxies in Nearby Clusters*, PASP, 118, 517

- Boselli, A. & Gavazzi, G. 2014, *On the origin of the faint-end of the red sequence in high-density environments*, Astronomy and Astrophysics Review, 22, 74
- Bottinelli, L., Gouguenheim, L., Fouque, P., & Paturel, G. 1990, *An extragalactic data base. II - The HI data*, A&AS, 82, 391
- Briggs, D. 1995, *High Fidelity Deconvolution of Moderately Resolved Sources*, PhD thesis, New Mexico Institute of Mining and Technology, 1995
- Bruzual, G. & Charlot, S. 2003, *Stellar population synthesis at the resolution of 2003*, MNRAS, 344, 1000
- Bruzual A., G. 1983, *Spectral evolution of galaxies. I - Early-type systems*, ApJ, 273, 105
- Butcher, H. & Oemler, Jr., A. 1984, *The evolution of galaxies in clusters. V - A study of populations since Z approximately equal to 0.5*, ApJ, 285, 426
- Byrd, G. & Valtonen, M. 1990, *Tidal generation of active spirals and S0 galaxies by rich clusters*, ApJ, 350, 89
- Campbell, William, W. 1915, *The evolution of the stars and the formation of the earth*, The Popular Science Monthly, LXXXVII, 209
- Chung, S. M., Gonzalez, A. H., Clowe, D., et al. 2009, *Impacts of a Supersonic Shock Front on Star Formation in the Bullet Cluster*, ApJ, 691, 963
- Cid Fernandes, R., Stasińska, G., Mateus, A., & Vale Asari, N. 2011, *A comprehensive classification of galaxies in the Sloan Digital Sky Survey: how to tell true from fake AGN?*, MNRAS, 413, 1687
- Clowe, D., Markevitch, M., Bradač, M., et al. 2012, *On Dark Peaks and Missing Mass: A Weak-lensing Mass Reconstruction of the Merging Cluster System A520*, ApJ, 758, 128
- Cohen, S. A., Hickox, R. C., Wegner, G. A., Einasto, M., & Vennik, J. 2014, *Star Formation and Substructure in Galaxy Clusters*, ApJ, 783, 136
- Coziol, R., Andernach, H., Caretta, C. A., Alamo-Martínez, K. A., & Tago, E. 2009, *The Dynamical State of Brightest Cluster Galaxies and The Formation of Clusters*, AJ, 137, 4795
- Crone Odekon, M., Hallenbeck, G., Haynes, M. P., et al. 2018, *The Effect of Filaments and Tendrils on the HI Content of Galaxies*, ApJ, 852, 142
- Czoske, O., Moore, B., Kneib, J.-P., & Soucail, G. 2002, *A wide-field spectroscopic survey of the cluster of galaxies <ASTROBJ>Cl0024+1654</ASTROBJ>. II. A high-speed collision?*, A&A, 386, 31

- De Lucia, G., Weinmann, S., Poggianti, B. M., Aragón-Salamanca, A., & Zaritsky, D. 2012, *The environmental history of group and cluster galaxies in a Λ cold dark matter universe*, MNRAS, 423, 1277
- De Propris, R., Stanford, S. A., Eisenhardt, P. R., & Dickinson, M. 2003, *The K-selected Butcher-Oemler Effect*, ApJ, 598, 20
- Delhaize, J., Meyer, M. J., Staveley-Smith, L., & Boyle, B. J. 2013, *Detection of HI in distant galaxies using spectral stacking*, MNRAS, 433, 1398
- Deshev, B., Verheijen, M., van Gorkom, J., et al. 2009, *Westerbork ultra-deep HI imaging of galaxy clusters at $z=0.2$* , in Panoramic Radio Astronomy: Wide-field 1-2 GHz Research on Galaxy Evolution, 24
- Dressler, A. 1980, *Galaxy morphology in rich clusters - Implications for the formation and evolution of galaxies*, ApJ, 236, 351
- Dressler, A. & Shectman, S. A. 1988, *Evidence for substructure in rich clusters of galaxies from radial-velocity measurements*, AJ, 95, 985
- Dubuisson, M.-P. & Jain, A. 1994, in A modified Hausdorff distance for object matching, Vol. Vol. 1, 566
- Dwarakanath, K. S. & Owen, F. N. 1999, *On the Different Radio Source Populations in the Butcher-Oemler Clusters Abell 2125 and 2645*, AJ, 118, 625
- Fabello, S., Catinella, B., Giovanelli, R., et al. 2011, *ALFALFA HI data stacking - I. Does the bulge quench ongoing star formation in early-type galaxies?*, MNRAS, 411, 993
- Fabricant, D., Fata, R., Roll, J., et al. 2005, *Hectospec, the MMT's 300 Optical Fiber-Fed Spectrograph*, PASP, 117, 1411
- Fabricant, D. G., Kurtz, M. J., Geller, M. J., et al. 2008, *Spectrophotometry with Hectospec, the MMT's Fiber-Fed Spectrograph*, PASP, 120, 1222
- Falco, M., Hansen, S. H., Wojtak, R., et al. 2014, *A new method to measure the mass of galaxy clusters*, MNRAS, 442, 1887
- Feretti, L., Giovannini, G., Govoni, F., & Murgia, M. 2012, *Clusters of galaxies: observational properties of the diffuse radio emission*, A&A Rev., 20, 54
- Ferrari, C., Benoist, C., Maurogordato, S., Cappi, A., & Slezak, E. 2005, *Dynamical state and star formation properties of the merging galaxy cluster Abell 3921*, A&A, 430, 19
- Fujita, Y. 2004, *Pre-Processing of Galaxies before Entering a Cluster*, PASJ, 56, 29

- Fukugita, M., Nakamura, O., Okamura, S., et al. 2007, *A Catalog of Morphologically Classified Galaxies from the Sloan Digital Sky Survey: North Equatorial Region*, AJ, 134, 579
- Geréb, K., Morganti, R., Oosterloo, T. A., Hoppmann, L., & Staveley-Smith, L. 2015, *From star-forming galaxies to AGN: the global HI content from a stacking experiment*, A&A, 580, A43
- Giovanelli, R., Haynes, M. P., Kent, B. R., et al. 2005, *The Arecibo Legacy Fast ALFA Survey. I. Science Goals, Survey Design, and Strategy*, AJ, 130, 2598
- Girardi, M., Barrena, R., Boschin, W., & Ellingson, E. 2008, *Cluster Abell 520: a perspective based on member galaxies. A cluster forming at the crossing of three filaments?*, A&A, 491, 379
- Govoni, F., Markevitch, M., Vikhlinin, A., et al. 2004, *Chandra Temperature Maps for Galaxy Clusters with Radio Halos*, ApJ, 605, 695
- Gunn, J. E. & Gott, III, J. R. 1972, *On the Infall of Matter Into Clusters of Galaxies and Some Effects on Their Evolution*, ApJ, 176, 1
- Haines, C. P., Finoguenov, A., Smith, G. P., et al. 2018, *LoCuSS: The infall of X-ray groups onto massive clusters*, MNRAS
- Haines, C. P., Pereira, M. J., Smith, G. P., et al. 2015, *LoCuSS: The Slow Quenching of Star Formation in Cluster Galaxies and the Need for Pre-processing*, ApJ, 806, 101
- Haines, C. P., Pereira, M. J., Smith, G. P., et al. 2013, *LoCuSS: The Steady Decline and Slow Quenching of Star Formation in Cluster Galaxies over the Last Four Billion Years*, ApJ, 775, 126
- Haines, C. P., Smith, G. P., Egami, E., et al. 2009, *LOCUSS: The Mid-Infrared Butcher-Oemler Effect*, ApJ, 704, 126
- Haynes, M. P. & Giovanelli, R. 1984, *Neutral hydrogen in isolated galaxies. IV - Results for the Arecibo sample*, AJ, 89, 758
- Hoekstra, H., Herbonnet, R., Muzzin, A., et al. 2015, *The Canadian Cluster Comparison Project: detailed study of systematics and updated weak lensing masses*, MNRAS, 449, 685
- Hubble, E. & Humason, M. L. 1931, *The Velocity-Distance Relation among Extra-Galactic Nebulae*, ApJ, 74, 43
- Hubble, E. P. 1925a, *Cepheids in Spiral Nebulae*, Popular Astronomy, 33
- Hubble, E. P. 1925b, *NGC 6822, a remote stellar system.*, ApJ, 62

- Huttenlocher, D. P., Klanderman, G. A., & Rucklidge, W. A. 1993, *Comparing Images Using the Hausdorff Distance*, IEEE Trans. Pattern Anal. Mach. Intell., 15, 850
- Hwang, H. S. & Lee, M. G. 2009, *Galaxy activity in merging binary galaxy clusters*, MNRAS, 397, 2111
- Hwang, J.-S., Park, C., Banerjee, A., & Hwang, H. S. 2018, *Evolution of Late-type Galaxies in a Cluster Environment: Effects of High-speed Multiple Encounters with Early-type Galaxies*, ApJ, 856, 160
- Jaffé, Y. L., Smith, R., Candlish, G. N., et al. 2015, *BUDHIES II: a phase-space view of H I gas stripping and star formation quenching in cluster galaxies*, MNRAS, 448, 1715
- Jaffé, Y. L., Verheijen, M. A. W., Haines, C. P., et al. 2016, *BUDHIES - III: the fate of H I and the quenching of galaxies in evolving environments*, MNRAS, 461, 1202
- Jee, M. J., Hoekstra, H., Mahdavi, A., & Babul, A. 2014, *Hubble Space Telescope/Advanced Camera for Surveys Confirmation of the Dark Substructure in A520*, ApJ, 783, 78
- Jee, M. J., Mahdavi, A., Hoekstra, H., et al. 2012, *A Study of the Dark Core in A520 with the Hubble Space Telescope: The Mystery Deepens*, ApJ, 747, 96
- Joeveer, M. & Einasto, J. 1978, *Has the universe the cell structure*, in IAU Symposium, Vol. 79, Large Scale Structures in the Universe, ed. M. S. Longair & J. Einasto, 241
- Kauffmann, G., Heckman, T. M., White, S. D. M., et al. 2003, *Stellar masses and star formation histories for 10^5 galaxies from the Sloan Digital Sky Survey*, MNRAS, 341, 33
- Kenney, J. D. P., van Gorkom, J. H., & Vollmer, B. 2004, *VLA H I Observations of Gas Stripping in the Virgo Cluster Spiral NGC 4522*, AJ, 127, 3361
- Kennicutt, R. C. & Evans, N. J. 2012, *Star Formation in the Milky Way and Nearby Galaxies*, Annual Review of Astronomy and Astrophysics, 50, 531
- Kurtz, M. J. & Mink, D. J. 1998, *RVS AO 2.0: Digital Redshifts and Radial Velocities*, PASP, 110, 934
- Kurtz, M. J. & Mink, D. J. 2000, *Eigenvector Sky Subtraction*, ApJ, 533, L183
- Kuutma, T., Tamm, A., & Tempel, E. 2017, *From voids to filaments: environmental transformations of galaxies in the SDSS*, A&A, 600, L6
- Larson, R. B., Tinsley, B. M., & Caldwell, C. N. 1980, *The evolution of disk galaxies and the origin of S0 galaxies*, ApJ, 237, 692

- Lee, J., Kim, S., & Rey, S.-C. 2015, *A New Dynamical Mass Measurement for the VIRGO Cluster Using the Radial Velocity Profile of the Filament Galaxies*, ApJ, 807, 122
- Mahdavi, A., Hoekstra, H., Babul, A., Balam, D. D., & Capak, P. L. 2007, *A Dark Core in Abell 520*, ApJ, 668, 806
- Mahdavi, A., Hoekstra, H., Babul, A., et al. 2013, *Joint Analysis of Cluster Observations. II. Chandra/XMM-Newton X-Ray and Weak Lensing Scaling Relations for a Sample of 50 Rich Clusters of Galaxies*, ApJ, 767, 116
- Margoniner, V. E. & de Carvalho, R. R. 2000, *Photometric Properties of 48 Clusters of Galaxies. I. The Butcher-Oemler Effect*, AJ, 119, 1562
- Margoniner, V. E., de Carvalho, R. R., Gal, R. R., & Djorgovski, S. G. 2001, *The Butcher-Oemler Effect in 295 Clusters: Strong Redshift Evolution and Cluster Richness Dependence*, ApJ, 548, L143
- Markevitch, M., Govoni, F., Brunetti, G., & Jerius, D. 2005, *Bow Shock and Radio Halo in the Merging Cluster A520*, ApJ, 627, 733
- Martel, H., Robichaud, F., & Barai, P. 2014, *Major Cluster Mergers and the Location of the Brightest Cluster Galaxy*, ApJ, 786, 79
- McGee, S. L., Balogh, M. L., Bower, R. G., Font, A. S., & McCarthy, I. G. 2009, *The accretion of galaxies into groups and clusters*, MNRAS, 400, 937
- Merritt, D. 1983, *Relaxation and tidal stripping in rich clusters of galaxies. I. Evolution of the mass distribution*, ApJ, 264, 24
- Miller, N. A., Oegerle, W. R., & Hill, J. M. 2006, *Abell 2111: An Optical and Radio Study of the Richest Butcher-Oemler Cluster*, AJ, 131, 2426
- Miller, N. A. & Owen, F. N. 2003, *Abell 2255: Increased Star Formation and AGN Activity in a Cluster-Cluster Merger*, AJ, 125, 2427
- Mink, D. J., Wyatt, W. F., Caldwell, N., et al. 2007, *Automating Reduction of Multifiber Spectra from the MMT Hectospec and Hectochelle*, in *Astronomical Society of the Pacific Conference Series*, Vol. 376, *Astronomical Data Analysis Software and Systems XVI*, ed. R. A. Shaw, F. Hill, & D. J. Bell, 249
- Monet, D. G. 1998, *The 526,280,881 Objects In The USNO-A2.0 Catalog*, in *Bulletin of the American Astronomical Society*, Vol. 30, *American Astronomical Society Meeting Abstracts*, 1427
- Montes, M. & Trujillo, I. 2019, *Intracluster light: a luminous tracer for dark matter in clusters of galaxies*, MNRAS, 482, 2838
- Okabe, N. & Umetsu, K. 2008, *Subaru Weak Lensing Study of Seven Merging Clusters: Distributions of Mass and Baryons*, PASJ, 60, 345

- Omer, Jr., G. C. & Lawson, J. L. 1936, *Constancy of Wave-Length of a Spectral Line*, ApJ, 84, 477
- Owen, F. N., Ledlow, M. J., Keel, W. C., Wang, Q. D., & Morrison, G. E. 2005, *A Deep Radio Survey of Abell 2125. II. Accelerated Galaxy Evolution during a Cluster-Cluster Merger*, AJ, 129, 31
- Papaderos, P., Gomes, J. M., Vílchez, J. M., et al. 2013, *Nebular emission and the Lyman continuum photon escape fraction in CALIFA early-type galaxies*, A&A, 555, L1
- Peebles, P. J. E. 1970, *Structure of the Coma Cluster of Galaxies*, AJ, 75, 13
- Peng, C. Y., Ho, L. C., Impey, C. D., & Rix, H.-W. 2002, *Detailed Structural Decomposition of Galaxy Images*, AJ, 124, 266
- Peng, Y., Maiolino, R., & Cochrane, R. 2015, *Strangulation as the primary mechanism for shutting down star formation in galaxies*, Nature, 521, 192
- Peng, Y.-j., Lilly, S. J., Kovač, K., et al. 2010, *Mass and Environment as Drivers of Galaxy Evolution in SDSS and zCOSMOS and the Origin of the Schechter Function*, ApJ, 721, 193
- Peng, Y.-j., Lilly, S. J., Renzini, A., & Carollo, M. 2012, *Mass and Environment as Drivers of Galaxy Evolution. II. The Quenching of Satellite Galaxies as the Origin of Environmental Effects*, ApJ, 757, 4
- Poggianti, B. M. & Barbaro, G. 1997, *Indicators of star formation: 4000 Å break and Balmer lines.*, A&A, 325, 1025
- Poggianti, B. M., Bridges, T. J., Komiyama, Y., et al. 2004, *A Comparison of the Galaxy Populations in the Coma and Distant Clusters: The Evolution of k+a Galaxies and the Role of the Intracluster Medium*, ApJ, 601, 197
- Poggianti, B. M., Moretti, A., Gullieuszik, M., et al. 2017, *GASP I: Gas stripping phenomena in galaxies with MUSE*, ArXiv e-prints, arXiv:1704.05086
- Poggianti, B. M., von der Linden, A., De Lucia, G., et al. 2006, *The Evolution of the Star Formation Activity in Galaxies and Its Dependence on Environment*, ApJ, 642, 188
- Postman, M. & Geller, M. J. 1984, *The morphology-density relation - The group connection*, ApJ, 281, 95
- Rengelink, R. B., Tang, Y., de Bruyn, A. G., et al. 1997, *The Westerbork Northern Sky Survey (WENSS), I. A 570 square degree Mini-Survey around the North Ecliptic Pole*, A&AS, 124, 259
- Richstone, D. O. 1976, *Collisions of galaxies in dense clusters. II - Dynamical evolution of cluster galaxies*, ApJ, 204, 642

- Rines, K., Geller, M. J., Diaferio, A., & Kurtz, M. J. 2013, *Measuring the Ultimate Halo Mass of Galaxy Clusters: Redshifts and Mass Profiles from the Hectospec Cluster Survey (HeCS)*, ApJ, 767, 15
- Sarron, F., Adami, C., Durret, F., & Laigle, C. 2019, *Pre-processing of galaxies in cosmic filaments around AMASCFI clusters in the CFHTLS*, arXiv e-prints, arXiv:1903.02879
- Skibba, R. A., van den Bosch, F. C., Yang, X., et al. 2011, *Are brightest halo galaxies central galaxies?*, MNRAS, 410, 417
- Skrutskie, M. F., Cutri, R. M., Stiening, R., et al. 2006, *The Two Micron All Sky Survey (2MASS)*, AJ, 131, 1163
- Smail, I., Edge, A. C., Ellis, R. S., & Blandford, R. D. 1998, *A statistical analysis of the galaxy populations of distant luminous X-ray clusters*, MNRAS, 293, 124
- Smith, G. P., Khosroshahi, H. G., Dariush, A., et al. 2010, *LoCuSS: connecting the dominance and shape of brightest cluster galaxies with the assembly history of massive clusters*, MNRAS, 409, 169
- Smith, G. P., Kneib, J.-P., Smail, I., et al. 2005, *A Hubble Space Telescope lensing survey of X-ray luminous galaxy clusters - IV. Mass, structure and thermodynamics of cluster cores at $z = 0.2$* , MNRAS, 359, 417
- Sobral, D., Stroe, A., Dawson, W. A., et al. 2015, *MC²: boosted AGN and star formation activity in CIZA J2242.8+5301, a massive post-merger cluster at $z = 0.19$* , MNRAS, 450, 630
- Spitzer, Jr., L. & Baade, W. 1951, *Stellar Populations and Collisions of Galaxies.*, ApJ, 113, 413
- Springel, V., White, S. D. M., Jenkins, A., et al. 2005, *Simulations of the formation, evolution and clustering of galaxies and quasars*, Nature, 435, 629
- Stetson, P. B. 2000, *Homogeneous Photometry for Star Clusters and Resolved Galaxies. II. Photometric Standard Stars*, Publications of the Astronomical Society of the Pacific, 112, 925
- Stroe, A., Sobral, D., Afonso, A., et al. 2016, *A large H α survey of star formation in relaxed and merging galaxy cluster environments at $z \sim 0.15 - 0.3$* , ArXiv e-prints, arXiv:1611.03512
- Stroe, A., Sobral, D., Dawson, W., et al. 2015, *The rise and fall of star formation in $z = 0.2$ merging galaxy clusters*, MNRAS, 450, 646
- Stroe, A., Sobral, D., Röttgering, H. J. A., & van Weeren, R. J. 2013, *The role of cluster mergers and travelling shocks in shaping the H α luminosity function at $z = 0.2$: ‘sausage’ and ‘toothbrush’ clusters*, MNRAS

- Stroe, A., Sobral, D., Röttgering, H. J. A., & van Weeren, R. J. 2014, *The role of cluster mergers and travelling shocks in shaping the $H\alpha$ luminosity function at $z \sim 0.2$: ‘sausage’ and ‘toothbrush’ clusters*, MNRAS, 438, 1377
- Tempel, E., Tuvikene, T., Kipper, R., & Libeskind, N. I. 2017, *Merging groups and clusters of galaxies from the SDSS data. The catalogue of groups and potentially merging systems*, A&A, 602, A100
- Terlouw, J. P. & Vogelaar, M. G. R. 2015, Kapteyn Package, version 2.3, Kapteyn Astronomical Institute, Groningen, available from <http://www.astro.rug.nl/software/kapteyn/>
- Tinker, J., Kravtsov, A. V., Klypin, A., et al. 2008, *Toward a Halo Mass Function for Precision Cosmology: The Limits of Universality*, ApJ, 688, 709
- Tonry, J. & Davis, M. 1979, *A survey of galaxy redshifts. I - Data reduction techniques*, AJ, 84, 1511
- van Albada, G. B. 1960, *Formation and evolution of clusters of galaxies (Errata: 15 330)*, Bull. Astron. Inst. Netherlands, 15, 165
- van Albada, G. B. 1961, *Evolution of clusters of galaxies under gravitational forces*, AJ, 66, 590
- van der Hulst, J. M., Terlouw, J. P., Begeman, K. G., Zwitser, W., & Roelfsema, P. R. 1992, *The Groningen Image Processing System, GIPSY*, in Astronomical Society of the Pacific Conference Series, Vol. 25, Astronomical Data Analysis Software and Systems I, ed. D. M. Worrall, C. Biemesderfer, & J. Barnes, 131
- Verheijen, M., van Gorkom, J. H., Szomoru, A., et al. 2007, *WSRT Ultradeep Neutral Hydrogen Imaging of Galaxy Clusters at $z \sim 0.2$: A Pilot Survey of Abell 963 and Abell 2192*, ApJ, 668, L9
- Verheijen, M. A. W. & Sancisi, R. 2001, *The Ursa Major cluster of galaxies. IV. HI synthesis observations*, A&A, 370, 765
- Vijayaraghavan, R. & Ricker, P. M. 2013, *Pre-processing and post-processing in group-cluster mergers*, MNRAS, 435, 2713
- Wang, Q. H. S., Markevitch, M., & Giacintucci, S. 2016, *The Merging Galaxy Cluster A520- A Broken-up Cool Core, A Dark Subcluster, and an X-Ray Channel*, ApJ, 833, 99
- White, S. D. M. 1976, *The dynamics of rich clusters of galaxies*, MNRAS, 177, 717
- York, D. G., Adelman, J., Anderson, Jr., J. E., et al. 2000, *The Sloan Digital Sky Survey: Technical Summary*, AJ, 120, 1579
- Zabludoff, A. I., Zaritsky, D., Lin, H., et al. 1996, *The Environment of “E+A” Galaxies*, ApJ, 466, 104

Zwicky, F. 1933, *Die Rotverschiebung von extragalaktischen Nebeln*, Helvetica Physica Acta, 6, 110

Zwicky, F. 1937, *On the Masses of Nebulae and of Clusters of Nebulae*, ApJ, 86, 217

Zwicky, F. 1938, *On the Clustering of Nebulae*, PASP, 50, 218

Summary in Estonian

GALAKTIKAD ei täida maailmaruumi ühtlaselt. Gravitatsiooni mõjul on nende jaotus moodustanud universumi suuremastaabilise struktuuri. Tühikud on äärmiselt madala tihedusega piirkonnad, mis võivad olla suurusega kuni sadu megaparsekeid, sisaldades seejuures vaid üksikuid galaktikaid. Galaktikad paiknevad tühikuid ümbritsevates nii-nimetatud seintes. Seinte lõikumisjoontel moodustuvad galaktikate filamendid, mis omakorda viivad galaktikaparvedesse. Parved ise võivad olla koondunud veelgi suurematesse superparvedesse, mis on suurimad teadaolevad galaktikate struktuurid. Ehkki nimetatud keskkondades tõuseb galaktikate keskmine tihedus pidevalt, võivad kohalikud erinevused olla väga suured. Galaktikad asetsevad tavaliselt kas paarides või paari-kuni paarikümneliikmelistes gruppides, mida võib leida kõikjal suuremastaabilise struktuuri osades. Galaktikate omadused varieeruvad eri keskkondades. Madala tihedusega piirkonnad, tühikutest kuni parvede välisosadeni, sisaldavad umbes 60% tähetekkega galaktikatest punanihkel $z=0$. Parvede virialiseerunud siseosades asuvate galaktikatest on harva rohkem kui 10% selliseid, milles toimub tähtede tekkimine. Endiselt on ebaselge, millised füüsikalised protsessid põhjustavad tähetekke kahanemist galaktikate liikumisel suurema tihedusega piirkondadesse. Tõenäoliselt on tegemist rea erinevate protsessidega, mis mõjuvad galaktikatele erinevates struktuurides, väikestest gruppidest suure massiga parvedeni. Kõik mainitud struktuurid, sealjuures eriti parved on pidevas arengus uute galaktikate ning mõnikord ka tervete parvede lisandumise tõttu. Võrreldava massiga galaktikaparvede pörked on ühed kõige energeetilisemad sündmused universumis. Kirjeldatud pilt pole ajas muutumatu. Minnes suurematele punanihetele, s.o. varasematesse ajajärkudesse, näeme seaduspära, mis on tuntud kui Butcher-Oemleri efekt – järjest suurem osa tähetekkega galaktikatest asuvad parvedes. Samas eksisteerib igal punanihkel ka suur hajumine ja võib leida parvi väga erineva tähti tekitavate galaktikate osakaaluga.

Käesolevas doktoritöös uuriti kahte galaktikaparve, mis kuulusid Butcher-Oemleri efekti avastamisel kasutatud valimisse. Mõlemad parved, A520 ja A963, asuvad samal punanihkel $z=0.2$, kuid paiknevad tähetekkega galaktikate osakaalu jaotuse eri otstes. Antud töö eesmärgiks on leida seos parvede tekkimise ja arengu vahel, mis on viinud drastiliselt erinevate galaktikapopulatsioonide moodustumiseni. A963 on suhteliselt tasakaalulises olekus, mis on kooskõlas sellega liitunud gruppide oletatava hulgaga. A520 on seevastu kahe suure, võrdse massiga parve ja mitmete väiksemate struktuuride ühinemise tulemus. Tähetekkega galaktikate osakaal parves A520 on äärmiselt väike ning parves A963 väga suur.

Dokoritöö raames teostati parvede A520 ja A963 ligi 700 liikmesgalaktika spektroskoopilised vaatlused. Võrdluseks analüüsti veel 27 000 sarnastel

punanihetel erinevates keskkondades asuvat galaktikat, millest vähemalt pooled on samuti parvede liikmed. Põhjalikud 21cm joone interferomeetrilised vaatlused WSRT raadioteleskoobiga andsid võimaluse määrata külma gaasi hulka parves A963. Külma atomaarne gaas on tähetekke kütuseks ning on kergesti eemaldatav näiteks rõhu tõttu, mis avaldub galaktikatele liikumisel parvegaasi keskkonnas. Lisaks nimetatud läbiviidud vaatlusprogrammidele kasutati ka optilise, infrapuna- ja röntgenfotomeetriliste vaatluste tulemusi. Galaktikate kohta kogutud informatsiooni analüüsi koos nende ruumilise paiknemise ja liikumiskiirusega parvede suhtes. Samuti on võimaluse korral arvesse võetud andmeid nimetatud parvi ümbritsevate suuremastaabiliste struktuuride ning parve A520 korral ka pörke ajastuse kohta.

Kokkuvõtlikult võib öelda, et suurte parvede pörked lämmitavad täheteket galaktikates, kuigi on võimalik ka tähetekke lühike võimendusfaas ühinemise algperioodil. Galaktikate gaasisaldus kohaliku universumi parvedes on võrreldav nendega, mille puhul avaldub Butcher-Oemleri efekt. Siit võib teha järelduse, et Butcher-Oemleri efekti põhjustab pigem muutus galaktikate parvedesse lisandumise kiiruses ja režiimis kui protsessides, milles galaktikad ise parvekeskkonnas teisenevad. Vaatlustulemused on kooskõlas galaktikate lisandumisega ükshaaval, sest isegi väikestes galaktikagruppides domineerivad suured passiivsed galaktikad. Galaktikate evolutsioon näib olevat tihedalt seotud gruppide ja parvede arenguga, millesse nad kuuluvad.

Acknowledgements

THIS book summarises some of the work I've been involved in for the last twelve years. Naturally, over such a long period of time, many people have left a trace in one way or another. Some have actively participated in the research, others have been part of my personal life and as such have also affected the way the work progressed. A warm hug and thanks to all who won't find their names here. Some people need a special mentioning. First and foremost I want to thank my parents for sparking the interest in astronomy in me and for supporting me during my education. As is, I suppose, fitting for such a long period of time I've been blessed with four supervisors. In no particular order, Alexis, you are what I imagine a supervisor should be. Thanks for the help, and thank you 10× that for leaving me do it my way the rest of the time. Bodo, I really wish we had spoken more often. Thanks for the support and above all thanks for making it possible for me and my family to live and work for an entire year in one of the truly great, old, European cities. Peeter, thanks for helping me wrestling with the bureaucracy. Marc, you messed it up! I want to mention one particular collaborator here - Chris, thank you so much for the help! I find your articles and presentations so complete that they often make me feel there is little left to do in galaxy evolution studies.

Science apart, there is one person that stands above all else. Thank you, Tiina, for being the most supportive person I have ever known. I feel blessed to have you present in my life. The little ones did not exactly help with the work but I just have to mention how lovely they are.

I made many friends over those years. Impossible to thank everybody, but a few names not associated with astronomy should be mentioned. Roughly in order of appearance, Nikola, Manfred, Kosyo, Dani, Rob, Andreas. You guys have been for me like islands of sanity in a pretty damn mad sea. Thank you!

Antti, I guess, if it wasn't for you I wouldn't be doing astronomy anymore. So your contribution to this work is very important indeed. Thank you Juhan and Antti for translating the summaries of this thesis into Estonian. Thanks to Antti again and to Elmo for the financial support during my years at TO. Thanks, Maret for talking to me. That is more important than it may appear.

A large part of the work presented in this book was done at the Kapteyn Astronomical Institute in Groningen, The Netherlands. I am grateful to this institution for hosting me for the duration of the work. I learned a lot there. I thank Tartu Observatory and Tartu University for supporting me during my work on this thesis. Part of this work was done at Vienna University, Centro de Astrofísica en La Palma (CALP), and Ondřejov Observatory, for which I am grateful. I have many fond memories from all these places.

The research presented in this thesis has been financially supported by institutional research funding IUT26-2 and IUT40-2 of the Estonian Ministry of Education and Research. We acknowledge the support of the Centre of Excellence “Dark side of the Universe” (TK133) financed by the European Union through the European Regional Development Fund. This research has also been co-funded by "Dora" and "Dora Plus" scholarships of the Archimedes foundation, and "Jaan Einasto" scholarship.

PUBLICATIONS

Curriculum vitae

Personal data

Name	Boris Zhivkov Deshev
Date and place of birth	21 June 1976, Gorna Oryahovica, Bulgaria
Citizenship	Bulgarian
Current employment	Tartu Observatory (researcher)
Address	Tartu Observatory 61602 Tõravere Tartumaa, Estonia
Phone	(+372) 5620 5390
E-mail	boris.deshev@to.ee

Education

2014 – 2019	University of Tartu, PhD student
2005 – 2006	Sofia University, graduate student, MSc 2006 (astrophysics)
1999 – 2005	Sofia University, undergraduate student, BSc 2005 (physics)

Employment

2012 – present	Tartu Observatory, Estonia
2007 – 2011	Kapteyn Astronomical Institute, The Netherlands
2006 – 2007	Bulgarian Academy of Sciences, Bulgaria

Professional training

15 – 25 Jul 2008	Enrico Fermi School: "Astrophysics of Galaxy Clusters", Varenna, Italy
10 – 15 Sept 2007	European Radio Interferometry School, Bonn, Germany
2 – 7 Jul 2006	Summer School: "Evolution of galaxies and their large-scale environment", Bad Honef, Germany

Conference presentations

- 3 – 5 Oct 2018 Workshop “Tartu – Tuorla annual meeting 2018: The large scale properties of the universe as a whole”, Tuorla, Finland. *Oral presentation*: “On the role of pre-processing of galaxies in the universe as a whole”
- 21 – 22 Sept 2017 Conference “Cosmic Mergers, from massive black holes to massive clusters”, Birmingham, England
Oral presentation: “The passive core of the "Train Wreck" cluster, Abell 520”
- 19 – 23 Sept 2016 Conference “The Changing Face of Galaxies: uncovering transformational physics”, Hobart, Australia
Poster presentation: “Effects of dynamic environment on galaxy evolution”
- 22 – 25 Sept 2015 Workshop “Tartu – Tuorla annual meeting 2015: The Bright Side of Space”, Võru, Estonia. *Oral presentation*: “Are the galaxies in a merging cluster affected by it? The case of Abell 520”
- 2 – 6 March 2015 Conference “Multi-Object Spectroscopy in the next decade”, Santa Cruz de La Palma, Spain
Poster presentation: “Building up a cluster. The case of A520”
- 24 – 27 Sept 2013 Workshop “Tartu – Tuorla annual meeting 2013: ”
Oral presentation: “Are the galaxies in a merging cluster affected by it? The case of Abell 520”
- 6 – 10 August 2010 Conference “JENAM 2010: Environment and the Formation of Galaxies, Lisbon, Portugal
Poster presentation: “A volume limited H I imaging survey at $z=0.2$ ”
- 2 – 5 June 2009 Conference “Panoramic Radio Astronomy” Groningen, The Netherlands
Poster presentation: “Westerbork ultra-deep HI imaging of galaxy clusters at $z=0.2$ ”
- 23 – 26 June 2008 Conference “YERAC 2008”, Gothenburg, Sweden
Oral presentation: “Westerbork Ultra-Deep H I Imaging of Galaxy Clusters at $z=0.2$ ”
- 1 – 5 Oct 2007 Conference “Formation and Evolution of Galaxy Disks”, Rome, Italy *Poster presentation*: “Westerbork Ultra-Deep H I Imaging of Galaxy Clusters at $z=0.2$ ”
- 9 – 12 May 2006 Conference “5th Bulgarian-Serbian Conference on Astronomy and Space Science (BSCASS 2006)”, Sofia, Bulgaria
Oral presentation: “Radio Astronomy Projects in Sofia”

Honours and Awards

2015	E. Öpik scholarship (Tartu Observatory)
2016	Jaani Einasto scholarship (Tartu Observatory)

Publications

1. Einasto, Maret; Gramann, Mirt; Park, Changbom; Kim, Juhan; Deshev, Boris; Tempel, Elmo; Heinämäki, Pekka; Lietzen, Heidi; Lähteenmäki, Anne; Einasto, Jaan; Saar, Enn 2018, *Supercluster A2142 and collapse in action: infalling and merging groups and galaxy transformations*, Astronomy & Astrophysics, Volume 620, id.A149, 17 pp.
2. Einasto, Maret; Deshev, Boris; Lietzen, Heidi; Kipper, Rain; Tempel, Elmo; Park, Changbom; Gramann, Mirt; Heinämäki, Pekka; Saar, Enn; Einasto, Jaan 2018, *Infalling groups and galaxy transformations in the cluster A2142*, Astronomy & Astrophysics, Volume 610, id.A82, 15 pp.
3. Spethmann, Christian; Veermäe, Hardi; Sepp, Tiit; Heikinheimo, Matti; Deshev, Boris; Hektor, Andi; Raidal, Martti 2017, *Simulations of galaxy cluster collisions with a dark plasma component*, Astronomy & Astrophysics, Volume 608, id.A125, 11 pp.
4. Deshev, Boris; Finoguenov, Alexis; Verdugo, Miguel; Ziegler, Bodo; Park, Changbom; Hwang, Ho Seong; Haines, Christopher; Kamphuis, Peter; Tamm, Antti; Einasto, Maret; Hwang, Narae; Park, Byeong-Gon 2017, *Galaxy evolution in merging clusters: The passive core of the "Train Wreck" cluster of galaxies, A 520*, Astronomy & Astrophysics, Volume 607, id.A131, 18 pp.
5. Deshev, B.; Park, C.; Hwang, H. S.; Ziegler, B.; Verdugo, M.; Kamphuis, P.; Finoguenov, A.; Tenjes, P.; Tamm, A. 2016, *Building Up a Cluster: The Case of A520*, ASP Conference Series, Vol. 507, p.237
6. Jaffé, Yara L.; Verheijen, Marc A. W.; Haines, Chris P.; Yoon, Hyein; Cybulski, Ryan; Montero-Castaño, María; Smith, Rory; Chung, Aeree; Deshev, Boris Z.; Fernández, Ximena; van Gorkom, Jacqueline; Poggianti, Bianca M.; Yun, Min S.; Finoguenov, Alexis; Smith, Graham P.; Okabe, Nobuhiro 2016, *BUDHIES - III: the fate of H I and the quenching of galaxies in evolving environments*, Monthly Notices of the Royal Astronomical Society, Volume 461, Issue 2, p.1202-1221
7. Cybulski, Ryan; Yun, Min S.; Erickson, Neal; De la Luz, Victor; Narayanan, Gopal; Montaña, Alfredo; Sánchez, David; Zavala, Jorge A.; Zeballos, Milagros; Chung, Aeree; Fernández, Ximena; van Gorkom, Jacqueline; Haines, Chris P.; Jaffé, Yara L.; Montero-Castaño, María; Poggianti, Bianca M.; Verheijen, Marc A. W.; Yoon, Hyein; Deshev, Boris Z.; Harrington, Kevin; Hughes, David H.; Morrison, Glenn E.; Schloerb, F. Peter; Velazquez, Miguel 2016, *Early Science with the Large Millimeter Telescope: COOL BUDHIES I - a pilot study of molecular and atomic gas*

- at $z \simeq 0.2$, Monthly Notices of the Royal Astronomical Society, Volume 459, Issue 3, p.3287-3306
8. Jaffé, Y. L.; Verheijen, M. A.; Poggianti, B. M.; van Gorkom, J. H.; Deshev, B. Z. 2014, *BUDHIES: a Blind Ultra Deep HI Environmental Survey*, XIV Latin American Regional IAU Meeting, Vol. 44, pp. 80-80
 9. Jaffé, Y.; Poggianti, B.; Verheijen, M.; Van Gorkom, J.; Deshev, B. 2013, *The Effect of Environment on Star Formation and Gas Reservoirs With Budhies*, Tracing Cosmic Evolution with Clusters of Galaxies, conference, id. 74
 10. Jaffé, Yara L.; Poggianti, Bianca M.; Verheijen, Marc A. W.; Deshev, Boris Z.; van Gorkom, Jacqueline H. 2013, *BUDHIES I: characterizing the environments in and around two clusters at $z \simeq 0.2$* , Monthly Notices of the Royal Astronomical Society, Volume 431, Issue 3, p.2111-2125
 11. Jaffé, Yara L.; Poggianti, Bianca M.; Verheijen, Marc A. W.; Deshev, Boris Z.; van Gorkom, Jacqueline H. 2012, *Gas Reservoirs and Star Formation in a Forming Galaxy Cluster at $z \simeq 0.2$* , The Astrophysical Journal Letters, Volume 756, Issue 2, article id. L28, 5 pp.
 12. Verheijen, Marc; Deshev, Boris; van Gorkom, Jacqueline; Poggianti, Bianca; Chung, Aeree; Cybulski, Ryan; Dwarakanath, K. S.; Montero-Castano, Maria; Morrison, Glenn; Schiminovich, David; Szomoru, Arpad; Yun, Min 2010, *Westerbork Ultra-Deep Survey of HI at $z=0.2$* , eprint arXiv:1009.0279
 13. Verheijen, M. A. W.; Deshev, B.; van Gorkom, J.; Poggianti, B.; Chung, A.; Cybulski, R.; Dwarakanath, K. S.; Montero-Castaño, M.; Morrison, G.; Schiminovich, D.; Szomoru, A.; Yun, M. 2010, *Ultra-deep WSRT observations of HI at $z=0.2$* , Proceedings of the ISKAF2010 Science Meeting, id.54
 14. Deshev, B.; Verheijen, M.; van Gorkom, J.; Szomoru, A.; Dwarakanath, K.; Poggianti, B.; Schiminovich, D.; Chung, A.; Yun, M. S.; Morrison, G. 2009, *Westerbork ultra-deep HI imaging of galaxy clusters at $z=0.2$* , Proceedings of Panoramic Radio Astronomy: Wide-field 1-2 GHz research on galaxy evolution, id.24
 15. Stanchev, Orlin I.; Deshev, Boris Zh.; Nedialkov, Petko L.; Georgiev, Tsvetan B. 2006, *Scaling relations and fundamental plane for spiral galaxies in J-band*, Bulgarian Astronomical Journal, Vol. 8, p. 149
 16. Deshev, Boris Zh.; Stanchev, Orlin I.; Georgiev, Tsvetan B. 2006, *Revealing of convex disk profiles in LSB galaxies*, Bulgarian Astronomical Journal, Vol. 8, p. 143
 17. Georgiev, Ts.; Stanchev, O.; Deshev, B.; Yankulov, I.; Nedialkov, P. 2006, *Studies of convex radial profiles of galactic disks*, Bulgarian Astronomical Journal, Vol. 8, p. 39

Elulookirjeldus

Isikuandmed

Nimi	Boris Zhivkov Deshev
Sünniaeg ja -koht	21. juuni 1976, Gorna Oryahovica, Bulgaria
Kodakondsus	Bulgaarlane
Praegune töökoht	Tartu Observatoorium (teadur)
Aadress	Tartu Observatoorium 61602 Tõravere Tartumaa, Eesti
Telefon	(+372) 5620 5390
E-post	boris.deshev@to.ee

Haridus

2014 – 2019	Tartu Ülikool, doktorant
2005 – 2006	Sofia Ülikool, magistrant, MSc 2006 (astrofüüsika)
1999 – 2005	Sofia Ülikool, üliõpilane, BSc 2005 (füüsika)

Teenistuskäik

2012 – ...	Tartu Observatoorium, teadur
2007 – 2011	Kapteyn Astronomical Institute, Holland, teadur
2006 – 2007	Bulgarian Academy of Sciences, Bulgaaria, teadur

Täiendkoolitus

15.07 – 25.07 2008	Enrico Fermi Kool: "Astrophysics of Galaxy Clusters", Varenna, Itaalia
10.09 – 15.09 2007	European Radio Interferometry School, Bonn, Saksamaa
2.07 – 7.07 2006	Suvekool: "Evolution of galaxies and their large-scale environment", Bad Honef, Saksamaa

Konverentside ettekanded

3.10 – 5.10 2018	Konverents "Tartu – Tuorla annual meeting 2018: The large scale properties of the universe as a whole", Tuorla, Soome <i>Suuline ettekanne</i> : "On the role of pre-processing of galaxies in the universe as a whole"
21.09 – 22.09 2017	Konverents "Cosmic Mergers, from massive black holes to massive clusters", Birmingham, Inglismaa

19.09 – 23.09 2016	<p><i>Suuline ettekanne:</i> “The passive core of the "Train Wreck" cluster, Abell 520”</p> <p>Konverents “The Changing Face of Galaxies: uncovering transformational physics”, Hobart, Austraalia</p> <p><i>Plakat:</i> “Effects of dynamic environment on galaxy evolution”</p>
22.09 – 25.09 2015	<p>Konverents “Tartu – Tuorla annual meeting 2015: The Bright Side of Space”, Võru, Eesti</p> <p><i>Suuline ettekanne:</i> “Are the galaxies in a merging cluster affected by it? The case of Abell 520”</p>
2.03 – 6.03 2015	<p>Konverents “Multi-Object Spectroscopy in the next decade”, Santa Cruz de La Palma, Hispaania</p> <p><i>Plakat:</i> “Building up a cluster. The case of A520”</p>
24.09 – 27.09 2013	<p>Konverents “Tartu – Tuorla annual meeting 2013: ”</p> <p><i>Suuline ettekanne:</i> “Are the galaxies in a merging cluster affected by it? The case of Abell 520”</p>
6.08 – 10.08 2010	<p>Konverents “JENAM 2010: Environment and the Formation of Galaxies, Lisbon, Portugal</p> <p><i>Plakat:</i> “A volume limited HI imaging survey at z=0.2”</p>
2.07 – 5.07 2009	<p>Konverents “Panoramic Radio Astronomy” Groningen, Holland</p> <p><i>Plakat:</i> “Westerbork ultra-deep HI imaging of galaxy clusters at z=0.2”</p>
23.06 – 26.06 2008	<p>Konverents “YERAC 2008”, Göteborg, Rootsi</p> <p><i>Suuline ettekanne:</i> “Westerbork Ultra-Deep HI Imaging of Galaxy Clusters at z=0.2”</p>
1.10 – 5.10 2007	<p>Konverents “Formation and Evolution of Galaxy Disks”, Rooma, Itaalia</p> <p><i>Plakat:</i> “Westerbork Ultra-Deep HI Imaging of Galaxy Clusters at z=0.2”</p>
9.05 – 12.05 2006	<p>Konverents “5th Bulgarian-Serbian Conference on Astronomy and Space Science (BSCASS 2006)”, Sofia, Bulgaaria</p> <p><i>Suuline ettekanne:</i> “Radio Astronomy Projects in Sofia”</p>

Uurimistoetused ja stipendiumid

2015	E. Öpiku stipendium (Tartu Observatoorium)
2016	Jaan Einasto stipendium (Tartu Observatoorium)

DISSERTATIONES ASTRONOMIAE UNIVERSITATIS TARTUENSIS

1. **Tõnu Viik.** Numerical realizations of analytical methods in theory of radiative transfer. Tartu, 1991.
2. **Enn Saar.** Geometry of the large scale structure of the Universe. Tartu, 1991.
3. **Maret Einasto.** Morphological and luminosity segregation of galaxies. Tartu, 1991.
4. **Urmas Haud.** Dark Matter in galaxies. Tartu, 1991.
5. **Eugene A. Ustinov.** Inverse problems of radiative transfer in sounding of planetary atmospheres. Tartu, 1992.
6. **Peeter Tenjes.** Models of regular galaxies. Tartu, 1993.
7. **Ivar Suisalu.** Simulation of the evolution of large scale structure elements with adaptive multigrid method. Tartu, 1995.
8. **Teimuraz Shvelidze.** Automated quantitative spectral classification of stars by means of objective prism spectra: the method and applications. Tartu, 1999.
9. **Jelena Gerškevitš.** Formation and evolution of binary systems with compact objects. Tartu, 2002.
10. **Ivan Suhhonenko.** Large-scale motions in the universe. Tartu, 2003.
11. **Antti Tamm.** Structure of distant disk galaxies. Tartu, 2006.
12. **Vladislav-Veniamin Pustynski.** Modeling the reflection effect in pre-cataclysmic binary systems. Tartu, 2007.
13. **Anna Aret.** Evolutionary separation of mercury isotopes in atmospheres of chemically peculiar stars. Tartu, 2009.
14. **Mari Burmeister.** Characteristics of the hot components of symbiotic stars. Tartu, 2010.
15. **Elmo Tempel.** Tracing galaxy evolution by their present-day luminosity function. Tartu, 2011.
16. **Anti Hirv.** Estimation of time delays from light curves of gravitationally lensed quasars. Tartu, 2011.
17. **Rain Kipper.** Galaxy modelling: dynamical methods and applications. Tartu, 2016, 134 p.
18. **Lauri Juhan Liivamägi.** Properties and spatial distribution of galaxy superclusters. Tartu, 2017, 185 p.
19. **Jaani Laur.** Variability survey of massive stars in Milky Way star clusters. Tartu, 2017, 183 p.